

**UNSTEADY FLUID MECHANICS OF
STARTING-FLOW VORTEX GENERATORS WITH
TIME-DEPENDENT BOUNDARY CONDITIONS**

Thesis by

John Oluseun Dabiri

In Partial Fulfillment of the Requirements for the Degree of

Doctor of Philosophy

CALIFORNIA INSTITUTE OF TECHNOLOGY

Pasadena, California

2005

(Defended April 8, 2005)

© 2005

John Oluseun Dabiri

All Rights Reserved

Acknowledgements

Above all else, I thank my Lord and Savior Jesus Christ for His grace, strength, guidance, and wisdom as I have pursued a fuller understanding of his Creation. Let this thesis stand as a testament of His abundant love for each of us.

I have been crucified with Christ; it is no longer I who live, but Christ lives in me; and the life which I now live in the flesh I live by faith in the Son of God, who loved me and gave Himself for me. --Galatians 2:20

My family has provided continual support and encouragement since I first realized a passion for learning as a child. It is their care, along with the love and patience of Melissa Suzanne Blue, which has motivated me during difficult times.

My thesis advisor Mory Gharib has imbued in me the art of scientific investigation. It is under his tutelage that I have gained the perspective to approach classical problems in science and the confidence to solve new ones.

I have benefited from the advice, collaboration, and companionship of a host of memorable individuals associated with science education, including Messrs. David Barrows and Robert Shawver; Mrs. JoAnn Love; Drs. Edgar Choueiri, Michael Littman, Alexander Smits, Boguslaw Gajdeczko, Philip Felton, Frederick Dryer, Luigi Martinelli, Jay Hove, Michele Milano, Nikoo Saber, David Jeon, Paul Krueger, John Costello, Sean Colin, Tait Pottebaum, Matthew Ringuette, Gabriel Acevedo-Bolton, and Arash Kheradvar; Mmes. Kathleen Hamilton and Martha Salcedo; Mmes. Anna Hickerson and Rebecca Rakow-Penner; and Messrs. Arian Forouhar, Lance Cai, Ben Lin, Emilio Graff, and Derek Rinderknecht. I am especially grateful for the generous comments of Profs. John Brady, Joel Burdick, Michael Dickinson, Anthony Leonard, and Dale Pullin on this work.

Abstract

Nature has repeatedly converged on the use of starting flows for mass, momentum, and energy transport. The vortex loops that form during flow initiation have been reproduced in the laboratory and have been shown to make a proportionally larger contribution to fluid transport than an equivalent steady jet. However, physical processes limit growth of the vortex loops, suggesting that these flows may be amenable to optimization. Although it has been speculated that optimal vortex formation might occur naturally in biological systems, previous efforts to quantify the biological mechanisms of vortex formation have been inconclusive. In addition, the unsteady fluid dynamical effects associated with starting flow vortex generators are poorly understood.

This thesis describes a combination of new experimental techniques and *in vivo* animal measurements that determine the effects of fluid-structure interactions on vortex formation by starting flow propulsors. Results indicate that vortex formation across various biological systems is manipulated by these kinematics in order to maximize thrust and/or propulsive efficiency. An emphasis on observed vortex dynamics and transient boundary conditions facilitates quantitative comparisons across fluid transport schemes, irrespective of their individual biological functions and physical scales.

The primary contributions of this thesis are the achievement of quantitative measures of unsteady vortex dynamics via fluid entrainment and added-mass effects, and the development of a robust framework to facilitate the discovery of general design principles for effective fluid transport in engineering technologies and biological therapies. The utility of this new research paradigm is demonstrated through a variety of examples.

Table of Contents

Acknowledgements	iii
Abstract	iv
Table of Contents	v
List of Figures	viii
CHAPTER 1: Prologue	1
CHAPTER 2: Fluid entrainment by isolated vortex rings.....	4
2.0 Chapter Abstract.....	4
2.1 Introduction	5
2.2 Measurement Techniques	9
2.2.1 Apparatus.....	9
2.2.2 Counter-flow protocols	11
2.3 Results.....	13
2.3.1 Vortex ring trajectories	13
2.3.2 Fluid entrainment and vorticity distribution.....	15
2.4 Comparison with Maxworthy (1972)	24
2.5 A Quantitative Model for Diffusive Fluid Entrainment.....	31
2.6 Conclusions	35
2.7 Chapter References.....	38
CHAPTER 3: A contribution from wake vortex added-mass in estimates of animal swimming and flying dynamics.....	41
3.0 Chapter Abstract.....	41
3.1 Introduction	41
3.2 Methods	44
3.3 Results.....	45
3.4 Discussion.....	52
3.5 Chapter References.....	54
CHAPTER 4: Delay of vortex ring pinch-off by an imposed bulk counter-flow	57
4.0 Chapter Abstract.....	57
4.1 Introduction	57
4.2 Methods and Results	59
4.3 Conclusions	64
4.4 Chapter References.....	65
CHAPTER 5: A revised slug model boundary layer correction for starting jet vorticity flux.....	67
5.0 Chapter Abstract.....	67
5.1 Introduction	67
5.2 Revised Correction.....	69

5.3	Conclusions	71
5.4	Chapter References.....	71
CHAPTER 6: Starting flow through nozzles with temporally variable exit diameter		73
6.0	Chapter Abstract.....	73
6.1	Introduction	74
6.2	Apparatus and Experimental Methods.....	79
6.2.1	Apparatus design.....	79
6.2.2	Effects of noncircular nozzle shape.....	84
6.2.3	Quantitative flow visualization.....	85
6.2.4	Experimental parameter space.....	86
6.2.5	Boundary layer dynamics	88
6.3	Results.....	92
6.3.1	Vorticity flux	92
6.3.2	Dimensional analysis	95
6.3.3	Leading vortex ring pinch-off and vorticity distribution	98
6.3.4	Leading vortex ring energy.....	103
6.3.5	Leading vortex ring fluid transport.....	109
6.4	Summary and Conclusions.....	111
6.5	Chapter References.....	115
CHAPTER 7: Sensitivity analysis of kinematic approximations in dynamic medusan swimming models.....		120
7.0	Chapter Abstract.....	120
7.1	Introduction	120
7.2	Materials and Methods.....	122
7.2.1	Video recording and image processing	122
7.2.2	Dynamical model	124
7.2.3	Sensitivity analysis—bell volume and aperture area	125
7.2.4	Sensitivity analysis—fineness ratio.....	126
7.3	Results.....	128
7.3.1	Bell volume and aperture area approximations.....	128
7.3.2	Fineness ratio approximation.....	128
7.4	Discussion.....	131
7.5	Chapter References.....	135
CHAPTER 8: The role of optimal vortex formation in biological fluid transport		137
8.0	Chapter Abstract.....	137
8.1	Introduction	138
8.2	Methods	140
8.2.1	Kinematic analysis	140
8.2.2	Laboratory apparatus.....	141
8.3	Results.....	141
8.3.1	Laboratory results.....	141
8.3.2	Biological optimization strategy.....	143

8.3.3 Comparison with in situ squid measurements.....	144
8.3.4 Comparison with in vivo cardiac measurements	145
8.4 Discussion.....	147
8.5 Chapter References.....	148
CHAPTER 9: Flow patterns generated by oblate medusan jellyfish: field measurements and laboratory analyses.....	
9.0 Chapter Abstract.....	151
9.1 Introduction	152
9.2 Methods	155
9.2.1 Video measurements.....	155
9.2.2 Kinematic analyses	156
9.2.3 Strategies for dye marker interpretation.....	157
9.3 Results.....	158
9.3.1 Vortex formation process.....	158
9.3.2 Tentacle positioning.....	163
9.3.3 Vortex ring kinematic measurements.....	164
9.4 Discussion.....	166
9.4.1 Implications for medusan swimming behavior.....	166
9.4.2 Implications for medusan feeding behavior	170
9.4.3 Implications for prolate medusae.....	171
9.4.4 A note on fluid dynamic and geometric scaling.....	174
9.5 Chapter References.....	175

List of Figures

Figure 2.1	Schematic of apparatus for piston-cylinder experiments.....	10
Figure 2.2	Measured vortex ring trajectory for each counter-flow protocol	14
Figure 2.3	Instantaneous streamlines for protocol <i>LD2-CF0</i> at time $T = 5.34$ s	16
Figure 2.4	Measured entrainment fraction $\eta(t)$ for each counter-flow protocol	18
Figure 2.5	Instantaneous streamlines and vorticity patches for protocol <i>LD2-CF0</i>	21
Figure 2.6	Measured vortex ring core vorticity profiles.....	22
Figure 2.7	Measured vortex ring velocity for each counter-flow protocol.....	25
Figure 2.8	Measured vortex ring circulation for each counter-flow protocol.....	28
Figure 2.9	Instantaneous streamlines and vorticity patches for protocol <i>LD2-CF0</i>	30
Figure 2.10	Comparison of predicted vortex growth to experimental measurements.....	35
Figure 3.1	DPIV measurements of free-swimming jellyfish and a mechanical analogue ..	46
Figure 3.2	Demonstration of heuristic (i.e., Darwin, 1953) for measuring solid body added-mass.....	49
Figure 3.3	Measurements of Lagrangian drift induced by translating fluid vortices	50
Figure 3.4	Drift and fluid body volume measurements for translating vortices.....	51
Figure 4.1	Schematic of basic apparatus for counter-flow experiments.....	60
Figure 4.2	Circulation versus nondimensional time for nominal stroke ratio of 4.....	61
Figure 4.3	Nondimensional time versus physical time.....	63
Figure 5.1	Comparison of slug models of vorticity flux with DPIV measurements	70
Figure 6.1	Apparatus for temporal variation of nozzle exit diameter	83
Figure 6.2	Programs of nozzle exit diameter temporal variation.....	87
Figure 6.3	Rate of diameter change for each program of nozzle exit diameter temporal variation.....	87
Figure 6.4	Velocity profile of fluid efflux at $X = 0.3 D_p$ for static minimum and maximum diameter cases	91
Figure 6.5	Measured and predicted circulation generated for each program of nozzle exit diameter temporal variation.....	94
Figure 6.6	Normalized circulation versus formation time for each program of nozzle exit diameter temporal variation.....	97
Figure 6.7	Normalized circulation versus formation time for SMIN, SO, and FO cases ..	100
Figure 6.8	Vorticity profile along radial section of vortex ring core for SMIN, SO, and FO cases	100
Figure 6.9	Normalized circulation versus formation time for SMAX, SC, and FC cases ..	102
Figure 6.10	Vorticity profile along radial section of vortex ring core for SMAX, SC, and FC cases	102
Figure 6.11	Normalized vortex generator energy versus formation time	105
Figure 6.12	Vorticity contours of the flow downstream of the static maximum diameter nozzle	107
Figure 6.13	Vorticity contours of the flow downstream of the FC diameter nozzle	107
Figure 6.14	Delivered fluid fraction for leading vortex rings in nozzle cases with temporally variable exit diameter.....	110

Figure 7.1	Video recording and image processing	124
Figure 7.2	Measurements of <i>Chrysaora fuscescens</i> swimming.....	127
Figure 7.3	Dynamical swimming models for each test case	129
Figure 7.4	Measured and computed fineness ratio	130
Figure 7.5	Modeled swimming dynamics from fineness ratio measurement inputs	130
Figure 7.6	Ratio of diameter for exact fineness-hemiellipsoid model to bell aperture diameter.....	133
Figure 8.1	Schematic of jet flow apparatus with time-varying nozzle exit diameter	142
Figure 8.2	Vorticity profiles for different rates of jet exit diameter temporal increase.....	143
Figure 8.3	Tail-first swimming kinematics of <i>Lolliguncula brevis</i>	145
Figure 8.4	Trans-mitral flow during normal and pathological early diastolic filling	147
Figure 9.1	Schematic of a jetting medusa with vortex rings in the wake	153
Figure 9.2	Video sequence of vortex ring formation during two swimming cycles of <i>Aurelia aurita</i>	159
Figure 9.3	Kinematics of the starting, stopping, and co-joined lateral vortex structures ..	161
Figure 9.4	Video sequence and schematic of fluorescent dye relative to the tentacles of <i>Aurelia aurita</i> during a swimming cycle	164
Figure 9.5	Medusa bell shape profiles normalized by volume of ejected bell fluid Ω_b	175

CHAPTER 1: Prologue

This thesis is comprised of peer-reviewed articles from archival journals spanning the experimental and theoretical practices of engineering and biology. The organization is intentional and meant to underscore the interdisciplinary nature of the topics at hand while fomenting a clear emphasis on the discipline-specific contributions of this work.

The thesis author is also the lead author of each article and wrote all (Chapters 2 through 8) or the large majority (Chapter 9, all sections save parts of 9.2.1, 9.3.1, and 9.3.2) of the text in each case.

The articles are arranged with the goal of presenting results related to the physics of fluids first, followed by directed studies of biological applications. Chapters 2 and 3 investigate the primary unsteady effects in starting flows, namely fluid entrainment and added-mass dynamics. In both cases, new experimental techniques were developed to facilitate the first fully quantitative measurements of the associated fluid mechanics and, in the latter case, to demonstrate the existence of that unsteady component for the first time.

Chapters 4 and 5 examine the role of boundary layer kinematics in dictating the dynamics of vortex formation and saturation. In the first of these two chapters, a model is developed to predict the flux of vorticity from a starting jet. Its accuracy is shown to be an order of magnitude greater than existing standard models. Chapter 5 describes the development of an experimental method to manipulate shear layer kinematics in order to achieve the first artificial delay of vortex saturation, a result that has been considered in this research field a necessary condition for augmentation of starting jet fluid transport.

The results of Chapters 4 and 5 are incorporated into Chapter 6, which brings together boundary layer kinematics, vortex dynamics, and fluid-structure interactions in experiments aimed at addressing the fluid mechanics of biologically-relevant starting flows. The results indicate the importance of properly accounting for the time-dependent boundary conditions that are commonly observed in Nature and suggest that a rich diversity of fluid dynamical effects can be induced by relatively simple fluid-structure interactions. This chapter serves a dual role, both as a fundamental investigation of fluid mechanics and as a robust framework for studies of biological fluid transport systems.

Chapter 7 introduces the first dedicated studies of biological fluid transport in the thesis, using jellyfish as the model system. Its primary contribution is to highlight difficulties in modeling swimming dynamics based solely on propulsor morphology and kinematics. Chapter 8 takes this message further and illustrates the ability of the framework developed in Chapter 6 to predict normal and pathological function of biological fluid transport systems, with greater fidelity than is afforded by prevalent methods. Consistent with the overall theme of this thesis, the role of fluid-structure interactions and their proper modeling is emphasized. Importantly, it is shown that the principles of optimal vortex formation apply to a broad range of biological systems and can be analyzed quantitatively in each case without the need to reference details of their specific biological functionalities.

Finally, Chapter 9 describes the first quantitative, *in situ* field measurements of jellyfish swimming and related fluid dynamics. Results indicate that even for the simple morphology of these animals, the generated flow field can be quite complex. The careful tuning and coordination of multiple jellyfish functions that is achieved solely by exploiting fluid dynamics is fascinating, but also hints at the magnitude of our challenge in replicating

and improving upon these and other biological systems in engineering contexts. This thesis is effective if it inspires the reader to accept that challenge and the rewards that will follow.

CHAPTER 2: Fluid entrainment by isolated vortex rings

Submitted to Journal of Fluid Mechanics April 15, 2004

2.0 Chapter Abstract

Of particular importance to the development of models for isolated vortex ring dynamics in a real fluid is knowledge of ambient fluid entrainment by the ring. This time-dependent process dictates changes in the volume of fluid that must share impulse delivered by the vortex ring generator. Therefore fluid entrainment is also of immediate significance to the unsteady forces that arise due to the presence of vortex rings in starting flows. Applications, ranging from industrial and transportation to animal locomotion and cardiac flows, are currently being investigated to understand the dynamical role of the observed vortex ring structures. Despite this growing interest, fully empirical measurements of fluid entrainment by isolated vortex rings have remained elusive. The primary difficulties arise in defining the unsteady boundary of the ring, as well as an inability to maintain the vortex ring in the test section sufficiently long to facilitate measurements. We present a new technique for entrainment measurement that utilizes a coaxial counter-flow to retard translation of vortex rings generated from a piston-cylinder apparatus, so that their growth due to fluid entrainment can be observed. Instantaneous streamlines of the flow are used to determine the unsteady vortex ring boundary and compute ambient fluid entrainment. Measurements indicate that the entrainment process does not promote self-similar vortex ring growth, but instead consists of a rapid convection-based entrainment phase during ring formation, followed by a slower diffusive mechanism that entrains ambient fluid into the isolated vortex ring. Entrained fluid

typically constitutes 30% to 40% of the total volume of fluid carried with the vortex ring. Various counter-flow protocols were used to substantially manipulate the diffusive entrainment process, producing rings with entrained fluid fractions up to 65%. Measurements of vortex ring growth rate and vorticity distribution during diffusive entrainment are used to explain those observed effects, and a model is developed to relate the governing parameters of isolated vortex ring evolution. Measurement results are compared with previous studies of the process, and implications for the dynamics of starting flows are suggested.

2.1 Introduction

The earliest theoretical treatments of isolated vortex ring kinematics and dynamics predate quantitative experimental observations of the same phenomena by a half-century, due largely to the lack of available techniques to measure the salient fluid mechanics. Although ideal vortex ring models such as those of Saffman (1970), Fraenkel (1972), and Norbury (1973) have remained popular for describing empirical vortex ring dynamics (e.g., Gharib, Rambod and Shariff, 1998; Linden and Turner, 2001), the past few decades of research have witnessed several efforts to reconcile the predictions of analytical models with more recent observations made in the laboratory.

The most common method for generating vortex rings in the laboratory is the piston-cylinder arrangement. In this configuration, a cylindrical piston with outer diameter flush to the inner diameter of a hollow cylinder is translated axially from rest. A fluid efflux emerges after separating from the sharp-edged lip at the open end of the hollow cylinder.

The resulting cylindrical vortex sheet induces its own roll-up into a ring, which propagates axially away from the exit plane of the generator.

Vortex rings generated in the laboratory tend to depart from the thin-ring limit typically studied in theory. Nevertheless the literature contains notable examples of agreement between classical theoretical predictions and empirical observations (e.g., Widnall and Sullivan, 1973; Liess and Didden, 1976).

Maxworthy (1972) credits Reynolds (1876) with the first qualitatively correct observations of vortex ring propagation subsequent to the formation process. Specifically, Reynolds describes the growth of the ring in time due to entrainment of fluid surrounding the ring. Assuming the ring itself possesses a nominally constant impulse, the ring velocity decreases as a consequence of shared momentum with an increasing mass of fluid.

A physical mechanism for ambient fluid entrainment consisting of repeated cycles of viscous diffusion and circulatory transport is proposed by Maxworthy (1972). Vorticity from the core of the isolated vortex ring diffuses to its radial extent, where it interacts with oncoming irrotational fluid (in the reference frame of the vortex ring). A process of viscous dissipation reduces the total pressure of the fluid adjacent to the ring, to the point that it cannot pass over the ring and is instead entrained by the circulatory motion of the ring. A portion of the diffused vorticity will return to the ring in this entrainment process, while the remainder will form a small wake behind the ring. Formation of the wake is facilitated by free-stream fluid that still possesses sufficient total pressure after the dissipation process to convect the vorticity downstream.

Using dimensional analysis and physical arguments regarding the structure of the dissipation region, Maxworthy (1972) derives the rate of fluid entrainment as

$$\frac{d\Omega_B}{dt} = C\nu^{1/2}a^{3/2}U_v^{1/2}, \quad (2.1.1)$$

where Ω_B is the volume of the vortex bubble (i.e., the volume of fluid moving with the ring), ν is the kinematic viscosity, a is a characteristic dimension of the ring, and U_v is the characteristic velocity of the free-stream fluid relative to the ring. The quantity C is a dimensionless lumped parameter that incorporates the shape and size of the dissipation region, assuming self-similar vortex bubble growth. Equation (2.1.1) is used in concert with an assumption of constant vortex ring impulse to predict a $-2/3$ power-law decay of ring circulation in time, and to hypothesize the existence of a small wake of vorticity behind the ring.

Despite this progress, Maxworthy (1972) does not attempt to estimate the magnitude of the lumped parameter and therefore cannot attain a quantitative result for the contribution of entrainment to the dynamics of vortex rings. Maxworthy (1972) also lacks a method to empirically verify the predictions of ring circulation decay and wake formation. The validity of the assumption of constant ring impulse remains unknown, although Maxworthy (1972) limits it to high Reynolds numbers and small time scales.

Baird, Wairegi and Loo (1977) briefly address the role of fluid entrainment quantitatively, using the classical slug model (cf. Shariff and Leonard, 1992) to approximate the fraction of vortex ring fluid that originated in the free stream. They arrive at the result that $1/4$ of the fluid in the vortex ring is supplied by entrainment. The validity of the calculation is limited to small piston stroke length-to-diameter ratios—less than $2L/D$ by their own assertion—so that it can be assumed that all of the impulse delivered from the

vortex generator is transferred to the vortex ring. Confirmation of the prediction is not reported in those experiments or in subsequent work.

Müller and Didden (1980) visualize the growth of vortex rings using a dye marker in the flow and estimate the entrained fluid fraction of the vortex ring to be approximately 40%. As this was an estimated average value, no conclusions regarding the temporal dependence of the process can be made.

Transient measurements of fluid entrainment in vortex rings are especially cumbersome due to difficulty in observing and defining the boundary of the vortex ring as it propagates in time. Maxworthy (1972) notes that the physical extent of the ring may not be accurately determined from common dye visualizations, due to marked differences in the diffusion coefficients of the vorticity and the dye marker (e.g., Schmidt number $\sim 10^2$ for Rhodamine WT). As such, he notes the propensity to misinterpret qualitative visualizations of the entrainment process (e.g., Prandtl and Tietjens, 1934). Fully quantitative measurements of unsteady ambient fluid entrainment by isolated vortex rings have not yet been accomplished.

The task of measuring fluid entrainment is simplified if the ring can be maintained within the measurement window for longer periods of time. In the absence of external intervention, the ring will propagate away from the vortex generator under its self-induced velocity. The time allotted for an entrainment measurement will then be dictated by the length of the viewing window and the ring speed.

A set of experiments was conducted to demonstrate use of an axisymmetric counter-flow to maintain the vortex ring within the measurement window for longer periods of time, with the goal of observing ring growth due to fluid entrainment.

Instantaneous streamlines of the flow in the reference frame of the vortex ring were measured using quantitative flow visualization techniques. These data enabled definition of the unsteady boundary of the vortex ring for transient entrainment calculations.

Although convective transport dominates the fluid entrainment process during vortex ring formation, the focus of this paper is on the diffusive mechanism of ambient fluid entrainment that is observed in isolated vortex rings. Various counter-flow protocols were implemented to manipulate this entrainment process and to elucidate the governing physical principles. Based on these results, a model is developed to quantitatively relate the salient parameters of isolated vortex ring evolution. The experimental data obtained here are compared and contrasted with the work of Maxworthy (1972) and the estimates of Baird et al. (1977) and Müller and Didden (1980). Finally, implications for the dynamics of starting flows are suggested.

2.2 Measurement Techniques

2.2.1 Apparatus

Experiments were conducted in a 60 cm H \times 40 cm W \times 110 cm L water tank using an impulsively started piston-cylinder arrangement similar to that described by Gharib et al. (1998). A basic schematic of the apparatus is shown in figure 2.1 (adapted from Krueger, Dabiri and Gharib 2003). The piston is driven by an external water supply that is maintained at constant total head ($\Delta p = 8.2$ kPa) and delivered by a computer-controlled solenoid valve (ASCO Valve, Inc.), to provide a repeatable piston velocity profile. Fluid ejected from the open end of the sharp-edged hollow cylinder (inner diameter = 2.54 cm) rolls into a vortex ring and propagates through the surrounding fluid.

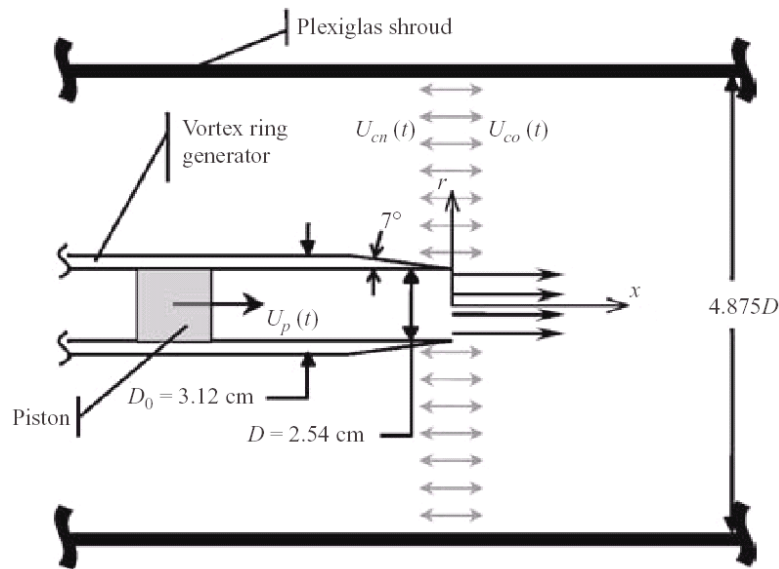


Figure 2.1 Schematic of apparatus for piston-cylinder experiments (adapted from Krueger et al. 2003).

A modification to the traditional piston-cylinder arrangement was made by enclosing the primary cylinder in a 12 cm diameter coaxial shroud. An external pump (Leeson Electronic Corp.) connected to the shroud drives flow around the primary cylinder in either a co-flowing (*co*) or counter-flowing (*cn*) configuration. Flow conditioning screens ensure nominally uniform flow around the primary cylinder. The shroud flow is also regulated by a computer-controlled solenoid valve. Tests verified that the presence of the shroud did not affect the observable vortex dynamics.

Ultrasonic flow probes (Transonic Systems, Inc.) measure the flow rates in the cylinder and shroud. All flow data are recorded to a computer hard disk via a LabVIEW (National Instruments) program. The starting jet flows are visualized quantitatively using digital particle image velocimetry (DPIV, cf. Willert and Gharib, 1991). The water tank is seeded with 13-micron (nominally) glass spheres that reflect light at the incident wavelength. Illumination is provided by a double-pulsed Nd:YAG laser (New Wave

Research) that delivers 30 mJ of energy per pulse at 532 nm. The laser beam is collimated by a cylindrical lens before entering the test section, which measures approximately 12 cm radially and 20 cm axially downstream of the vortex generator exit plane.

Mie scattering from the seeded water is captured by a 1024×1024 pixel black-and-white CCD digital camera (Uniq Vision, Inc.) at 30 Hz. The pixel resolution corresponds to a physical test section resolution of approximately 0.19×0.19 mm. This is sufficient to resolve the vortex ring core vorticity distribution. Image data are transferred in real time by a progressive scan protocol to a frame grabber (Coreco Imaging) linked to a PC.

Images are paired according to the method described by Willert and Gharib (1991). In the present case, each pair of images represents a separation of 18 ms between laser pulses. This timing results in an average particle shift of 4-7 pixels between images for the nominal piston speed of 5.5 cm s^{-1} . Interrogation is accomplished using a window size of 32×32 pixels with a 50% overlap. Calculations of velocity and vorticity fields are completed using an in-house code on an Intel 2-GHz processor. Velocity and vorticity measurements possess an uncertainty of 1% and 3%, respectively. A MATLAB (The Mathworks, Inc.) algorithm was created to rapidly visualize the instantaneous streamlines of the flow, based on the measured velocity field.

The flow Reynolds number is 1400 based on the piston speed and cylinder exit diameter, and varies between 2000 and 4000 based on the ring circulation (i.e., loop integral of measured velocity along a path enclosing the vortex).

2.2.2 Counter-flow protocols

A variety of counter-flow protocols were implemented to manipulate the dynamics of vortex rings generated by the piston-cylinder apparatus. The primary goal of these

protocols was to maintain the vortex rings in the test section for sufficient time to permit transient fluid entrainment measurements after initial ring formation. In addition, several of the protocols were used to affect the vorticity distribution of the rings via the dynamics of the shear layer efflux from the vortex generator. The strength and convective velocity of the shear layer were affected by the counter-flow, increasing the former and decreasing the latter. These effects resulted in a modified vorticity distribution in the vortex ring. The dynamics of the entrainment process were significantly altered by changing the vorticity distribution in some cases, as will be shown in section 2.3.

In the absence of counter-flow, vortex ring *pinch-off* (i.e., dynamic separation from the vortex generator flow source, cf. Gharib et al., 1998) was observed to occur at a formation number $F = 3.6$, where

$$F = \frac{\overline{U_p} t|_{\text{pinch-off}}}{D} = \frac{L|_{\text{pinch-off}}}{D}. \quad (2.2.1)$$

In (2.2.1), $\overline{U_p}$ is the running average of the piston velocity, L is the total piston stroke length (i.e., at the end of fluid ejection), D is the cylinder exit diameter, and t is time measured relative to the start of piston motion. Hence, counter-flow protocols initiated prior to $L/D = 3.6$ affected the vortex ring vorticity distribution, whereas those initiated subsequent to pinch-off could not.

The magnitude of the counter-flow was assigned one of two values. In the first case it was matched to the measured vortex ring propagation speed U_v in the absence of counter-flow. This enabled vortex rings to be maintained at a single axial location for longer periods of time. Alternatively, the counter-flow was set to one-half of the nominal piston speed. This is the theoretical vortex ring propagation speed predicted by the slug model

(Baird et al., 1977). Table 2.1 lists the set of counter-flow protocols utilized in these experiments, along with an abbreviated notation to be used in the following sections. The basic format of the notation is [*vortex generator L/D*]-[*counter-flow speed*]-[*initiation delay*].

Notation	Vortex generator L/D	Counter-flow speed	Initiation Delay
<i>LD2-CF0</i>	2	0	N/A
<i>LD2-CF05-12</i>	2	$0.5U_p$	12 L/D
<i>LD2-CFE</i>	2	$U_v _{CF0}$	0
<i>LD4-CF0</i>	4	0	N/A
<i>LD4-CF05-2</i>	4	$0.5U_p$	2 L/D
<i>LD4-CF05-6</i>	4	$0.5U_p$	6 L/D
<i>LD4-CFE</i>	4	$U_v _{CF0}$	0

Table 2.1 Counter-flow protocols.

2.3 Results

2.3.1 Vortex ring trajectories

Figure 2.2 plots the trajectories of vortex rings generated using the protocols in table 2.1, as measured from the location of peak vorticity in the ring. In the absence of counter-flow, cases *LD2-CF0* and *LD4-CF0* exhibit the expected ring propagation axially away from the vortex generator under self-induced velocity. The additional shear layer strength and concomitant circulation increase generated in cases *LD2-CFE* and *LD4-CFE* (i.e., due to counter-flow initiation prior to vortex ring pinch-off) enables these vortex rings to emerge from the vortex generator, despite the presence of counter-flow equal to $U_v|_{CF0}$. The increased circulation in the *LD4-CFE* case is greater than that in the *LD4-CF05-2* protocol, leading to the observed larger axial translation away from the vortex generator.

Vortex rings generated under the protocols with larger counter-flow initiation delays (i.e., *LD2-CF05-12* and *LD4-CF05-6*) exhibited abrupt changes in vortex ring trajectory due to the sudden application of a relatively large counter-flow.

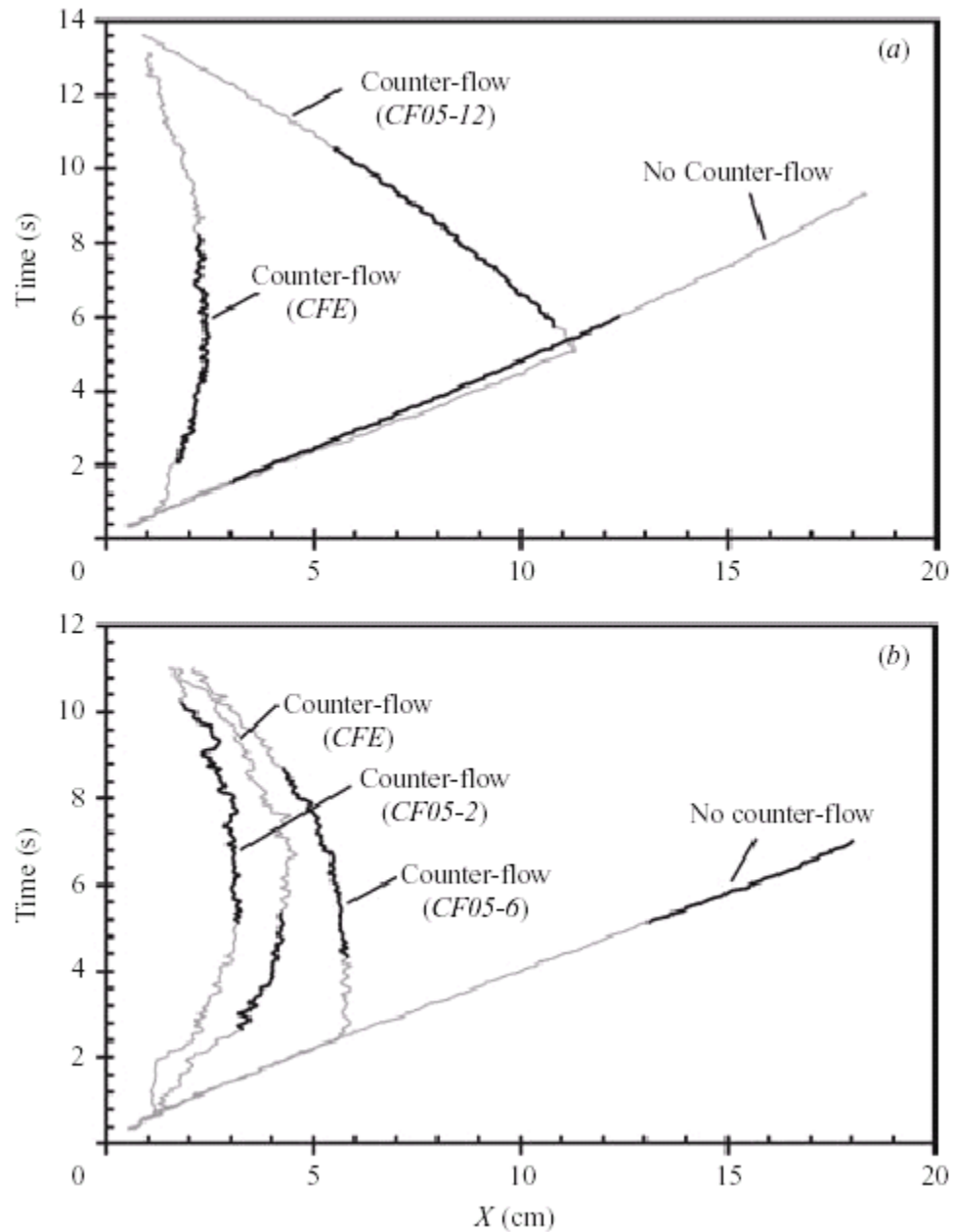


Figure 2.2 Measured vortex ring trajectory for each counter-flow protocol.
(a) $L/D = 2$; (b) $L/D = 4$.

In each of the counter-flow protocols, a trend can be observed at later times in which the counter-flow dominates the self-induced velocity of the rings, convecting the vortex ring structure back toward the vortex generator. This effect can be attributed to the increasing mass of fluid in the vortex bubble as the entrainment process proceeds, slowing and ultimately reversing the forward progress of the bubble.

The darkened portion of each vortex ring trajectory in figure 2.2 will be the focus of the following investigations. In these regions the vortex ring can be considered isolated, and the transients associated with the formation process (e.g., fluid convection from the vortex generator) have ceased.

2.3.2 *Fluid entrainment and vorticity distribution*

Measurements of transient fluid entrainment and vorticity distribution in isolated vortex rings were made using DPIV. The primary difficulty associated with such measurements—definition of the vortex boundaries—was overcome by making use of instantaneous streamlines of the flow determined from DPIV velocity field results and a post-processing algorithm created for this purpose.

An example of the instantaneous streamlines measured from a steadily translating vortex ring (protocol *LD2-CF0*, time $T = 5.34$ s) is shown in figure 2.3(a), in a laboratory reference frame. The physical extent of the vortex is not evident until the measurement is taken in a frame moving with the ring. This was accomplished by superimposing a free-stream axial flow with magnitude equal to the measured ring axial velocity. Figure 2.3(b) shows the same vortex ring in its moving frame. Its physical extent is well-defined.

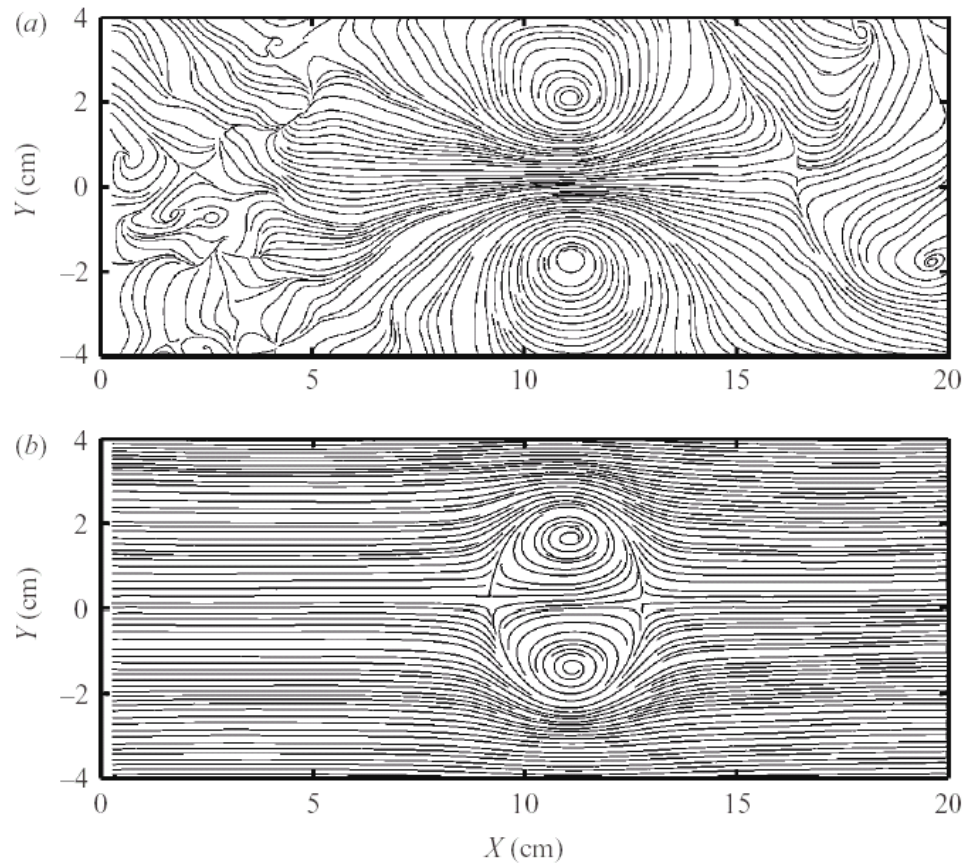


Figure 2.3 Instantaneous streamlines for protocol *LD2-CF0* at time $T = 5.34$ s. (a) Laboratory frame; (b) vortex ring frame. Flow is from left to right.

The ring velocity was measured from the axial location of peak vorticity in the cores. A more correct measurement should use an *ad hoc* vorticity centroid location, such as that suggested by Saffman (1970). However, the difference between Saffman's vorticity centroid location and the vorticity peak appears to remain within experimental error.

The volume of the vortex bubble $\Omega_B(t)$ was computed using an ellipsoidal fit based on the measured locations of the front and rear stagnation points as well as the radial extent of the ring. In the event that the rear stagnation point was obscured (e.g., when in close proximity to the vortex generator), this point was defined as the mirror image of the

front stagnation point relative to a plane containing the vortex core centers and oriented normal to the axial direction.

Given the measured volume of the vortex bubble $\Omega_B(t)$ and the fluid volume $\Omega_J(t)$ supplied by the vortex generator,

$$\Omega_J(t) = \frac{\pi D^2}{4} \int_0^t U_p(\tau) d\tau, \quad (2.3.1)$$

the magnitude of entrainment was quantified by the entrained fluid fraction $\eta(t)$, where

$$\eta(t) = \frac{\Omega_B(t) - \Omega_J(t)}{\Omega_B(t)} = 1 - \frac{\Omega_J(t)}{\Omega_B(t)}. \quad (2.3.2)$$

Measurements possess an uncertainty of 8% to 10%. The primary source of error lies in the measured instantaneous vortex ring velocity that is used to visualize the streamlines in the moving ring frame. This velocity measurement has a first-order effect on the observed location of the ring stagnation points when the free-stream velocity is superimposed.

Figure 2.4 plots the entrained fluid fraction $\eta(t)$ measured during the darkened portion of each vortex ring trajectory in figure 2.2. The trends are generally monotonic in favor of increasing bubble volume. Oscillations in the measured data for protocol *LD4-CF05-2* were suspected to be due to rotation of its non-circular vortex cores, which tended to distort the measurement of the radial vortex ring extent. This was confirmed by examination of the vorticity contours, which indicated that the frequency of measurement oscillation exactly matched the frequency of the non-circular core rotation.

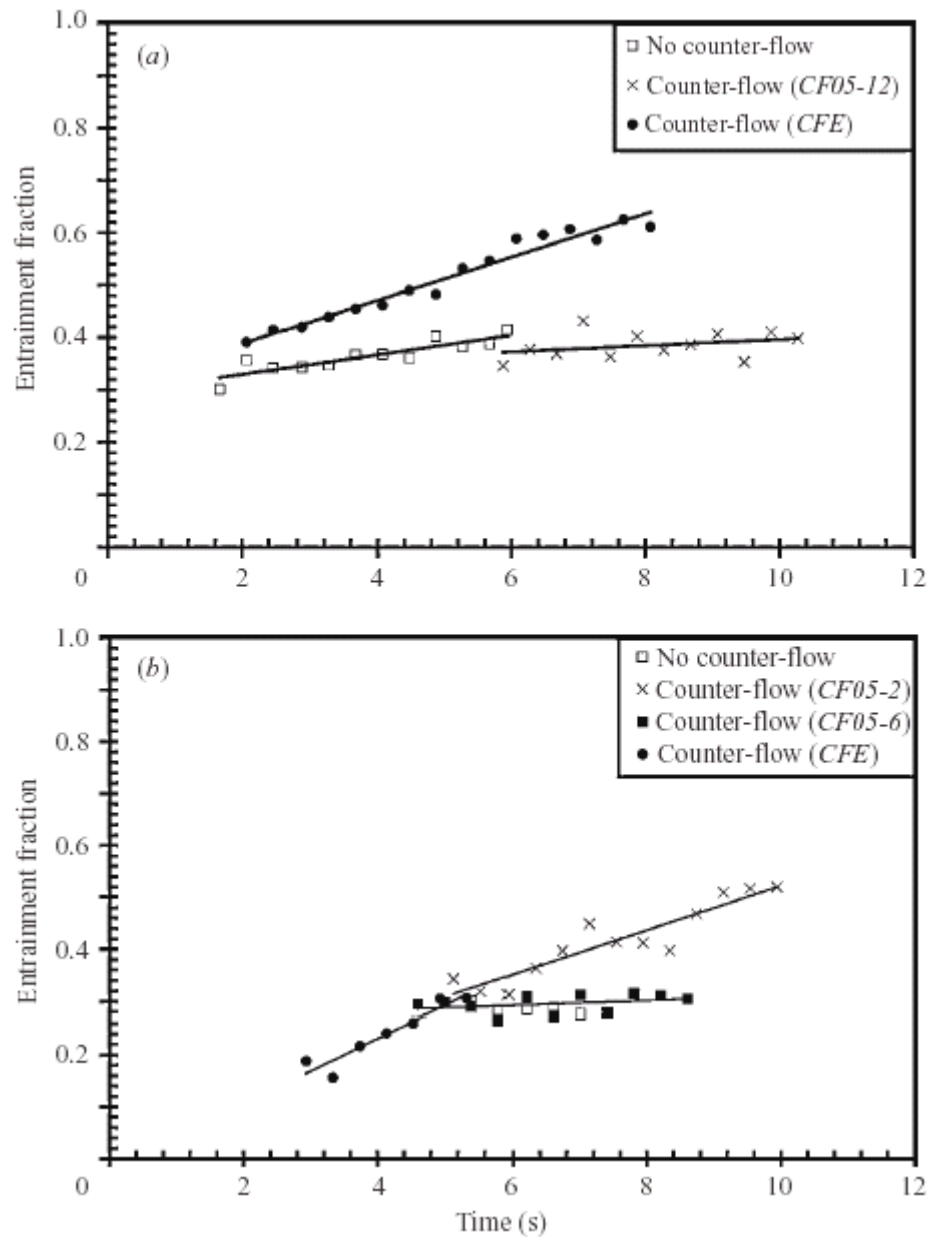


Figure 2.4 Measured entrainment fraction $\eta(t)$ for each counter-flow protocol.
 (a) $L/D = 2$; (b) $L/D = 4$.

It is immediately evident that an extrapolation of the entrainment data to time $T = 0$ will not lead to the expected condition of zero entrainment fraction at the start of vortex ring formation. This is because convective fluid entrainment is the dominant mechanism at early times, as the generated vortex sheet involutes and captures a substantial portion of

ambient fluid near the exit plane of the vortex generator. This captured fluid persists in the vortex bubble indefinitely. The data collected in figure 2.4 only capture the integrated effect of this early entrainment phase, essentially as an initial condition for the diffusive fluid entrainment of the isolated vortex rings studied here. The dynamics of the convective entrainment process during vortex ring formation are beyond the scope of this paper, although it is interesting to observe in passing that the counter-flow appears to also have a measurable effect on early convective entrainment at the stroke ratio $L/D = 4$.

In the absence of counter-flow, the magnitude of fluid entrainment at both piston stroke-to-diameter ratios $L/D = 2$ and $L/D = 4$ was found to lie between 30% and 40% of the bubble volume. These values are higher than those predicted based on a slug model analysis similar to that of Baird et al. (1977). The discrepancy arises due to overestimation of the vortex ring velocity by a boundary-layer-corrected slug model (e.g., Shusser et al. 2002; Dabiri and Gharib 2004a), leading to underestimation of the bubble mass that must share the conserved impulse. The experimental result by Müller and Didden (1980) of a 40% entrained fluid fraction lies within the range observed here. A time-dependent trend in the fluid entrainment is not reported by Baird et al. (1977) or Müller and Didden (1980), limiting any further comparison.

Imposition of a counter-flow was demonstrated to substantially affect fluid entrainment for several of the protocols. An entrainment fraction of nearly 65% was observed for the *LD2-CFE* case, nearly 200% of the entrainment level for vortex rings generated in the absence of counter-flow. Examination of the vorticity distribution generated by each of the protocols provides the insight necessary to explain the mechanism

whereby the process of fluid entrainment is being manipulated. This will be demonstrated in the following development.

An important parameter in the entrainment mechanism described by Maxworthy (1972) is the spatial distribution of vorticity relative to the translating vortex bubble. It is vorticity that has diffused outside the bubble that will reduce the total pressure of ambient fluid near the ring (i.e., by viscous dissipation) to an extent that entrainment can proceed. This relationship can be visualized quantitatively, by superimposing the measured vorticity field on instantaneous streamlines of the flow in the vortex reference frame. Figure 2.5 plots these data for the protocol *LD2-CF0* at times $T = 1.67$ s, 3.54 s, and 5.34 s. The gray patches represent regions of vorticity magnitude above 10% of peak vorticity (10 s^{-1}) in the cores.

Consistent with the model of Maxworthy (1972), the vorticity diffuses beyond the radial extent of the vortex bubble where it will interact with ambient fluid. The thickness of this interacting layer remains steady as the vortex bubble translates, as indicated by the plots at three distinct times during the ring evolution. A similar structure is observed in vortex rings generated by the other protocols. The various counter-flow protocols can be distinguished by observing the evolution of the vorticity profiles in time. Figure 2.6 shows this evolution for cases *LD2-CF0* and *LD2-CFE*. The vorticity profile evolution for vortex rings generated in the absence of counter-flow (i.e., *LD2-CF0*) exhibits broadening of an initially Gaussian vorticity distribution. In the process, the location of peak vorticity remains essentially stationary, with a small movement toward the vortex ring axis of symmetry. Thus, relative to the growing vortex bubble, the location of peak vorticity is moving away from the ambient fluid on the opposite side of the bounding streamsurface.

By contrast, as the vortex rings generated by protocol *LD2-CFE* grow, the peak vorticity does not decay as rapidly and its location moves radially away from the vortex ring axis of symmetry (figure 2.6*b*). These effects should enhance the strength of vorticity in the dissipation region, amplifying ambient fluid entrainment. The measurements shown in figure 2.4 confirm this prediction.

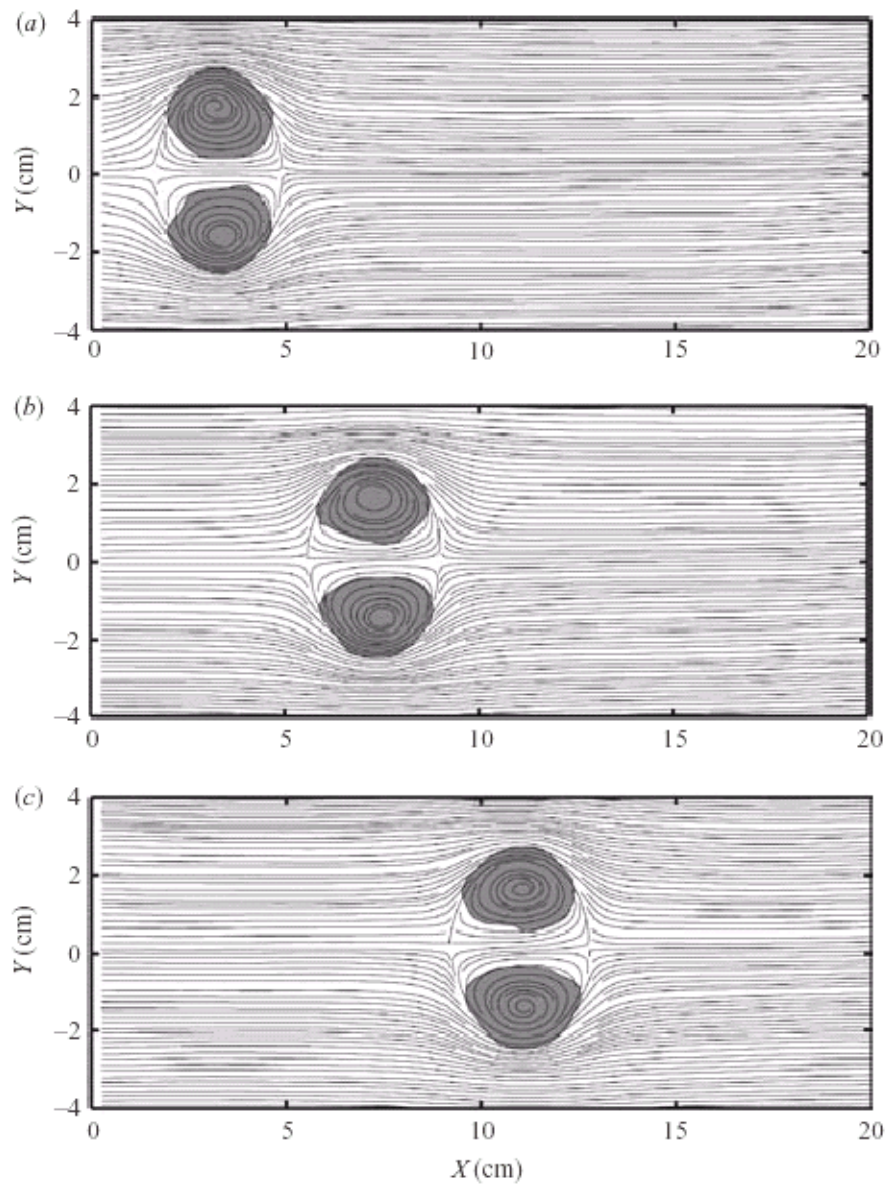


Figure 2.5 Instantaneous streamlines and vorticity patches for protocol *LD2-CF0*.
 (a) $T = 1.67$ s; (b) $T = 3.54$ s; (c) $T = 5.34$ s. Minimum vorticity level is 1 s^{-1} .

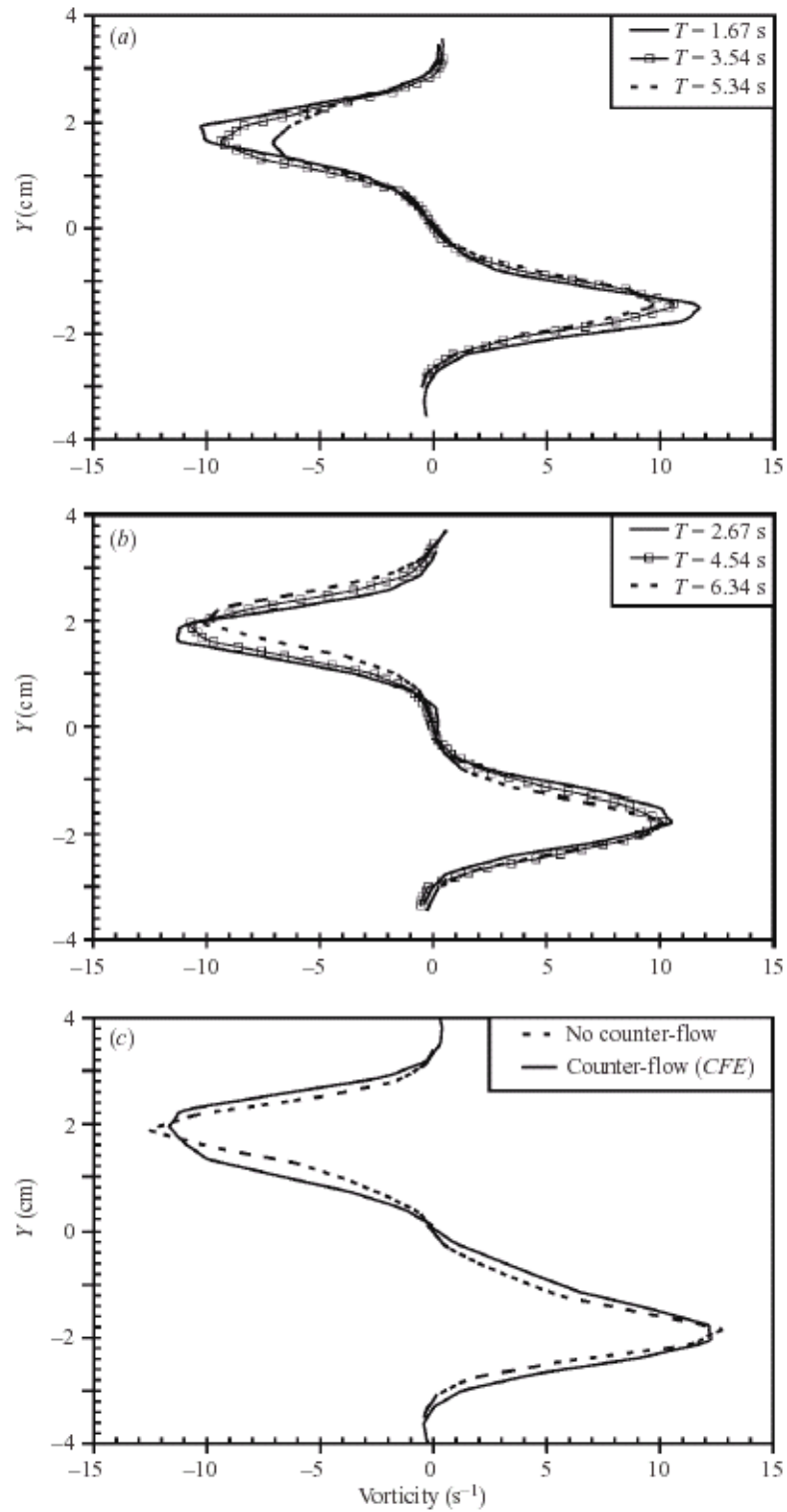


Figure 2.6 Measured vortex ring core vorticity profiles. (a, b) Temporal evolution of vortex ring vorticity profile for protocols *LD2-CF0* and *LD2-CFE*, respectively; (c) vorticity profiles for protocols *LD4-CF0* and *LD4-CFE* at time $T = 2.0$ s.

If this physical mechanism is consistent, one can also anticipate that thicker vortex rings—with broader vorticity distribution reaching closer to the bounding streamsurface—will also have enhanced fluid entrainment, relative to a vortex ring with similar aspect ratio but sharper vorticity decay in the radial direction. This, too, is confirmed in the measurements, as indicated by comparison of the vorticity profiles of protocols *LD4-CF0* and *LD4-CFE* in figure 2.6(c) and their corresponding entrainment measurements in figure 4.

An additional dynamical process becomes important to the fluid entrainment mechanism for vortex rings generated at piston stroke-to-diameter ratios L/D greater than the formation number F . Under these conditions, it has been demonstrated in experiments (Gharib et al., 1998), models (Kelvin, 1875; Benjamin, 1976; Mohseni and Gharib, 1998; Mohseni 2001), and numerical simulations (Mohseni, Ran and Colonius 2001) that the vortex ring possesses maximum energy with respect to impulse-preserving rearrangements of the vorticity. The vortex ring cannot accept additional fluid from the vortex generator without violating this energy maximization, leading to the observed pinch-off. Shusser and Gharib (2000) provide an equivalent statement of this maximization principle and predict that pinch-off occurs when the velocity of fluid from the vortex generator falls below that of the translating ring. Since the velocity of the ambient fluid is less than that of the vortex generator fluid trailing behind the ring, ambient fluid entrainment must also be prohibited after vortex ring pinch-off.

This absence of fluid entrainment is observed for protocols *LD4-CF0* and *LD4-CF05-6*, in which the stroke length-to-diameter ratio of the vortex generator ($L/D = 4$) is greater than the formation number ($F = 3.6$). The entrained fluid fraction is unchanged

from its value at the end of the convective entrainment process (i.e., at vortex ring pinch-off). Interestingly, we do observe substantial fluid entrainment for protocols *LD4-CF05-2* and *LD4-CFE* well above the formation number F , despite the fact that these rings were generated at the same L/D as the non-entraining vortex rings. The apparent contradiction is resolved by the observation that the vortex rings generated by protocols *LD4-CF05-2* and *LD4-CFE* do not experience pinch-off. The effect of counter-flow on the shear layer dynamics is to delay vortex ring pinch-off (Dabiri and Gharib 2004b). Only a minor delay in pinch-off was necessary in the present case, since the stroke length-to-diameter ratio of the vortex generator is only slightly greater than the formation number. However, the delay was sufficient to prevent pinch-off and facilitate fluid entrainment. By contrast, the counter-flow implemented in protocol *LD4-CF05-6* was initiated after the formation number and therefore could not affect the shear layer dynamics or the pinch-off process.

2.4 Comparison with Maxworthy (1972)

The work of Maxworthy (1972) provides the most complete analysis of the diffusive entrainment process in isolated vortex rings that exists in the literature. Due to limitations in the experimental techniques employed therein, many of the model predictions could not be validated. Experiments conducted here are sufficient to revisit those analyses and make detailed comparisons. The most important predictions made by Maxworthy (1972) are a -1 power-law decay in the vortex ring propagation velocity U_v , a -2/3 power-law decay in vortex ring circulation Γ , and the formation of a small wake behind the vortex ring. It is prudent to note that the equivalent piston stroke-to-diameter ratio L/D in the experiments of Maxworthy (1972) is not known. However, given that pinch-off is not

observed in that study and the Reynolds numbers are in the laminar regime, a comparison with the current results is warranted.

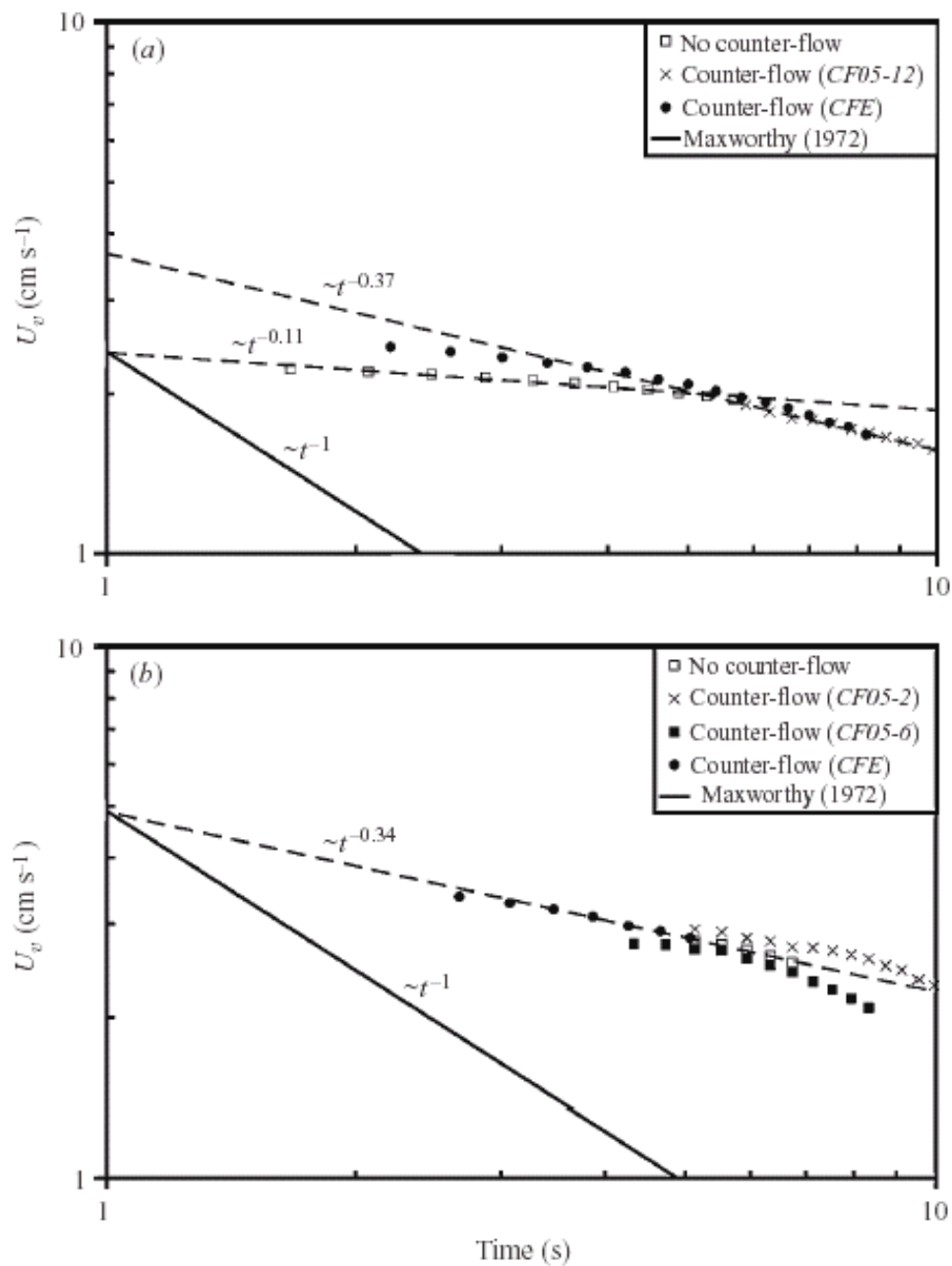


Figure 2.7 Measured vortex ring velocity for each counter-flow protocol. (a) $L/D = 2$; (b) $L/D = 4$.

As mentioned in the previous section, the vortex ring velocity in the laboratory frame of reference was measured in these experiments based on the location of peak vorticity in the cores. By subtracting the counter-flow velocity from this measured value, the ring velocity relative to the fluid U_v was determined for each of the counter-flow protocols. The results are plotted in figure 2.7. It is evident that the decay rate of the vortex ring velocity in each case is much slower than the -1 power-law observed by Maxworthy (1972). For the majority of protocols, the power-law exponent is closer to -1/3. Exceptions to this trend occur for the *LD2-CF0* protocol, in which the ring decays with a further reduced exponent of approximately -1/9; and the late-time motion of rings from protocols *LD4-CF05-2* and *LD4-CF05-6*, which decay at an increasing rate near the end of the measurements.

Although the present measurements are limited to a single decade of time (10^0 to 10^1 s), this is approximately the same data range reported by Maxworthy (1972). Therefore we can reasonably conclude that the rapid decay in vortex ring velocity reported there is not observed here.

The most likely source of the discrepancy in measured vortex ring velocity lies in the initial conditions of vortex ring generation. Whereas the current experiments utilize a piston-cylinder apparatus to generate the rings, Maxworthy (1972) uses a sharp-edged orifice plate. This can present two prominent effects. First, the magnitude of convective fluid entrainment during vortex ring formation can be substantially altered, leading to different initial conditions for the subsequent diffusive entrainment process than those in the present study. Second, the entrainment of opposite-sign vorticity on the downstream-facing wall of the orifice plate will comprise a larger component than in the present

experiments. Maxworthy (1972) predicts the production and convection of this opposite-sign vorticity to affect the dynamics of the evolving vortex rings. It is possible that the translational velocity of the rings is one of the affected parameters, e.g., by vorticity cancellation in the ring, which will reduce its self-induced velocity. The effect of opposite-sign vorticity is further amplified for vortex rings generated at small L/D , in which the relative fraction of opposite-sign vorticity increases.

To predict a temporal trend in the vortex bubble circulation, Maxworthy (1972) uses a model that assumes the vortex ring possesses a nominally constant impulse. The model is admittedly limited to large Reynolds numbers and small time scales, so that impulse loss to the wake behind the ring can be neglected. Nevertheless, a $-2/3$ power-law decay rate in the ring circulation is predicted. Figure 2.8 plots the temporal trends in ring circulation for the protocols tested in these experiments. The decay rates are much slower than predicted by Maxworthy (1972). Specifically, the protocols using $L/D = 2$ decay with a power-law exponent an order of magnitude smaller than that observed by Maxworthy (1972). The circulation of thicker vortex rings at $L/D = 4$ decays slightly faster, but still at a rate much smaller than the $-2/3$ power-law.

It is likely that this discrepancy is due to the fact that the present experiments satisfy neither the requirement of large Reynolds number, nor the assumption of short elapsed time. Hence it is also incorrect to assume a constant impulse for the vortex ring.

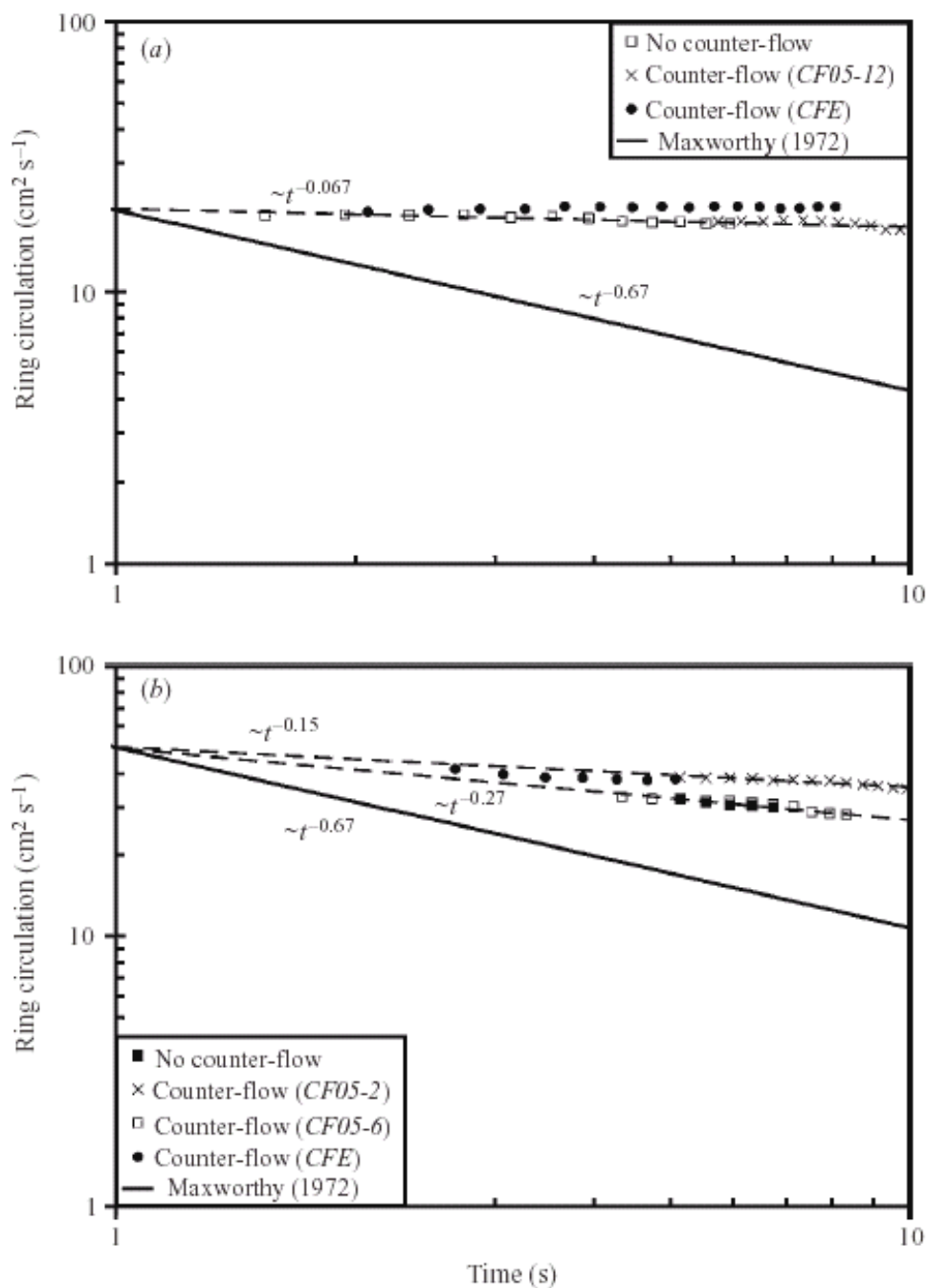


Figure 2.8 Measured vortex ring circulation for each counter-flow protocol. (a) $L/D = 2$; (b) $L/D = 4$. Note that the data symbol convention in (b) has been altered to avoid data point overlap.

Using the analytical method of Maxworthy (1972), one can attempt to estimate the decay rate of the ring impulse based on the measured ring velocity and circulation. The impulse I is related to the ring circulation Γ and the characteristic dimension of the vortex bubble $\Omega_B^{1/3}$ by

$$I = C_1 \Gamma \Omega_B^{2/3}, \quad (2.4.1)$$

where C_1 is a dimensionless constant dependent on the bubble shape. The vortex ring velocity U_v is related to the ring circulation Γ and the characteristic bubble dimension $\Omega_B^{1/3}$ by

$$U_v = C_2 \frac{\Gamma}{\Omega_B^{1/3}}, \quad (2.4.2)$$

where C_2 is also a dimensionless constant dependent on the bubble shape. Therefore the ring impulse goes as

$$I \sim \frac{\Gamma^3}{U_v^2}. \quad (2.4.3)$$

Substituting the measured -1/3 power-law decay for the vortex ring velocity and -1/10 power-law decay for the vortex ring circulation (conservatively), the ring impulse is actually predicted to *increase* with an 11/30 power-law in time! This physically incorrect result of increasing impulse also holds for each of the protocols when the individual velocity and circulation decay rates are input to (2.4.3) in place of the nominal values above. Therefore we must re-examine the model of Maxworthy (1972). Specifically, the following section will show that the non-physical result arises due to the assumption of self-similar vortex bubble growth that is implicit in the use of constant parameters (e.g., C_1 and C_2) to relate the characteristic ring dimension to the actual bubble shape.

Before concluding this section, it is useful to explore the final important prediction of Maxworthy (1972), namely the formation of a wake behind the vortex ring. Figure 2.9 plots the vorticity patches and instantaneous streamlines for a vortex ring formed using protocol *LD2-CF0* at time $T = 5.74$ s. The minimum vorticity level has been reduced to 3% of the peak vorticity in the vortex core in order to visualize regions of low vorticity. As this represents the upper-bound on the measurement error, the data must be interpreted with caution, especially in regions of the flow with large velocity gradients. Nevertheless, the measurement does appear to capture the presence of symmetric vorticity patches behind the vortex ring, in accordance with the prediction of Maxworthy (1972). The existence of this wake structure emphasizes the fact that the increase in vortex ring impulse predicted by the model above must be incorrect. Given the consistency of the observed wake with the aforementioned physical mechanism for diffusive fluid entrainment proposed by Maxworthy (1972), it will henceforth be assumed correct and will be used in the following section to derive an improved quantitative model for the process.

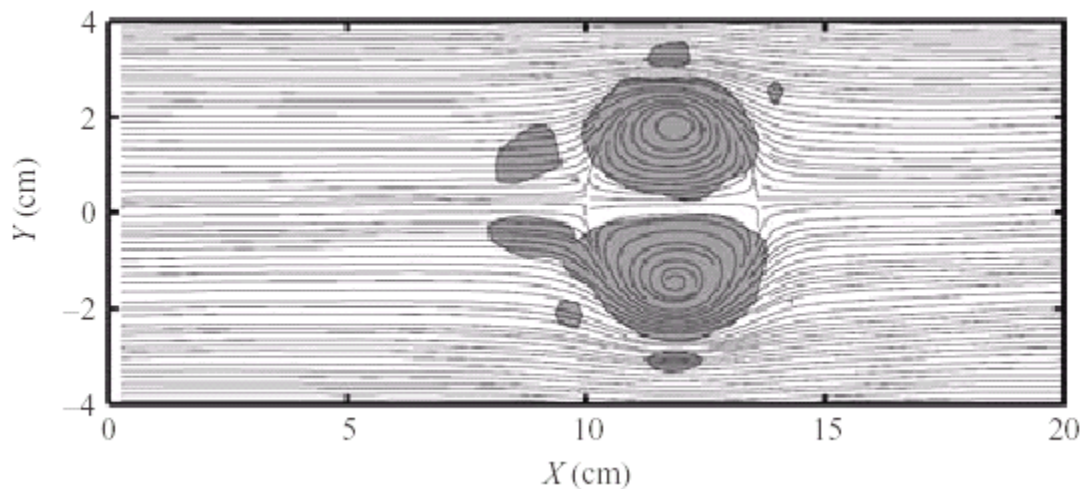


Figure 2.9 Instantaneous streamlines and vorticity patches for protocol *LD2-CF0*. Time $T = 5.74$ s. Minimum vorticity level is 0.3 s^{-1} .

2.5 A Quantitative Model for Diffusive Fluid Entrainment

The physical process of diffusive entrainment is assumed to be essentially that of Maxworthy (1972), as described in the Introduction. Our model will make the corollary assumption that the fraction of ambient fluid flux into the dissipation region that is entrained by the vortex ring is proportional to the fraction of energy lost by the ambient fluid in the same region, i.e.,

$$\frac{d\Omega_B/dt}{d\Omega_D/dt} \sim \frac{dE_L/dt}{dE_I/dt}, \quad (2.5.1)$$

where $d\Omega_B/dt$ is the flux of entrained fluid from the dissipation region into the vortex ring, $d\Omega_D/dt$ is the total flux of fluid into the dissipation region, dE_L/dt is the rate of ambient fluid energy loss due to viscous dissipation in the dissipation region, and dE_I/dt is the rate of ambient fluid energy entering the dissipation region.

The rate of energy loss dE_L/dt (per unit mass) is computed using the two-dimensional incompressible dissipation function Φ in the energy equation (i.e., the scalar product of the momentum equation with the velocity vector u ; see Batchelor (1967):

$$\frac{dE_L}{dt} = \Phi = 2\nu \left[\left(\frac{\partial u}{\partial x} \right)^2 + \left(\frac{\partial v}{\partial r} \right)^2 + \frac{1}{2} \left(\frac{\partial v}{\partial x} + \frac{\partial u}{\partial r} \right)^2 \right], \quad (2.5.2)$$

where u and v are the velocity components in the axial x and radial r directions, respectively. The magnitude of the dissipation function will be proportional to the kinematic viscosity ν , and to a characteristic speed U_v and length scale $\Omega_B^{1/3}$ over which changes in fluid velocity occur, i.e.,

$$\frac{dE_L}{dt} = \Phi = S_1 \nu U_v^2 \Omega_B^{-2/3}. \quad (2.5.3)$$

In (2.5.3), S_1 is a dimensionless shape factor that is dependent on time and other parameters to be delineated shortly. This is distinct from the assumption of constant shape factors used by Maxworthy (1972).

The rate of ambient fluid energy entering the dissipation region (per unit mass) is directly proportional to the square of the fluid velocity and inversely proportional to the time scale over which the process occurs:

$$\frac{dE_I}{dt} = U_v^2 T_d^{-1}. \quad (2.5.4)$$

This characteristic dissipation time scale T_d can be replaced by the characteristic velocity and bubble dimension as $T_d = S_2 \Omega_B^{1/3} U_v^{-1}$, where S_2 is a second dimensionless shape factor.

With this substitution, (2.5.4) becomes

$$\frac{dE_I}{dt} = S_2 U_v^3 \Omega_B^{-1/3}. \quad (2.5.5)$$

Finally, the volume flux of fluid into the dissipation region is

$$\frac{d\Omega_D}{dt} = S_3 (\nu T_d)^{1/2} \Omega_B^{1/3} U_v = S_2^{1/2} S_3 \nu^{1/2} \Omega_B^{1/2} U_v^{1/2}, \quad (2.5.6)$$

where the radial extent of the dissipation region is proportional to $(\nu T_d)^{1/2}$. Substituting (2.5.3), (2.5.5), and (2.5.6) into (2.5.1) gives an expression for the vortex bubble growth as a function of the characteristic ring velocity and dimension, and the shape factors:

$$\frac{d\Omega_B}{dt} = S_1 S_2^{-1/2} S_3 \nu^{3/2} U_v^{-1/2} \Omega_B^{1/6}. \quad (2.5.7)$$

Henceforth, we will consider a dimensionless lumped shape factor $S = S_1 S_2^{-1/2} S_3$ and unit viscosity. As mentioned above, the shape factor is no longer assumed constant, and is instead dependent on time and the set of parameters that will affect the shape and size of the ring from the start of diffusive entrainment: the instantaneous circulation of the ring $\Gamma(t)$; the duration of vortex generator fluid ejection T_e ; the rate of change of the entrained fluid fraction $d\eta/dt$; and the vortex generator exit diameter D . Given this functional dependence, the shape factor can be expressed in terms of a single dimensionless parameter,

$$S = \hat{S} \frac{d\eta}{dt} \Gamma D^{-2} T_e t, \quad (2.5.8)$$

where \hat{S} is a dimensionless constant. Substituting for S in (2.5.7) using this result and rearranging with the use of (3.2), we obtain

$$\Omega_B(t) = \Omega_B^0 + \tilde{S} \Gamma(t)^{6/11} D^{-12/11} T_e^{6/11} \Omega_J^{6/11} U_v(t)^{-3/11} t^{6/11}. \quad (2.5.9)$$

Note that (2.5.9) is dimensionally correct with $\tilde{S} = \hat{S}^{6/11}$ as a dimensionless constant, when the unit viscosity from (2.5.7) is included. The time variable t in (2.5.9) is measured relative to the beginning of diffusive entrainment. Therefore the constant Ω_B^0 is included as the volume of the vortex bubble at the beginning of the diffusive entrainment phase. The magnitude of Ω_B^0 will be determined by the dynamics of the preceding convective entrainment phase. In the following, Ω_B^0 will be estimated based on the earliest data points in each measurement series, although it is recognized that each measurement did not necessarily commence immediately after the convective entrainment phase.

The large number of parameters in (2.5.9) may be reduced via simplifying assumptions regarding the dependence of the vortex ring velocity $U_v(t)$ on its circulation (e.g., Norbury, 1973), and the dependence of the circulation on the variables Ω_j , D , and T_e (e.g., slug model approximation, cf. Shariff and Leonard, 1992). However, since the data for every parameter are readily available in the present case, we will not implement those approximations at this time.

Figure 2.10 plots the predicted vortex bubble growth law in (2.5.9) for each of the counter-flow protocols (excluding the non-entraining protocols *LD4-CF0* and *LD4-CF05-6*), along with the measured vortex bubble growth in each case. The shape constant for each curve is indicated in the figure. A consistently high level of agreement is observed in each case, with the exception of the late-time behavior of protocol *LD2-CFE*. This discrepancy is probably due to the close proximity of the ring to the vortex generator, as indicated by its trajectory in figure 2.2. It appears that the vortex generator may have prevented normal deposition of ring circulation into a wake, allowing the ring to achieve substantially enhanced entrainment at later times when the ring circulation is normally decaying. This explanation is supported by the observed lack of ring circulation decay for protocol *LD2-CFE* in figure 2.8. Although this result emphasizes the role of vorticity distribution in the entrainment process, these modified entrainment dynamics cannot be captured by the current model.

The dimensionless shape constant \tilde{S} is of order unity and exhibits only modest variation across the range of experimental results. It appears that the constant scales with increasing entrainment enhancement, but the current data are insufficient to draw firm conclusions.

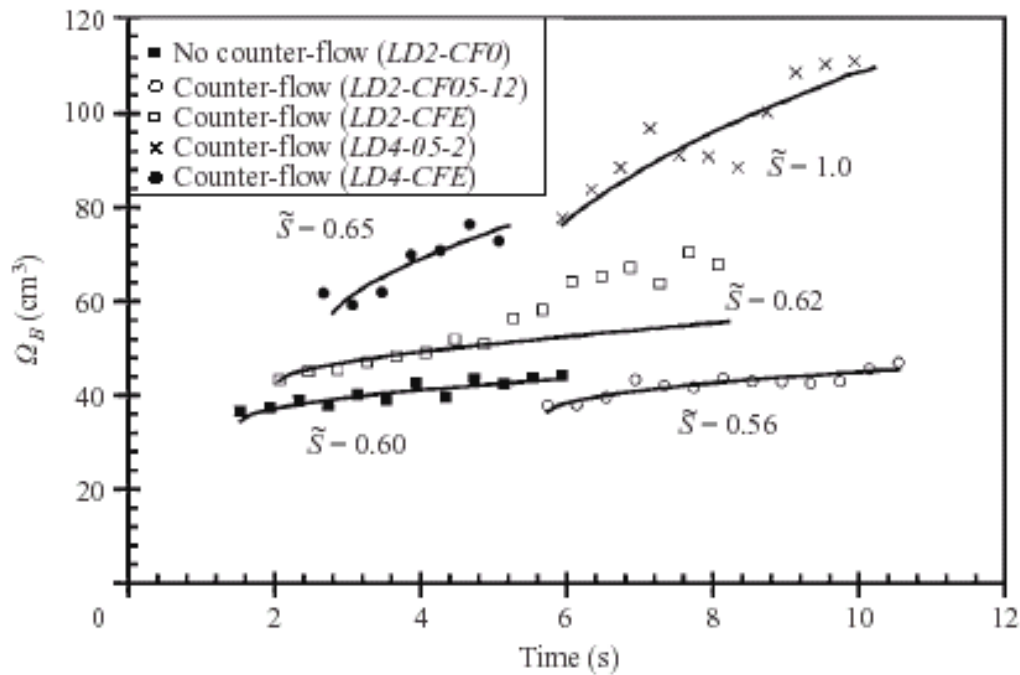


Figure 2.10 Comparison of predicted vortex growth to experimental measurements. Non-entraining protocols (i.e., *LD4-CF0* and *LD4-CF05-6*) are excluded.

2.6 Conclusions

Novel experimental techniques have been developed to probe the dynamics of isolated vortex rings. The counter-flow protocols have enabled empirical study of vortex ring evolution in a moving frame of reference, effectively eliminating many of the common obstacles to progress in previous efforts. Quantitative velocimetry has elucidated the structure of the rings, and a diverse set of experimental conditions has indicated the special role of vorticity distribution and vortex ring pinch-off in the diffusive process of ambient fluid entrainment. In a normal diffusive process (i.e., without counter-flow enhancement), entrained fluid fractions between 30% and 40% were measured. Various counter-flow protocols demonstrated the possibility of substantial entrainment augmentation, up to a 65% entrained fluid fraction in these experiments.

Wake formation behind vortex rings during the entrainment process was observed in these experiments, confirming the physical model for diffusive entrainment suggested by Maxworthy (1972). The corresponding measurements of ring velocity and circulation showed substantial discrepancy, however. Differences in observed ring velocity are probably due to dissimilar boundary conditions in the vortex generator of the previous experiments and the current study, while the overestimate in predicted circulation decay can be attributed to the invalid assumptions of constant ring impulse and self-similar growth in the previous analysis. The present results should serve to caution efforts to describe vortex ring dynamics using constant-impulse or constant-volume assumptions. Although such approximations may be reliable early in the diffusive stage of fluid entrainment, they are inappropriate during both ring formation and late-time ring propagation.

A model for diffusive fluid entrainment has been developed here that does not assume a self-similar shape for vortex rings as they evolve, nor does it require a nominally constant ring impulse. Dimensional analysis and physical arguments were used to derive the growth rate of the vortex bubble as a function of ring circulation and propagation speed. Predictions of the model were found to agree well with measurements of the normal diffusive entrainment process, and it is hypothesized that the shape constant \tilde{S} may scale with increasing entrainment enhancement. Unfortunately, the discovery that the vortex rings do not evolve self-similarly limits our ability to predict trends in the ring impulse using formulae from thin-core approximations or steady solution families (e.g., Fraenkel, 1972; Norbury, 1973).

Future efforts must be directed toward achieving a better understanding of the rapid convective entrainment process that occurs during vortex ring formation. One can infer from the present experiments that this early phase of entrainment will be responsible for much of the entrained fluid fraction that persists in the vortex rings. The current experimental method was not sufficiently accurate to resolve that convective entrainment process, but it is possible that a refinement of the technique introduced here might be effective. Despite the absence of dynamical information regarding the convective fluid entrainment process, the present experiments have definitively shown a substantial contribution of ambient fluid entrainment to the dynamics of vortex rings. As improved ideal vortex ring models are being developed, it will be prudent to account for this phenomenon.

These results may have important implications for pulsed jet systems that possess a capability to manipulate the vortex ring velocity and/or vorticity distribution. Notwithstanding the many manmade applications that may be designed to exploit these parameters in the future, various animals may have already achieved success in this endeavor. For example, it is known that many pulsed-jet animal swimmers that are dependent on self-generated vortical flows for feeding are narrowly tuned for a specific swimming speed regime. Since the relative speed of vortex rings generated during swimming is coupled to the prevalent swimming speed regime of the animal, it will be interesting to further examine the relationship between swimming regime and the effectiveness of entrainment mechanisms in these animals.

2.7 Chapter References

- Baird, M. H. I., Wairegi, T. and Loo, H. J. 1977 Velocity and momentum of vortex rings in relation to formation parameters. *Can. J. Chem. Engng.* **55**, 19-26.
- Batchelor, G. K. 1977 *An Introduction to Fluid Dynamics*. Cambridge University Press.
- Benjamin, T. B. 1976 The alliance of practical and analytical insights into the non-linear problems of fluid mechanics. In *Applications of Methods of Functional Analysis to Problems in Mechanics* (ed. P. Germain and B. Nayroles). Lecture Notes in Mathematics, vol. 503, pp. 8-28. Springer.
- Dabiri, J. O. and Gharib, M. 2004a A revised slug model boundary layer correction for starting jet vorticity flux. *Theor. Comput. Fluid Dyn.* **17**, 293-295.
- Dabiri, J. O. and Gharib, M. 2004b Delay of vortex ring pinch-off by an imposed bulk counter-flow. *Phys. Fluids* **16**, L28-L30.
- Fraenkel, L. E. 1972 Examples of steady vortex rings of small cross-section in an ideal fluid. *J. Fluid Mech.* **51**, 119-135.
- Gharib, M., Rambod, E. and Shariff, K. 1998 A universal time scale for vortex ring formation. *J. Fluid Mech.* **360**, 121-140.
- Kelvin, W. T. 1875 Vortex statics. *Collected Works* vol. 4, pp. 115-128. Cambridge University Press.
- Krueger, P. S., Dabiri, J. O. and Gharib, M. 2003 The formation number of vortex rings formed in the presence of uniform background co-flow. *Phys. Fluids* **15**, L49-L52.
- Lies, C. and Didden, N. 1976 Experimente zum einfluss der anfangsbedingungen auf die instabilität von ringwirblen. *Z. Angew. Math. Mech.* **56**, T206-T208.

- Linden, P. F. and Turner, J. S. 2001 The formation of 'optimal' vortex rings, and the efficiency of propulsion devices. *J. Fluid Mech.* **427**, 61-72.
- Maxworthy, T. 1972 The structure and stability of vortex rings. *J. Fluid Mech.* **51**, 15-32.
- Maxworthy, T. 1977 Some experimental studies of vortex rings. *J. Fluid Mech.* **80**, 465-495.
- Mohseni, K. 2001 Statistical equilibrium theory for axisymmetric flows: Kelvin's variational principle and an explanation for the vortex ring pinch-off process. *Phys. Fluids* **13**, 1924-1931.
- Mohseni, K. and Gharib, M. 1998 A model for universal time scale of vortex ring formation. *Phys. Fluids* **10**, 2436-2438.
- Mohseni, K., Ran, H. Y. and Colonius, T. 2001 Numerical experiments on vortex ring formation. *J. Fluid Mech.* **430**, 267-282.
- Müller, E. A. and Didden, N. 1980 Zur erzeugung der zirkulation bei der bildung eines ringwirbels an einer dusenmundung. *Stroj. Casop.* **31**, 363-372.
- Norbury, J. 1973 A family of steady vortex rings. *J. Fluid Mech.* **57**, 417-431.
- Prandtl, L. and Tietjens, O. G. 1934 *Fundamentals of Hydro and Aeromechanics*. Dover.
- Reynolds, O. 1876 On the resistance encountered by vortex rings, and the relation between vortex rings and the streamlines of a disk. *Nature* **14**, 477.
- Saffman, P. G. 1970 The velocity of viscous vortex rings. *Stud. Appl. Maths* **49**, 371-380.
- Shariff, K. and Leonard, A. 1992 Vortex rings. *Annu. Rev. Fluid Mech.* **24**, 235-279.
- Shusser, M. and Gharib, M. 2000 Energy and velocity of a forming vortex ring. *Phys. Fluids* **12**, 618-621.

- Shusser, M., Gharib, M., Rosenfeld, M. and Mohseni, K. 2002 On the effect of pipe boundary layer growth on the formation of a laminar vortex ring generated by a piston/cylinder arrangement. *Theor. Comput. Fluid Dyn.* **15**, 303-316.
- Widnall, S. E. and Sullivan, J. P. 1973 On the stability of vortex rings. *Proc. R. Soc. Lond. A* **332**, 335-353.
- Willert, C. E. and Gharib, M. 1991 Digital particle image velocimetry. *Exps. Fluids* **10**, 181-193.

CHAPTER 3: A contribution from wake vortex added-mass in estimates of animal swimming and flying dynamics

Submitted to Journal of Experimental Biology February 10, 2005

3.0 Chapter Abstract

Wake analyses are currently the most popular method for studying the dynamics of swimming and flying animals. The effect of the wake vortex structures on locomotion is typically deduced based solely on their rotational momentum. We conduct a case study of the vortex wake generated by free-swimming *Aurelia aurita* jellyfish, as well as a mechanical device that mimics their jetting system, to demonstrate the existence of an additional and substantial dynamical contribution from the irrotational added-mass of the wake vortices. This added-mass contribution is separate from the effects encountered due to acceleration of the animal body and its appendages. These fluid vortex added-mass dynamics are neglected in current methods of quantitative wake analysis, but should be included in order to achieve accurate estimates of locomotive dynamics.

3.1 Introduction

The vortex wake is the fluid dynamical signature of swimming and flying animals. It can be studied to infer net thrust or drag in an accelerating animal or probed to determine the relative contributions to lift and forward motion in steady locomotion.

Current studies of wake vortex dynamics focus on the rotational momentum of the vortices. The magnitude of rotational momentum in the region V downstream from the animal can be determined from the vorticity distribution $\boldsymbol{\omega}(\mathbf{x})$ via the hydrodynamic

impulse in the flow, defined as $\mathbf{I} \sim \int \mathbf{x} \times \boldsymbol{\omega} dV$. This integral of the first moment of vorticity is then related to non-conservative external forces \mathbf{F} acting on the flow by the equation $d\mathbf{I}/dt = \int \mathbf{F} dV$ (Saffman, 1992). When discrete vortices arise in the wake, current models of their dynamics will either use these formulae directly, or apply simplifying approximations regarding the distribution of vorticity and its evolution in time (cf. Shariff and Leonard, 1992).

An additional irrotational added-mass contribution to vortex wake momentum has been previously proposed (Weihs, 1977; Sunada and Ellington, 2001). In the simplified analytical treatment of unsteady jet flow by Weihs (1977), it was suggested that coherent ring vortex structures in the flow would exhibit dynamic behavior similar to solid bodies with equivalent geometric dimensions. In particular, the fluid structures would exhibit an added-mass effect in which fluid external to the vortices experiences a net drift in the direction of ring vortex translation without actually being entrained into the vortices. This effect was quantified using an added-mass coefficient C_{AM} , which represents the volume of external fluid drifting downstream with the vortex, as a fraction of the total vortex volume. The coefficient is identical in definition to the index typically used to characterize accelerating solid bodies during swimming and flying motions (e.g., Batchelor, 1967; Daniel, 1984; Dickinson et al., 1999).

Recently, the first empirical measurements of vortex dynamics in a similar unsteady jet flow showed that the impulse delivered to the flow in the form of fluid vortices cannot be fully accounted by considering only the rotational momentum (Krueger and Gharib,

2003). They, too, hypothesized that the effects of wake vortex added-mass might play a role.

Despite a rich literature dealing with the added-mass of animal *bodies* and their appendages, the question of whether *fluid vortices* such as those observed in animal vortex wakes actually exhibit added-mass behavior has not been previously resolved. The induced Lagrangian fluid particle drift (i.e., tracking individual fluid elements) necessary to generate an added-mass effect in vortex flows has not been quantified in any previous study. Hence, the existence of a fluid vortex added-mass effect similar to that observed in solid bodies and multi-phase flows has remained an unproven conjecture.

In this paper, we use quantitative visualizations of *Aurelia aurita* jellyfish and a mechanical analogue, to demonstrate an important dynamical contribution from added-mass in the vortex wake. This phenomenon is separate from the added-mass contribution of the animal body and appendages and is neglected in current methods of quantitative wake analysis. The techniques described herein allow for the quantification of these missing dynamics in the case of jellyfish swimming and can be readily extended to quantify the wake vortex added-mass dynamics in other animals as well.

Jellyfish were selected as the focus of this proof-of-concept study because they have been observed to form some of the simplest vortex wakes in the animal kingdom, a train of nearly axisymmetric vortex rings (Dabiri et al., 2005). This wake structure can be more easily replicated and quantified in controlled laboratory experiments than fully three-dimensional vortices. Extension of these results to more complex wake structures is proposed in the Discussion.

3.2 Methods

Juvenile *Aurelia* medusae raised at the Cabrillo Marine Aquarium (Long Beach, California, USA) were transferred to a transparent pseudokreisel jellyfish facility at the California Institute of Technology for quantitative flow visualization experiments using digital particle image velocimetry (DPIV; Willert and Gharib, 1991). A 532-nm planar laser sheet illuminated 14- μm glass beads seeded throughout the pseudokreisel saltwater supply. These particles were quantitatively tracked to measure the instantaneous velocity field surrounding the animals. Neither the laser sheet nor the particles were observed to affect the swimming behavior of the jellyfish during the flow measurements. All flow visualization data were collected from animals swimming in regions of the tank at least 2 body diameters from the side walls and 5 body diameters from the tank floor, and with their bodies oriented approximately symmetric in the plane of the laser sheet. In addition, only animals swimming in isolation (i.e., away from other medusae) were selected for flow visualization.

A mechanical apparatus was constructed to simulate the observed jellyfish wake in repeatable and controlled experiments. Specifically, wake vortex rings were generated using a piston-cylinder apparatus (Dabiri and Gharib, 2004). The device was submerged in water and ejected discrete pulses of fluid with jet length-to-diameter ratio $L/D = 2$ from the open end of a hollow 2.54-cm diameter circular tube. During each pulse, the free shear layer produced by the vortex generator rolled into a single ring vortex that propagated downstream via its self-induced motion. The downstream velocity field created by the vortex generator was measured using the same DPIV technique applied to the free-

swimming jellyfish. All velocity field measurements possess an uncertainty between 1% and 3%, with larger uncertainty occurring in regions with greater spatial velocity gradients.

To determine the Lagrangian particle drift induced by the translation of the generated wake vortices, several sets of “virtual” particles were seeded in the measured vortex generator flow. Prior to wake vortex formation, the particles were initialized with positions in the flow corresponding to several discrete, axisymmetric, planar discs downstream of the vortex generator, each oriented normal to the direction of downstream propagation of the wake vortex rings. Since the DPIV data is two-dimensional, these axisymmetric planes correspond to straight lines in the measured two-dimensional flow, i.e., the planes are viewed in a meridian cross-section. The motion of each planar set of particles was determined by updating the positions of those particles based on the measured instantaneous Eulerian velocity fields from DPIV. Cubic interpolation was used to determine the local velocity to sub-grid resolution.

3.3 Results

Figure 3.1(a) shows the measured vortex wake of a swimming *Aurelia* in a plane near the radial symmetry plane of the animal. Instantaneous streamlines of the flow (i.e., lines tangent to local velocity vector) are used to visualize the wake. This method of visualization is useful for determining the global topology of the flow. A pair of vortex rings is clearly visible in the wake.

Figure 3.1(b) shows a wake vortex ring generated by the mechanical analogue. The vortex ring is propagating downstream away from the apparatus. The topology of this wake vortex ring flow is comparable to that produced by the real jellyfish in figure 3.1(a). Although the mechanical apparatus does not experience an external flow as seen in the

reference frame of the free-swimming animals, previous studies have shown that the vortex ring kinematics and flow topology are qualitatively consistent in the presence of moderate external flows such as those induced during swimming (Krueger et al., 2003).

The full extent of the vortex ring was visualized using the method of Dabiri and Gharib (2004), in which the vortex streamlines are tracked in a frame of reference moving at the translational velocity of the vortices, rather than in the laboratory reference frame (figure 3.1*c*). This latter perspective enables us to observe all of the fluid carried by the vortex ring, information that will be necessary in the following analysis in order to properly investigate the added-mass behavior of the vortices.

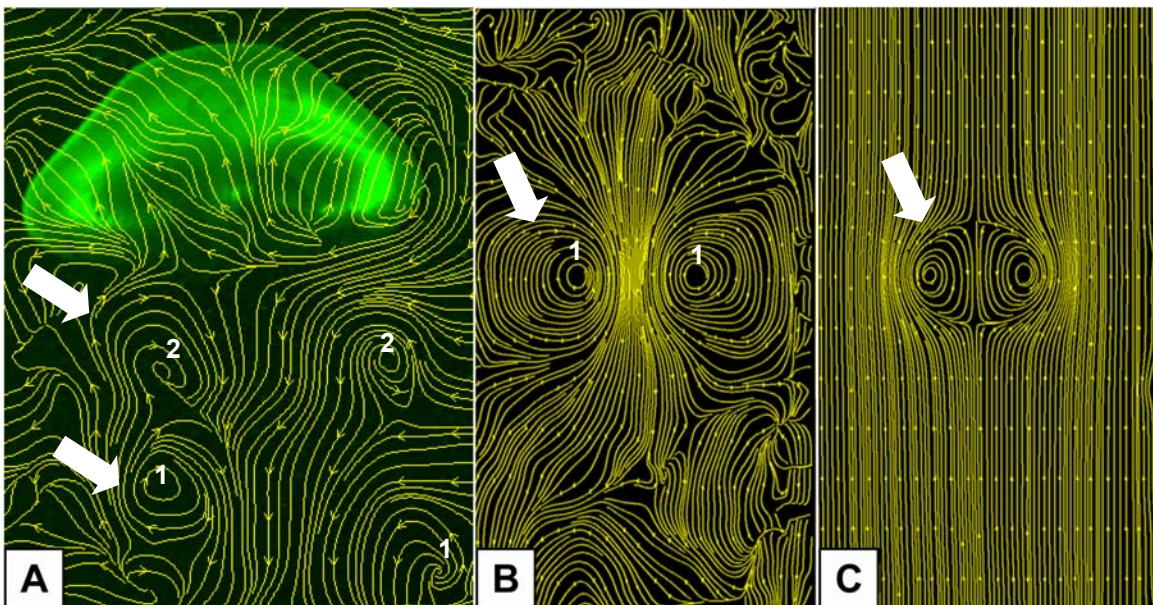


Figure 3.1 DPIV measurements of free-swimming jellyfish and a mechanical analogue. Images are taken in the laser sheet plane, which is aligned close to the plane of symmetry of the flow. (a) Vortex wake of the free-swimming jellyfish consists of a train of nearly axisymmetric vortex rings (white arrows, cores numbered in order of formation). Flow field is approximately 14 cm in height. (b) Vortex ring propagating downstream from the mechanical apparatus. Exit plane of the vortex generator is located at the upper margin of the frame. Flow is vertically downward. Flow field is 20 cm in height. (c) Vortex ring from frame (b) viewed in its propagating reference frame. The full extent of the vortex is clearly visible from this perspective. Flow field is 20 cm in height.

A straightforward heuristic has been previously developed to compute the added-mass of any *solid* body (Darwin, 1953). As the body translates steadily through a plane of initially stationary fluid particles in the flow (oriented normal to the direction of translation), it will induce a net drift of the particles in the direction of body translation. After the body has passed downstream, the volume of fluid Ω_{drift} between the distorted plane and its initial position is equal to the product of the added-mass coefficient and the volume of the solid body Ω_{body} , i.e., $\Omega_{\text{drift}} = C_{\text{AM}} \Omega_{\text{body}}$ (figure 3.2c). Proving this result as a mathematical theorem requires care (cf. Darwin, 1953; Lighthill, 1956; Benjamin, 1986; Eames et al., 1994; Yih, 1997; Eames, 2003); however, the accuracy and robustness of this method has been demonstrated in a variety of experimental studies (e.g., Eames and Duursma, 1997; Bush and Eames, 1998; Eames and Flor, 1998).

The added-mass behavior of a solid sphere traveling through such a planar collection of Lagrangian fluid particles is computed in figure 3.2, using the potential flow stream function for a steadily translating sphere (Milne-Thompson, 1968). The reference plane (shown in cross-section) is distorted to a horn-like shape after passage of the sphere. Interestingly, individual fluid particles do not drift unidirectionally, but instead exhibit looping paths referred to as *elastica* (Darwin, 1953). These elasticas cause the drift volume to undergo a temporal oscillation before achieving the asymptotic value of $0.5 \Omega_{\text{body}}$, consistent with the known added-mass coefficient for a sphere.

Lagrangian particles in the laboratory-generated wake vortex flow were observed to behave in a manner very similar to the inviscid sphere solution (figure 3.3). Looping elastica paths were induced by the translating vortices, and the initially planar surfaces

were again distorted to horn-like shapes. To account for the fact that the translating vortices are increasing in size as they propagate downstream (i.e., due to entrainment of ambient fluid), several planes downstream of the vortex generator were tracked. Each showed similar deformation patterns. The entrainment process is sufficiently slow such that no substantial acceleration of the near wake (and accompanying virtual buoyancy, cf. Batchelor, 1967) is observed to occur in the flow (Dabiri and Gharib, 2004).

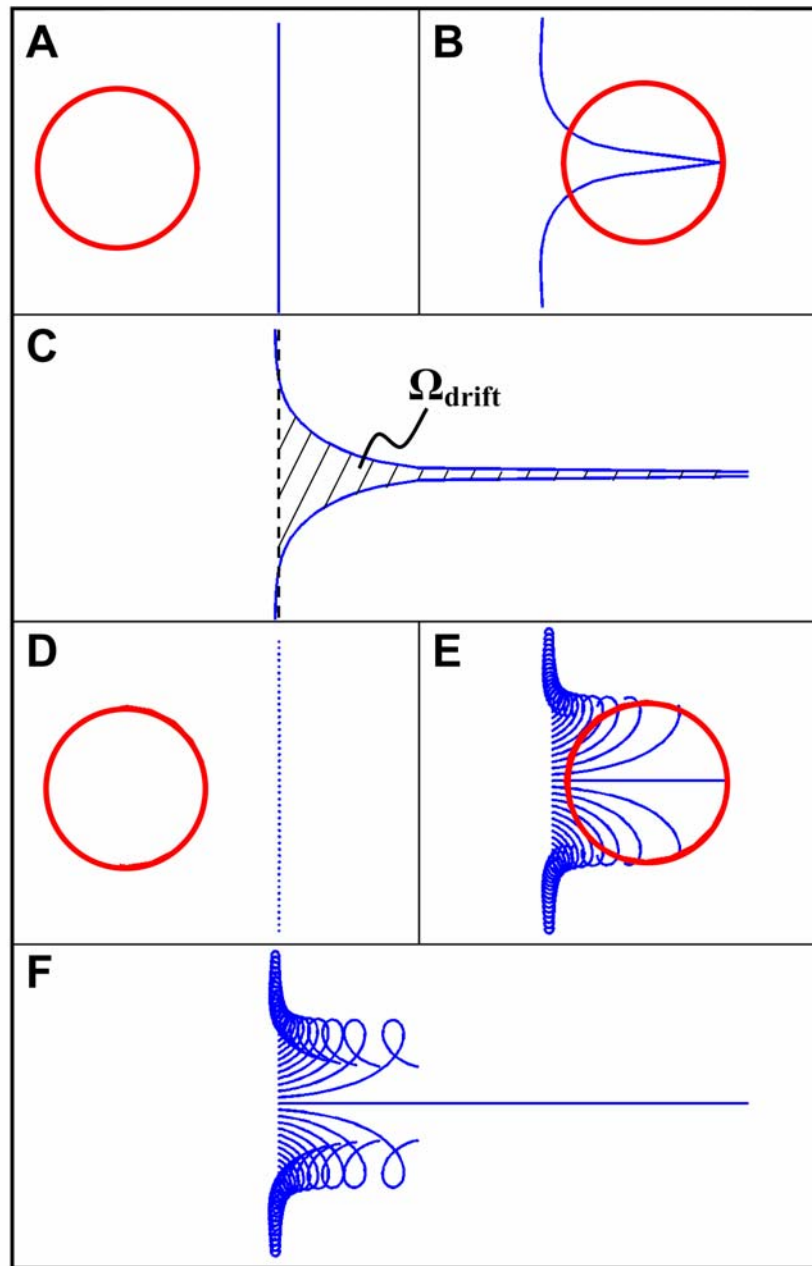


Figure 3.2 Demonstration of heuristic (i.e., Darwin, 1953) for measuring solid body added-mass. Axisymmetric inviscid flow about a solid sphere is shown in cross section. Solutions were computed using dimensional units to allow comparison with experimental results. Sphere radius and propagation speed are 2.54 cm and 1 cm s^{-1} , respectively. Computational domain is 50 sphere radii axially in both directions normal to the reference plane and approximately 12 cm radially. Total fluid drift (i.e., for infinite domain) was computed using measured partial drift in the computational domain and an analytical asymptotic correction factor (i.e., Eames et al., 1994). (a) Sphere approaches initially planar Lagrangian surface from left; $t = 0$ s.

(b) Streamwise distortion of Lagrangian surface occurs as the sphere passes through the plane; $t = 4.45$ s. Note that since only streamwise Lagrangian displacement is plotted, the sphere appears to pass through the plane. Plots of combined streamwise and transverse Lagrangian displacement (e.g., (d)-(f) below) verify that the plane is actually distorted around the sphere. (c) Volume between initial plane and horn-like distorted surface is the drift volume, Ω_{drift} , from which the added-mass coefficient is computed; $t = 13.3$ s. (d)-(f) Individual Lagrangian particle paths corresponding to $t = 0$ s, 4.45 s, and 13.3 s, respectively.

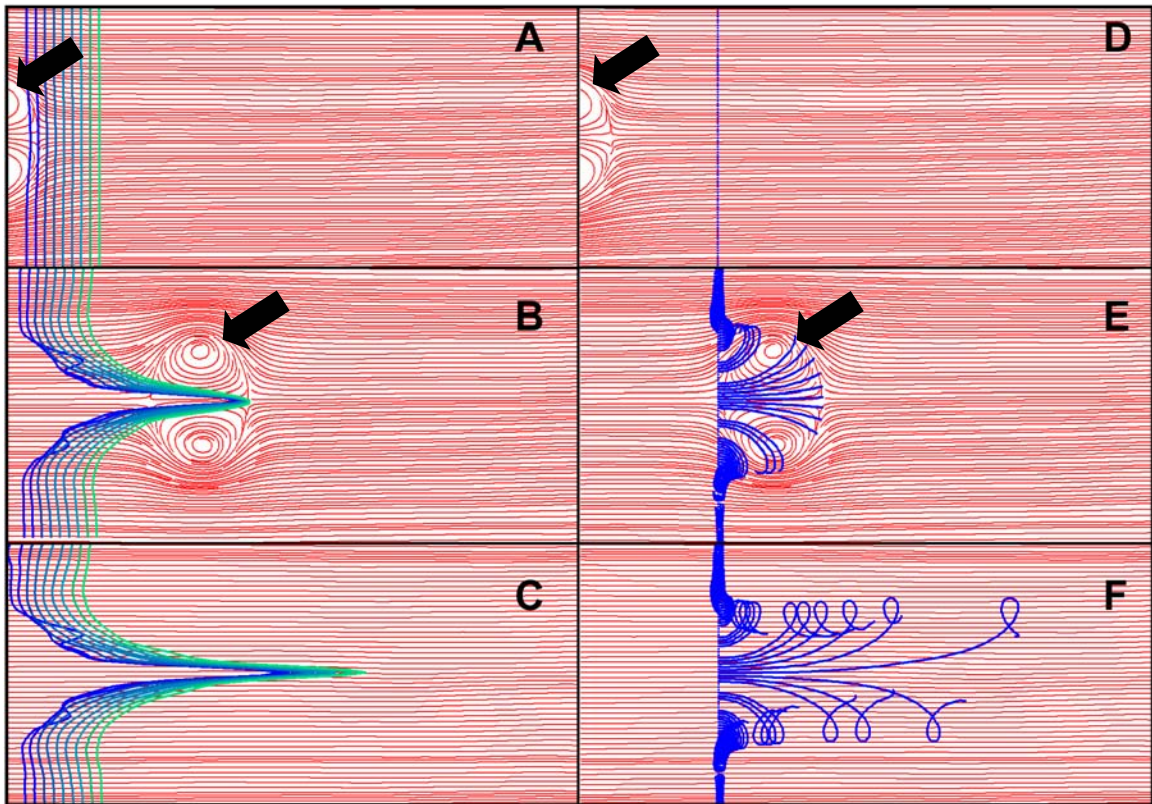


Figure 3.3 Measurements of Lagrangian drift induced by translating fluid vortices. Vortex is indicated by black arrow. (a) Vortex approaches several planar Lagrangian surfaces downstream of the vortex generator (several more planes further downstream not shown); $t = 0.07$ s. (b), (c) Fluid vortices interact with Lagrangian surfaces in a manner similar to that observed for the inviscid sphere solution. Initially planar surfaces are deformed to horn-like shapes; $t = 3.34$ s and 13.3 s, respectively. (d)-(f) Individual Lagrangian particle paths corresponding to $t = 0.07$ s, 3.34 s, and 13.3 s, respectively.

In addition to the volume of each fluid vortex increasing as it propagates downstream, the asymptotic behavior of its associated drift volume also exhibits sustained linear growth rather than saturation at a constant drift volume as was observed for the solid body (figure 3.4). This linear growth in the drift volume reflects the fact that for the observed constant vortex shape (and hence constant added-mass coefficient), the drift volume will continually increase to maintain its magnitude at a constant ratio (i.e., the added-mass coefficient) relative to the growing fluid vortex.

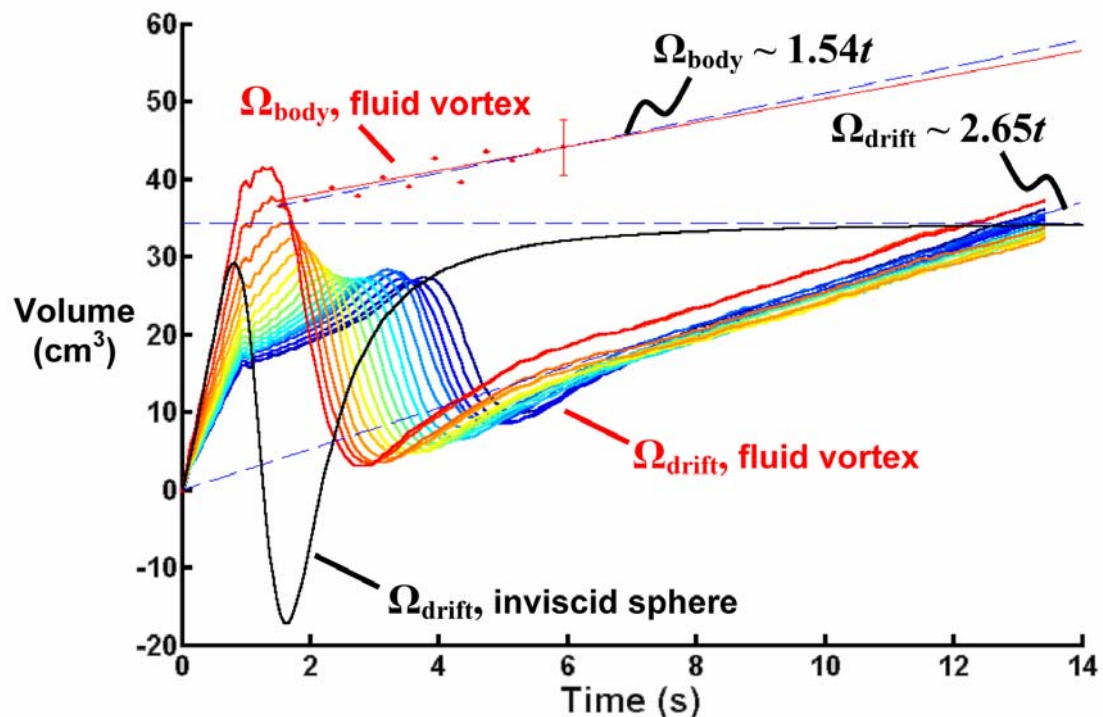


Figure 3.4 Drift and fluid body volume measurements for translating vortices. Colored solid lines: Drift volume of planes initially located in 0.3 cm increments from 2.7 cm (red) to 8.0 cm (blue) downstream of the vortex generator exit. Total fluid drift (i.e., for infinite domain) was computed using measured partial drift in the measurement window and an analytical asymptotic correction factor (i.e., Eames et al., 1994). Closed circles: Measured volume of ellipsoidal fluid vortex. Error bars indicate measurement uncertainty. Dashed blue line: Least-squares linear fit to vortex volume measurements. Solid red line: Linear fit required to exactly match the added-mass coefficient of an equivalent solid body. Inviscid sphere solution is plotted for comparison.

The observed temporal growth of the propagating vortices requires that the heuristic for computing the added-mass coefficient be modified. To properly compute the added-mass coefficient for fluid vortices, we must first subtract the entrained fluid from the total drift volume, i.e., $\Omega_{\text{drift}} - \Omega_{\text{entrained}} = C_{\text{AM}}\Omega_{\text{body}}$, since the entrained fluid is already accounted for in the volume of the vortex, Ω_{body} . In the present case (figure 3.4), the temporal trends in each of these parameters can be measured such that the above equation becomes $2.65t - 1.54t = C_{\text{AM}}(1.54t)$ or, in the limit as $t \rightarrow \infty$ (i.e., so that the vortex has passed far downstream), $C_{\text{AM}} = 0.72$. This is precisely the added-mass coefficient for a *solid* ellipsoidal body with the same shape as the fluid vortices. In figure 3.4, the least-squares linear fit to the vortex volume data is compared with the linear trend required for an exact match to the added-mass coefficient of an equivalent solid body. The agreement is very good.

3.4 Discussion

The present results demonstrate an important contribution to vortex dynamics that is absent from current methods of animal wake analysis, especially those utilizing quantitative wake measurements to estimate locomotive dynamics. The added-mass coefficient of 0.72 measured here indicates that, in addition to transporting fluid via the translating vortices, the vortex generator also indirectly moves an additional mass of fluid whose magnitude is 72 percent of the primary vortex. This is a very substantial improvement in fluid transport that can have profound dynamical effects on animal locomotion. Given the relative magnitude of this effect, it is reasonable to hypothesize that the locomotor could not function as effectively in its absence.

The magnitude of the wake vortex added-mass effect demonstrated here will vary depending on the animal of interest and its locomotive gait. Biological factors affecting vortex formation (e.g., time-dependent boundary conditions, flexible surfaces, etc.) will produce quantitative differences in the wake vortex added-mass effect relative to the mechanical analogue used in these experiments. However, the physical analogy with inviscid body added-mass suggests that the wake vortex added-mass contribution in those cases will remain similar, both qualitatively and in order of magnitude, to the present results.

We have focused on axisymmetric fluid vortices because their propagation is rectilinear and hence only one component of the full added-mass tensor is required in order to characterize their irrotational wake dynamics. Methods more advanced than the current heuristic will be necessary to determine the additional non-zero elements of the added-mass tensor that arise for the large class of animal vortex wakes that do not propagate rectilinearly or unidirectionally.

Nonetheless, the basic physical concept of induced fluid particle drift that led to the added-mass effect measured here is sufficiently general that it should also appear in more complex animal vortex wakes. The vortex wake added-mass effect is also not limited to swimming animals, despite the fact that the present experiments were conducted in water. The bounding streamlines of the fluid vortices (viewed in an appropriate reference frame) mimic the dynamical behavior of solid bodies in inviscid flow via the no through-flow condition that holds at the boundaries; this no through-flow condition appears with equal importance in air, water, or any other fluid medium.

The net contribution of the *solid* body added-mass dynamics to animal locomotion typically vanishes in a time-periodic flow (Daniel, 1984). However unlike solid bodies, *fluid* vortex bodies are time-varying in their volume, shape, and associated added-mass. Since the added-mass contributions during vortex acceleration and deceleration will not be identically equal and opposite, the net contribution to the animal swimming and flying dynamics can be non-zero.

An important example is the wake capture mechanism observed prominently in insect flight (e.g., Dickinson et al., 1999) and fish swimming (e.g., Liao et al., 2003). Wake vortex added-mass provides a direct dynamical contribution to this mechanism via the acceleration and/or deceleration of the wake vortices. When the locomotor body and/or appendages interact with fluid vortices, the dynamics of both the vortex and the associated added-mass of the vortex are affected (and *vice versa*, via Newton's third law). How animals effectively exploit the added-mass dynamics during these fluid-structure interactions is an important question that mandates further study.

3.5 Chapter References

- Batchelor, G. K. 1967 *An Introduction to Fluid Dynamics*. Cambridge University Press.
- Benjamin, T. B. 1986 Note on added-mass and drift. *J. Fluid Mech.* **169**, 251-256.
- Bush, J. W. M. and Eames, I. 1998 Fluid displacement by high Reynolds number bubble motion in a thin gap. *Int. J. Multiphas. Flow* **24**, 411-430.
- Dabiri, J. O. and Gharib, M. 2004 Fluid entrainment by isolated vortex rings. *J. Fluid Mech.* **511**, 311-331.
- Daniel, T. L. 1984 Unsteady aspects of aquatic locomotion. *Am. Zool.* **24**, 121-134.
- Darwin, C. 1953 Note on hydrodynamics. *P. Camb. Philos. Soc.* **49**, 342-354.

- Dickinson, M. H., Lehmann F. O. and Sane S. P. 1999 Wing rotation and the aerodynamic basis of insect flight. *Science* **284**, 1954-1960.
- Eames, I. 2003 The concept of drift and its application to multiphase and multibody problems. *Phil. Trans. R. Soc. Lond. A* **361**, 2951-2965.
- Eames, I., Belcher, S. E. and Hunt, J. C. R. 1994 Drift, partial drift and Darwin's proposition. *J. Fluid Mech.* **275**, 201-223.
- Eames, I. and Duursma, G. 1997 Displacement of horizontal layers by bubbles injected into fluidized beds. *Chem. Eng. Sci.* **52**, 2697-2705.
- Eames, I. and Flor, J.-B. 1998 Fluid transport by dipolar vortices. *Dynam. Atmos. Oceans* **28**, 93-105.
- Krueger, P. S., Dabiri, J. O. and Gharib, M. 2003 Vortex ring pinchoff in the presence of simultaneously initiated uniform background co-flow. *Phys. Fluids* **15**, L49-L52.
- Krueger, P. S. and Gharib, M. 2003 The significance of vortex ring formation to the impulse and thrust of a starting jet. *Phys. Fluids* **15**, 1271-1281.
- Liao J. C., Beal D. N., Lauder G. V. and Triantafyllou M. S. 2003 Fish exploiting vortices decrease muscle activity. *Science* **302**, 1566-1569.
- Lighthill, M. J. 1956 Drift. *J. Fluid Mech.* **1**, 31-53.
- Milne-Thompson, L. M. 1968 *Theoretical Hydrodynamics*. Dover Publications.
- Saffman, P. G. 1992 *Vortex Dynamics*. Cambridge University Press.
- Shariff, K. and Leonard, A. 1992 Vortex rings. *Annu. Rev. Fluid. Mech.* **24**, 235-279.
- Sunada, S. and Ellington, C. P. 2001 A new method for explaining the generation of aerodynamic forces in flapping flight. *Math. Method Appl. Sci.* **24**, 1377-1386.
- Weih, D. 1977 Periodic jet propulsion of aquatic creatures. *Forts. Zool.* **24**, 171-175.

Willert, C. E. and Gharib, M. 1991 Digital particle image velocimetry. *Exp. Fluids* **10**, 181-193.

Yih, C.-S. 1997 Evolution of Darwinian drift. *J. Fluid Mech.* **347**, 1-11.

CHAPTER 4: Delay of vortex ring pinch-off by an imposed bulk counter-flow

Submitted to Physics of Fluids October 23, 2003

4.0 Chapter Abstract

The Kelvin-Benjamin variational principle has been previously used to predict that vortex ring pinch-off can be delayed if the energy of the leading vortex ring is decreased during formation and/or the energy delivered by the vortex generator is increased. We present experimental results in which the former and latter energy effects were simultaneously accomplished by imposing a bulk axisymmetric counter-flow during vortex ring formation. Measurements indicate that the formation number is retarded sufficiently to allow increased ingestion of fluid circulation by the leading vortex ring. This serves as a first demonstration of artificial manipulation of vortex ring formation for potential propulsive benefits in starting jets.

4.1 Introduction

Krueger et al. (2001, 2003) recently measured the time-integrated force associated with vortex ring formation in a starting jet and determined that its magnitude is greater than an equivalent steady jet. This result encourages one to imagine the possibility of exploiting arbitrarily large vortex rings for unsteady fluid transport or thrust generation.

The question of whether rings of arbitrary size can be created in practice was not examined until relatively recently. Gharib, Rambod and Shariff (1998) studied the formation of vortex rings using a piston-in-cylinder arrangement. They demonstrated that

at sufficiently large stroke length-to-diameter ratios, the size of the leading vortex ring can no longer be increased. Fluid ejected from the vortex generator subsequent to this limit forms an unstable trailing jet posterior to the ring. Krueger (2001) compared the time-integrated force due to vortex rings formed below and above the limiting stroke ratio and showed that the force production is maximized as the limit is reached.

The discovery and characterization of a limiting process during vortex ring formation has generated substantial interest in the concept of optimal unsteady jet propulsion and methods to delay vortex ring pinch-off. Gharib et al. (1998) and others subsequently have characterized the limiting process as a manifestation of the Kelvin-Benjamin variational principle (cf. Saffman, 1992; Mohseni, Ran and Colonius, 2001; Mohseni and Gharib, 1998; Mohseni, 2001). In effect, the principle predicts the separation of the leading vortex ring from the trailing fluid supply (known as vortex ring pinch-off) when the vortex generator is no longer able to supply energy at a level sufficient for ring growth. Further, the principle dictates that the energy of an axis-touching ring, i.e., one with the core vorticity reaching the symmetry axis asymptotically, is maximized relative to other arrangements of the vorticity with the same impulse.

These developments suggest that in order to delay the pinch-off process, the energy required by the leading vortex ring must be decreased and/or the energy delivered by the vortex generator must be increased during the formation process. The objective of these experiments is to demonstrate both strategies simultaneously, in order to suggest the possibility of achieving propulsive benefits from augmented leading vortex rings in starting jets.

4.2 Methods and Results

By establishing bulk counter-flow in the fluid surrounding a vortex generator, the energy of the forming vortex ring can be altered. Formally, the ring energy is given by (Saffman, 1992)

$$E_{\text{ring}} = \int_V \frac{1}{2} \mathbf{u}^2 dV = 2\mathbf{U} \cdot \mathbf{I} + \int_V (\mathbf{u} - \mathbf{U}) \cdot \mathbf{r} \times \boldsymbol{\omega} dV, \quad (4.2.1)$$

where \mathbf{U} is the vortex velocity, \mathbf{I} is the fluid impulse, \mathbf{u} and $\boldsymbol{\omega}$ are the fluid velocity and vorticity, respectively, and the integration is taken over the ring volume. The first term in the last expression accounts for translational energy while the second term includes the energy of fluid motion in the vortex ring relative to its translating frame of reference. A bulk counter-flow at speed U_{cn} decreases the vortex ring translational velocity, resulting in a concomitant decrease in ring energy:

$$E_{\text{ring}} = 2(\mathbf{U} - U_{cn}) \cdot \mathbf{I} + \int_V (\mathbf{u} - \mathbf{U}) \cdot \mathbf{r} \times \boldsymbol{\omega} dV. \quad (4.2.2)$$

The energy delivered by the vortex generator is also affected by counter-flow, since the exit velocity in the energy equation is measured relative to the bulk velocity of the ambient fluid. Using a format similar to that of Shusser and Gharib (2000),

$$E_{\text{generator}} = \frac{1}{8} \pi D^2 L (U_e + U_{cn})^2, \quad (4.2.3)$$

where D and L are the nozzle exit diameter and stroke length, respectively, and U_e is the exit velocity of the fluid efflux from the vortex generator in a laboratory frame. Equations (4.2.2) and (4.2.3) suggest that counter-flow both decreases the ring energy and increases the vortex generator energy, delaying ring pinch-off.

These hypotheses were tested using the apparatus of figure 4.1. Operation is similar to that described by Krueger, Dabiri and Gharib (2003) for a co-flowing configuration. Measurement of vortex ring circulation was accomplished using digital particle image velocimetry (DPIV, Willert and Gharib, 1991). Neutrally buoyant 20- μm particles were seeded in the flow to scatter incident light from a 532-nm pulsed Nd:YAG laser. The flow field—8 diameters downstream of the nozzle exit and 2.4 diameters radially from the symmetry axis—was captured by a 1024×1024 pixel black-and-white charge-coupled device digital camera (Uniq Vision, Inc.) at 30 Hz. This pixel resolution corresponds to a physical test section resolution of approximately 0.19×0.19 mm and was sufficient to resolve the vortex ring core vorticity distribution.

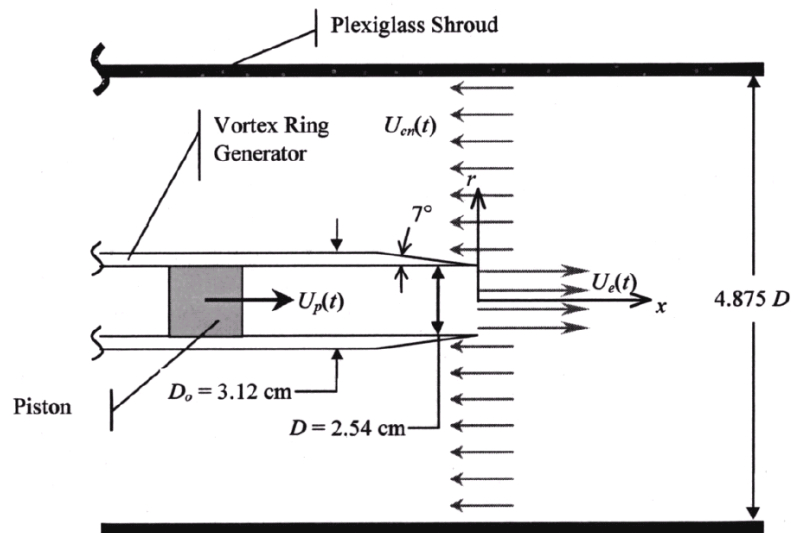


Figure 4.1 Schematic of basic apparatus for counter-flow experiments (adapted from Krueger et al. 2003).

Vortex rings were generated for stroke length-to-diameter ratios L/D of 4 and 12, nominally, at a Reynolds number of 1400 based on the nominal piston speed (5.5 cm s^{-1}) and nozzle exit diameter (2.54 cm). The following counter-flow protocols and

corresponding test names were introduced: $CF0$ = no counter-flow; $CF05-n$ = counter-flow at one half of the nominal piston speed and a $n L/D$ delay in its initiation relative to the start of vortex ring formation (e.g., $CF05-2$ corresponds to a $2 L/D$ delay in counter-flow); CFE = counter-flow matched to the measured instantaneous $CF0$ vortex ring speed.

The counter-flow changed the dynamics of vorticity flux without significantly altering the total circulation delivered by the vortex generator. This is demonstrated by the plots of circulation versus nondimensional time $\hat{t} = (\overline{U}_p - \overline{U}_{cn})t/D$ (where overbars denote running time averages) at stroke ratio 4, shown in figure 4.2.

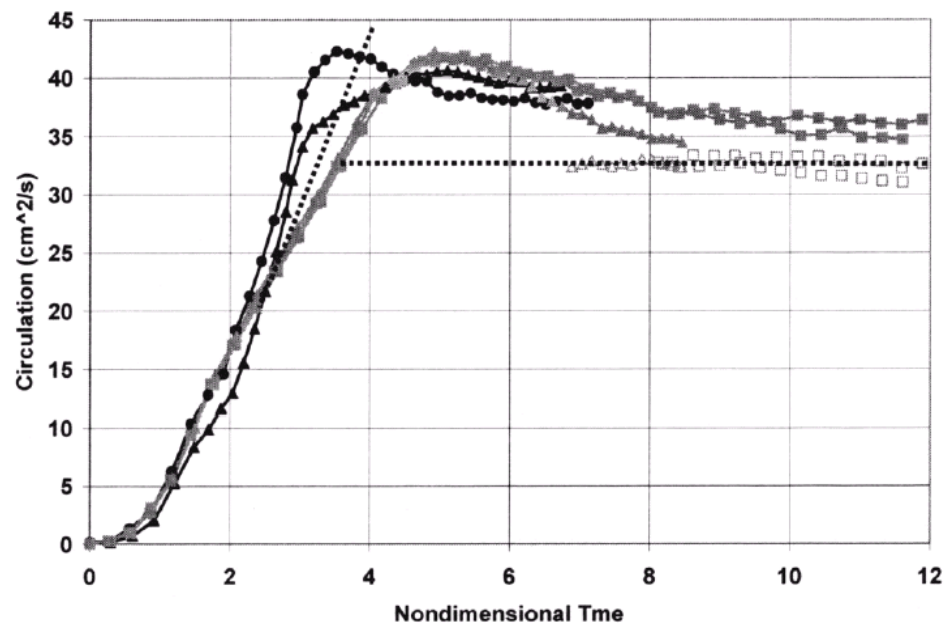


Figure 4.2 Circulation versus nondimensional time for nominal stroke ratio of 4. Gray squares, $CF0$; black triangles, $CF05-2$; gray triangles, $CF05-6$; black circles, CFE . Open symbols represent circulation in pinched-off leading vortex ring.

For the stroke ratio 4, vortex ring pinch-off consistently occurred at nondimensional time near 3.6, where pinch-off was observed at all. This formation number lies in the range observed by Gharib et al. (1998) in the absence of bulk flow. Complete suppression of

vortex ring pinch-off was accomplished for cases *CF05-2* and *CFE*. The angled line in the figure separates trials in which pinch-off was observed (right hand side of line) and those in which all of the circulation ejected from the generator was ingested by the leading vortex ring. From this plot it appears that an increased rate of vorticity flux in nondimensional time is consistently correlated with sustained growth of the leading vortex ring.

It is clear that the delayed pinch-off in the *CF05-2* and *CFE* trials is due in part to the counter-flow being implemented prior to normal vortex ring pinch-off (i.e., $\hat{t} < 3.6$). To be sure, the counter-flow for *CF05-6* is identical in magnitude to the *CF05-2* case, but is initiated after pinch-off has already occurred, and therefore cannot affect the pinch-off dynamics. This is effectively demonstrated in figure 4.3(a), which plots the nondimensional time versus real time and indicates the end point of fluid ejection by the vortex generator.

The trials observed to experience pinch-off of the leading vortex ring (i.e., *CF0* and *CF05-6*) reach the formation number (horizontal line) before the end point of fluid ejection. Accordingly, the leading vortex pinches off and a trailing jet is formed. The two cases in which counter-flow was initiated prior to the normal pinch-off do not reach the formation number until after fluid ejection has terminated. Thus, the leading vortex ring is able to accommodate all of the circulation from the vortex generator. Initiation of counter-flow is indicated by the abrupt decrease in curve slope for cases *CF05-2*, *CF05-6*, and *CFE*.

Similar efforts were made to delay vortex ring pinch-off at a stroke ratio of 12. However, the counter-flow protocols were unable to suppress the nondimensional time

below the formation number for the entire duration of fluid ejection (figure 4.3b). Hence, pinch-off of the leading vortex ring was observed in each trial.

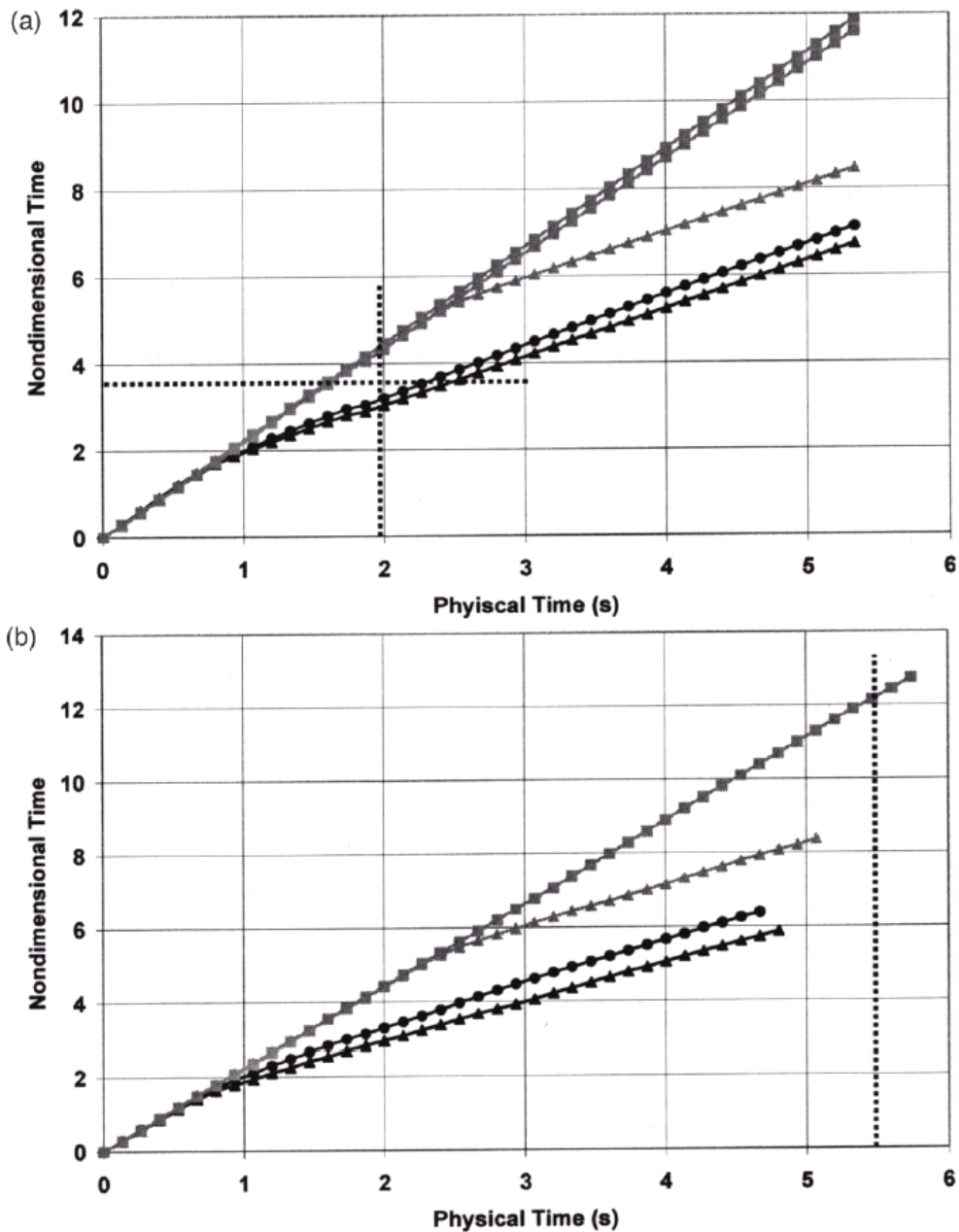


Figure 4.3 Nondimensional time versus physical time. (a) Stroke ratio = 4; (b) stroke ratio = 12. Gray squares, CF_0 ; black triangles, $CF_{0.5-2}$; gray triangles, $CF_{0.5-6}$; black circles, CFE . Vertical line denotes end of fluid ejection. Horizontal line in (a) denotes measured formation number for vortex ring pinch-off.

4.3 Conclusions

These results elucidate important principles governing vortex ring pinch-off in starting jets. Specifically, we have empirically demonstrated the sufficient condition for complete avoidance of vortex ring pinch-off that is suggested by the Kelvin–Benjamin variational principle: the formation time must be suppressed below the formation number until the end of fluid ejection. The use of a counter-flow to reduce vortex ring energy and increase vortex generator energy is a simple but effective mechanism to exploit the salient limiting processes and achieve enhanced vortex ring formation. In the present case, the circulation of the vortex rings that were effectively manipulated by counter-flow was increased by over 25% at peak circulation levels. The increased circulation persists at least 10% above normal levels even at later times (e.g., beyond nondimensional time 8), when a reduction from peak circulation levels occurs due to cancellation of vorticity at the symmetry axis and loss of vorticity into a small wake during the process of fluid entrainment (cf. Maxworthy, 1972). These dissipative mechanisms have been duly noted in both vortex ring experiments and numerical simulations (e.g., Gharib et al., 1998; Mohseni et al., 2001).

The counter-flow technique described here is the first empirical demonstration of effective pinch-off delay. The authors intend to shift focus to methods of pinch-off delay that do not rely on external devices, such as might be accomplished by manipulation of parameters of the vortex generator itself. Because the Kelvin–Benjamin variational principle does not lend itself to immediate interpretation in terms of a physical vortex generator, we will rely on analyses similar to those introduced in equations (4.2.1)–(4.2.3) herein.

4.4 Chapter References

- Gharib, M., Rambod, E. and Shariff K. 1998 A universal time scale for vortex ring formation. *J. Fluid Mech.* **360**, 121-140.
- Krueger, P. S. 2001 The significance of vortex ring formation and nozzle exit overpressure to pulsatile jet propulsion. Ph.D. thesis, California Institute of Technology, Pasadena, CA, 2001.
- Krueger, P. S., Dabiri, J. O., and Gharib, M. 2003 Vortex ring pinch-off in the presence of simultaneously initiated uniform background co-flow. *Phys. Fluids* **15**, L49-L52.
- Krueger, P. S. and Gharib, M. 2003 The significance of vortex ring formation to the impulse and thrust of a starting jet. *Phys. Fluids* **15**, 1271-1281.
- Maxworthy, T. 1972 The structure and stability of vortex rings. *J. Fluid Mech.* **51**, 15-32.
- Mohseni, K. 2001 Statistical equilibrium theory for axisymmetric flows: Kelvin's variational principle and an explanation for the vortex ring pinch-off process. *Phys. Fluids* **13**, 1924-1931.
- Mohseni, K. and Gharib, M. 1998 A model for universal time scale of vortex ring formation. *Phys. Fluids* **10**, 2436-2438.
- Mohseni, K., Ran, H. Y. and Colonius, T. 2001 Numerical experiments on vortex ring formation. *J. Fluid Mech.* **430**, 267-282.
- Saffman, P. G. 1970 The velocity of viscous vortex rings. *Stud. Appl. Maths* **49**, 371-380.
- Saffman, P. G. 1992 *Vortex Dynamics*. Cambridge University Press.
- Shusser, M. and Gharib, M. 2000 Energy and velocity of a forming vortex ring. *Phys. Fluids* **12**, 618-621.

Willert, C. E. and Gharib, M. 1991 Digital particle image velocimetry. *Exp. Fluids* **10**, 181-193.

CHAPTER 5: A revised slug model boundary layer correction for starting jet vorticity flux

Submitted to Theoretical and Computational Fluid Dynamics December 15, 2003

5.0 Chapter Abstract

The flux of vorticity from a piston-cylinder vortex generator is commonly approximated using a model in which the fluid efflux is treated as a uniform slug of fluid with negligible boundary layer thickness. Shusser et al. (2002) introduced a correction to the slug model that accounts for boundary layer growth within the cylinder. We show that their implemented boundary layer solution contains an error, leading to an underestimate of the calculated boundary layer growth. We present a corrected model that agrees more closely with experimental measurements of starting jet vorticity flux and vortex ring core thickness.

5.1 Introduction

When describing the formation of vortex rings from a piston-cylinder apparatus, a slug model for the fluid efflux is often utilized. It is assumed that the starting jet possesses a thin boundary layer so that the velocity at the edge of the boundary layer is approximately equal to the piston velocity (Shariff and Leonard, 1992). The vorticity flux can then be computed as

$$\frac{d\Gamma}{dt}(t) = \int_{BL} \omega_{\phi} u dy \approx \int_{BL} -u \frac{\partial u}{\partial y} dy \approx \frac{1}{2} U_p^2(t), \quad (5.1.1)$$

where the integration is taken in a meridian (x, y) plane across the boundary layer, Γ is the circulation in the flow, ω_ϕ is the azimuthal component of vorticity, u is the axial fluid velocity component, and U_p is the piston speed.

A substantial discrepancy has persisted between empirical measurements of vorticity flux in piston-generated starting jets and theoretical models based solely on parameters of the vortex generator. These models commonly underestimate the vorticity flux by up to 40% at large piston stroke length-to-diameter ratios. A portion of the inconsistency between the slug model of vorticity flux and laboratory measurements can be attributed to boundary layer growth at the inner surface of the cylinder during fluid ejection. As the boundary layer grows, fluid continuity demands a concomitant increase in the jet velocity from the piston to the nozzle exit plane of the vortex generator. To incorporate this effect in the slug model, Shusser et al. (2002) implemented a Rayleigh-Stokes solution for an infinite plate in the following form:

$$u = U_p \operatorname{erf}\left(\frac{y}{\sqrt{\nu t}}\right), \quad (5.1.2)$$

where ν is the kinematic viscosity of the fluid and erf is the error function. Using this velocity profile and the continuity equation, the jet velocity at the nozzle exit plane U_e is given by

$$U_e = U_p \left(1 + \frac{4}{\sqrt{\pi}} \frac{1}{\sqrt{\operatorname{Re}}} \sqrt{\frac{L}{D}}\right), \quad (5.1.3)$$

where L is the piston stroke length, D is the nozzle exit diameter, and Re is the Reynolds number based on the piston velocity and nozzle exit diameter. The exit velocity in (5.1.3) then replaces the piston velocity in the slug model equation (5.1.1).

5.2 Revised Correction

Closer examination of the boundary layer correction by Shusser et al. (2002) reveals that the implemented solution in (5.1.2) above is not a solution to the boundary layer equations. To be sure, the source that they cite for the solution includes an additional factor of two in the denominator of the error function (Rosenhead, 1963):

$$u = U_p \operatorname{erf}\left(\frac{y}{2\sqrt{vt}}\right), \quad (5.2.1)$$

Equation (5.2.1) is a solution to the boundary layer equations, and implementing this in favor of (5.1.2) results in a small but crucial correction to (5.1.3) above:

$$U_e = U_p \left(1 + \frac{8}{\sqrt{\pi}} \frac{1}{\sqrt{\operatorname{Re}}} \sqrt{\frac{L}{D}}\right), \quad (5.2.2)$$

where the second term in parentheses has increased by a factor of two.

Figure 5.1 plots the circulation growth predicted by this new correction, along with the classical slug model, the errant correction, and experimental data. The slope of the new curve—the vorticity flux—is very nearly matched to experimental data measured using digital particle image velocimetry (DPIV, cf. Willert and Gharib, 1991) at piston stroke length-to-diameter ratios of 4 and 12. The deviation from experimental data at later times for the stroke ratio of 12 is due to breakdown of the assumption that the boundary layer thickness is negligible relative to the curvature of the cylinder. This assumption was necessary for development of the analytical model, but neglects the accelerated growth of the boundary layer (and concomitant increase in exit fluid velocity) due to the cylinder curvature. Indeed, an accelerated increase in vorticity flux at longer stoke lengths is

apparent in the change of slope beyond stroke length-to-diameter ratio 8.5 (i.e., time $T > 3.8$ s) in figure 5.1(b).

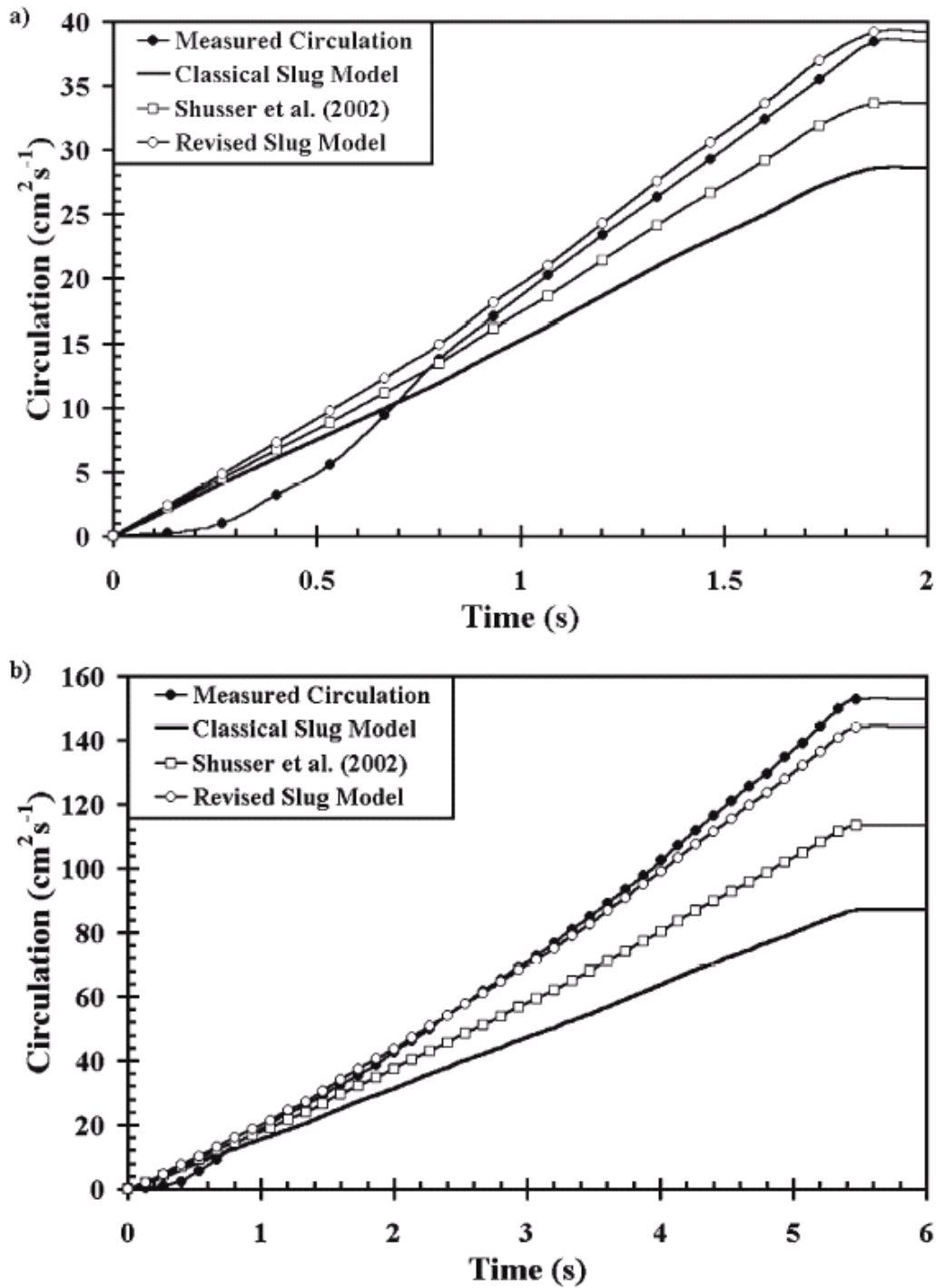


Figure 5.1 Comparison of slug models of vorticity flux with DPIV measurements. (a) $L/D = 4$; (b) $L/D = 12$.

The revised correction additionally affects the predicted non-dimensional Norbury (1973) vortex core thickness ε of fully-formed vortex rings after pinch-off (Gharib et al., 1998). Specifically, the revised correction shifts the curves in figure 10 of Shusser et al. (2002) upward, so that the core thickness consistent with the vortex ring formation number is reduced by 25 percent, to 0.3. This is in agreement with the experimental results of Gharib et al. (1998).

5.3 Conclusions

An important correction to the slug model boundary layer correction proposed by Shusser et al. (2002) has been discovered. The new result significantly improves agreement with experimental measurements of starting jet vorticity flux and vortex ring core thickness. The observed overestimation of vorticity flux by the revised correction at early times is related to the dynamics of flow initiation, during which nozzle exit overpressure has been observed to play an important role (Krueger and Gharib 2003). Nonetheless the current result demonstrates the significant effect of boundary layer growth, especially for the longer piston strokes needed to generate thick vortex rings.

5.4 Chapter References

- Gharib, M., Rambod, E. and Shariff, K. 1998 A universal time scale for vortex ring formation. *J. Fluid Mech.* **360**, 121-140.
- Krueger, P. S. and Gharib, M. 2003 The significance of vortex ring formation to the impulse and thrust of a starting jet. *Phys. Fluids* **15**, 1271-1281.
- Norbury, J. 1973 A family of steady vortex rings. *J. Fluid Mech.* **57**, 417-431.
- Rosenhead, L. 1963 *Laminar Boundary Layers*. Clarendon Press.

- Shariff, K. and Leonard, A. 1992 Vortex rings. *Annu. Rev. Fluid Mech.* **24**, 235-279.
- Shusser, M., Gharib, M., Rosenfeld, M. and Mohseni, K. 2002 On the effect of pipe boundary layer growth on the formation of a laminar vortex ring generated by a piston/cylinder arrangement. *Theor. Comp. Fluid Dyn.* **15**, 303-316.
- Willert, C. E. and Gharib, M. 1991 Digital particle image velocimetry. *Exp. Fluids* **10**, 181-193.

CHAPTER 6: Starting flow through nozzles with temporally variable exit diameter

Submitted to Journal of Fluid Mechanics December 8, 2004

6.0 Chapter Abstract

Starting flow through a nozzle or orifice typically results in the transient formation of a leading vortex ring and trailing jet. Experiments are conducted to investigate the dynamics of this process in the case of a temporally variable nozzle exit diameter, with the aim of understanding these flows as they occur in Nature and emerging technologies. By kinematically decoupling the source flow from the nozzle motion, comparison across several classes of exit diameter temporal variation is facilitated. Kinematic models of the starting flows are used to accurately predict the fluid circulation produced by the vortex generators and to emphasize the special role of the nozzle boundary layer in dictating the nature of the global flow patterns. A dimensionless temporal parameter is derived in order to track the vortex formation process for the various classes of nozzle motion. Dynamics of vortex ring disconnection from the source flow are studied in this new dimensionless framework. We show that temporally increasing the nozzle exit diameter as the starting flow develops results in higher-energy vortex ring structures with peak vorticity located further from the axis of symmetry relative to a static nozzle case. In addition, the normalized energy supplied by the vortex generator is increased in this process. We do not observe a delay in the onset of vortex ring disconnection from the trailing jet, as predicted by previous numerical simulations. In contrast, growth of the leading vortex ring is substantially augmented by temporally decreasing the nozzle exit diameter during fluid

ejection, as noted in a previous experiment. Normalized vortex ring circulation is increased 35% in these cases, and the normalized energy of the generated vortex rings is equivalent to that of Hill's spherical vortex. These observed effects are explained by considering the measured vorticity distribution and energy of the starting flows. Strategies are suggested to exploit the discovered dynamics for various pulsed-jet applications.

6.1 Introduction

Pulsatile flows are among the most common and successful mechanisms for convective fluid transport found in Nature. Although the selection of such techniques may often be related to morphological constraints (Vogel, 1988, 1994), it remains noteworthy that today we can observe the action of these unsteady flows in systems ranging from the most primitive jellyfish locomotor to the complex trans-mitral and trans-aortic blood flows in the animal heart.

Throughout the diverse catalogue of biological systems utilizing pulsatile flow, the generated starting flow typically emerges from a nozzle or orifice with temporally variable exit diameter. In systems with valve structures governing the flow, the observed motion of the exit diameter is a necessary consequence of the transition from a closed valve to an open one, and vice versa. An important example is the animal heart, where it has been suggested that the interaction between the starting flows and the moving valves can be correlated to some commonly observed cardiac pathologies (e.g., Gorman et al., 1996; Yoganathan, Lemmon and Ellis, 2000; Handke et al., 2003).

In addition to the aforementioned use of starting flows for mass transfer, many biological systems have co-opted pulsatile flow for locomotion. Certain cnidarians (e.g., jellyfish), cephalopods (e.g., squid), and bivalves (e.g., scallops) are most prominent in this

regard. Dabiri and Gharib (2003) measured exit diameter changes up to 30% during steady swimming of *Chrysaora fuscescens* jellyfish. Transient exit diameter changes of over 400% have been measured in the *Lolliguncula brevis* squid (Bartol, Patterson and Mann, 2001), and the nozzle exit has been observed to close completely between fluid pulses in the *Loligo pealei* squid (Anderson and DeMont, 2000). In many instances, the temporal variation of the exit diameter is actively controlled, suggesting possible real-time refinement of the fluid-structure interaction.

The fluid dynamical effect of a temporally variable nozzle exit diameter on a starting flow has remained essentially unexplored. Our mandate for this study is at least twofold. First, a better understanding of these systems can facilitate predictive models to explain correlations between local fluid-structure interactions at the nozzle or orifice exit and observed global features of the generated flow. Secondly, we may explain the physical impetus for the specific programs of exit diameter temporal variation observed in Nature. The design principles that are elucidated here may be transferable to emerging engineering technologies, such as pulsed-jet propulsors and synthetic jets (see Glezer and Amitay, 2002 for a review).

From a kinematic perspective, the primary constituents of the starting flow through a nozzle or orifice are a leading vortex ring and, in some cases, a trailing jet. A large literature dealing with the dynamics of the quasi-steady jet is now available; however, our understanding of the dynamics of the leading vortex ring is more limited. Gharib, Rambod and Shariff (1998) experimentally identified a transition from formation of a single vortex ring to generation of a leading vortex ring and trailing flow, as a function of the normalized length of the ejected slug of fluid. Their work and subsequent models by Mohseni and

Gharib (1998), Linden and Turner (2001), and Mohseni (2001) have pointed to the effect of an energetic requirement for the leading vortex ring during this transition, as stipulated by the Kelvin-Benjamin variational principle (Kelvin, 1875; Benjamin, 1976). The principle suggests that the leading vortex ring is incapable of further growth via ingestion of fluid from the vortex generator if the energy of this source flow falls below the vortex ring energy. Dynamical separation of the leading vortex ring from the trailing flow due to this energetic effect is referred to as *pinch-off* in the literature.

Krueger (2001) and Krueger and Gharib (2003) attained the first measurements of the dynamical effect of the vortex ring pinch-off process. They discovered that the time-averaged force generated by a starting flow becomes maximal at the onset of vortex ring pinch-off. This result suggests an optimal operating point just before vortex ring pinch-off and also motivates the search for methods to delay vortex ring pinch-off altogether. Dabiri and Gharib (2004a) successfully demonstrated the possibility of delaying vortex ring pinch-off by imposing an external axisymmetric counter-flow during vortex ring formation. Although those experiments demonstrated the feasibility of delaying vortex ring pinch-off in general, it would be more useful to achieve similar results by manipulating properties of the vortex ring generator itself, i.e., in the absence of external intervention.

Numerical studies by Rosenfeld, Rambod and Gharib (1998); Zhao, Frankel and Mongean (2000); and Mohseni, Ran and Colonius (2001) have demonstrated that parameters such as shear layer thickness, Reynolds number, and velocity profile can all affect the dynamics of the pinch-off process. As this parameter space has only been explored *in silico*, it is not immediately evident how each of these parameters should be manipulated in practice. Notwithstanding, two practical methods have emerged from the

simulations of Mohseni et al. (2001) as potential candidates to delay pinch-off of the leading vortex ring. In the first case, it is suggested to increase the velocity of the source flow from the vortex generator to prolong feeding of dynamical invariants (i.e., energy, impulse, and circulation) to the leading vortex ring. This concept is also proposed by Shusser and Gharib (2000) as a corollary to their theory that vortex ring pinch-off occurs when the velocity of the trailing jet (source flow) falls below the celerity of the leading vortex ring.

The second method suggested by Mohseni et al. (2001) is to increase the radial extent of the forcing (i.e., increase the nozzle or orifice exit diameter) as the starting flow emerges from the vortex generator. In this way the shear layer of the source flow behind the leading vortex ring could be moved away from the axis of symmetry, where it would normally cancel with its mirror across the azimuthal plane of symmetry and lose strength.

These and other potential methods for pinch-off delay have not yet been validated experimentally. Dr. J. J. Allen of New Mexico State University (2003, personal communication) has conducted experiments on vortex ring formation with a variable diameter orifice aperture. Consistent with the prediction of Mohseni et al. (2001), preliminary results indicated the effectiveness of an accelerating source flow for generating vortex rings of low normalized energy, possibly indicative of delayed vortex ring pinch-off. In contrast, increasing the radial extent of the forcing via a temporally increasing orifice aperture did little to enhance the vortex ring formation process. Several questions remain unanswered regarding the experimental method of Allen (2003), including the effects of fluid structures generated on the upstream-facing side of the orifice plate (e.g., in stagnation zones); aperture rotation about the axis of symmetry during orifice enlargement; and noncircular

aperture shape. Hence, we will only refer to those experiments in regard to the general qualitative trends observed.

The objective of the present experiments is to study the dynamics of starting flows through nozzles with temporally variable exit diameter. The nearly axisymmetric nozzle used in these experiments serves as a generalization of the various nozzle and orifice geometries observed in biological systems. Nozzle dynamics are decoupled from the source flow by imposing a constant volume flux from a piston-cylinder apparatus at the inlet to the nozzle during all experiments. This strategy proves to simplify the analysis and facilitate quantitative comparison across all of the test cases. An important goal of these experiments is to implement the strategies for pinch-off delay suggested by Mohseni et al. (2001) and examined by Allen (2003). The observed starting flow dynamics are explained in terms of the shear layer kinematics and leading vortex ring vorticity distribution and energy. In addition, we examine relevant measures of pulsing performance to suggest benefits of temporally variable nozzle and orifice exit diameters in biological systems and emerging technologies.

The following section describes the apparatus and experimental methods in detail, with special attention given to possible artifacts that could be introduced to the observed fluid dynamics by the nature of the nozzle design. The results are catalogued in Section 3, beginning with the kinematics of the nozzle boundary layer and shear layer efflux, and subsequently focusing on the dynamics of the leading vortex ring. Nuances of dimensional analysis for the time-dependent exit diameter are also presented in this section. Section 4 summarizes the analyses, provides comparison with previous numerical and experimental

observations of these flows, and discusses the physical basis for effective use of temporally varying exit diameters in practice.

6.2 Apparatus and Experimental Methods

6.2.1 Apparatus design

Several challenges were faced in designing an apparatus to achieve temporal variation of a nozzle exit diameter, without introducing undue complexity or unwanted artifacts into the experiments. The design requirements included—but were not limited to—distinct and repeatable separation of the nozzle boundary layer at a known radial distance from the axis of symmetry and at a fixed axial location; a nozzle wall that is sufficiently rigid to prevent deformation due to fluid forces, yet flexible enough to vary the exit diameter over a large range; uniform radial actuation to maintain a nearly circular shape at the nozzle exit plane; suppression of secondary vorticity generation by the apparatus (e.g., as is present on the upstream-facing side of an orifice plate); and an actuation mechanism that does not measurably disturb the flow.

This set of requirements is appropriately satisfied by the apparatus represented in figure 6.1. The source flow is generated by a traditional piston-cylinder apparatus (cf. Dabiri and Gharib, 2004c), with the inlet flow originating from the left hand side of the hollow cylinder (inner diameter = 2.5 cm) in the schematic. A piston is oriented coaxially with the hollow cylinder and has its diameter D_p flush with the inner surface of the cylinder. The piston is driven by flow supplied from an external constant-head tank operating at a total pressure head Δp of 8.2 kPa. A computer-controlled solenoid valve meters the flow using an impulsive velocity profile with a rise time of approximately 300

ms to steady flow at $8.8 \text{ cm}^3\text{s}^{-1}$. Flow rates are monitored by an ultrasonic flow probe at the inlet to the cylinder and are recorded to a computer hard disk via a LabVIEW program. A single value of the constant volume flux is used throughout all of the experiments described in this paper. In this way, the source flow merely serves as a control parameter and falls out of much of the subsequent analyses. Source flow from the piston-cylinder apparatus enters the nozzle inlet, which is mounted immediately downstream.

The nozzle is constructed from a 5.1 cm length of originally straight latex rubber tubing with 1.5 cm nominal inner diameter, 0.08 cm nominal thickness, and sharp edges. Optimal wall thickness was determined from repeated iterations of the design to facilitate maximum actuation of the exit diameter without becoming susceptible to deformation due to fluid forces. The nozzle inlet diameter is matched to the inner diameter of the upstream hollow cylinder by fitting the elastic tube over the outer diameter of the cylinder lip ($D_o = 3.1 \text{ cm}$). To facilitate a smooth transition from the cylinder to the nozzle, the cylinder lip is sharpened to form a 7 degree wedge from its outer diameter to inner diameter (cf. figure 1 of Dabiri and Gharib, 2004c). The nozzle is held to the cylinder by elastic forces induced during the process of stretching the latex tube over the cylinder lip, and by a series of compression clamps placed around the cylinder outer diameter.

For simplicity in later analyses, a spatially linear contraction in nozzle diameter from the inlet to the exit plane is desired. This is accomplished by supporting the elastic nozzle with 16 straight stainless steel cotter pin support spars equally spaced azimuthally around the nozzle. Each support spar has a hairpin shape and is fitted over the downstream edge of the elastic nozzle with both prongs extending upstream along the length of the nozzle. The junction of the two prongs of each hairpin is positioned at the nozzle exit plane.

The free ends of the two prongs of each hairpin are fixed to the inner and outer surfaces of the nozzle, respectively, using a waterproof adhesive. These free hairpin ends effectively act as a pin joint when the nozzle is actuated.

A water-resistant actuating cable is connected to the hairpin junction of each support spar at the nozzle exit plane; the cable extends radially to a perforated conical shell that acts as a fixed pulley. The apex of the cone is truncated, and the piston-cylinder apparatus is mounted rigidly through the apical opening. After passing through a hole in the wall of the conical fixed pulley, the cable is turned 90 degrees toward an axial orientation upstream, where its terminal end is mounted to the inner surface of a hollow drum. The drum is mounted coaxially to the piston-cylinder apparatus on a roller bearing, so that it is free to rotate about the axis of symmetry.

When the drum rotates, the terminal end of the cable that is mounted to the drum moves azimuthally. Since the cable is inextensible, the other end of the cable connected to the support spar is pulled radially toward its respective hole in the conical pulley. By this mechanism, a single degree of freedom in the rotating drum is transduced to radial actuation at 16 uniformly spaced locations around the azimuth of the nozzle exit plane.

A flat belt pulley system connects the drum to a computer-controlled stepper motor that governs the nozzle motion. The drum rotation necessary for actuation of the nozzle from minimum to maximum diameter is approximately 30 degrees. Details of the specific programs of exit diameter variation used in these experiments will be presented in a subsequent section.

The entire piston-cylinder-nozzle apparatus is submerged in a 60 cm H \times 40 cm W \times 100 cm L water tank with transparent walls. Mounting points are located along the cylinder and around the azimuth of the conical pulley.

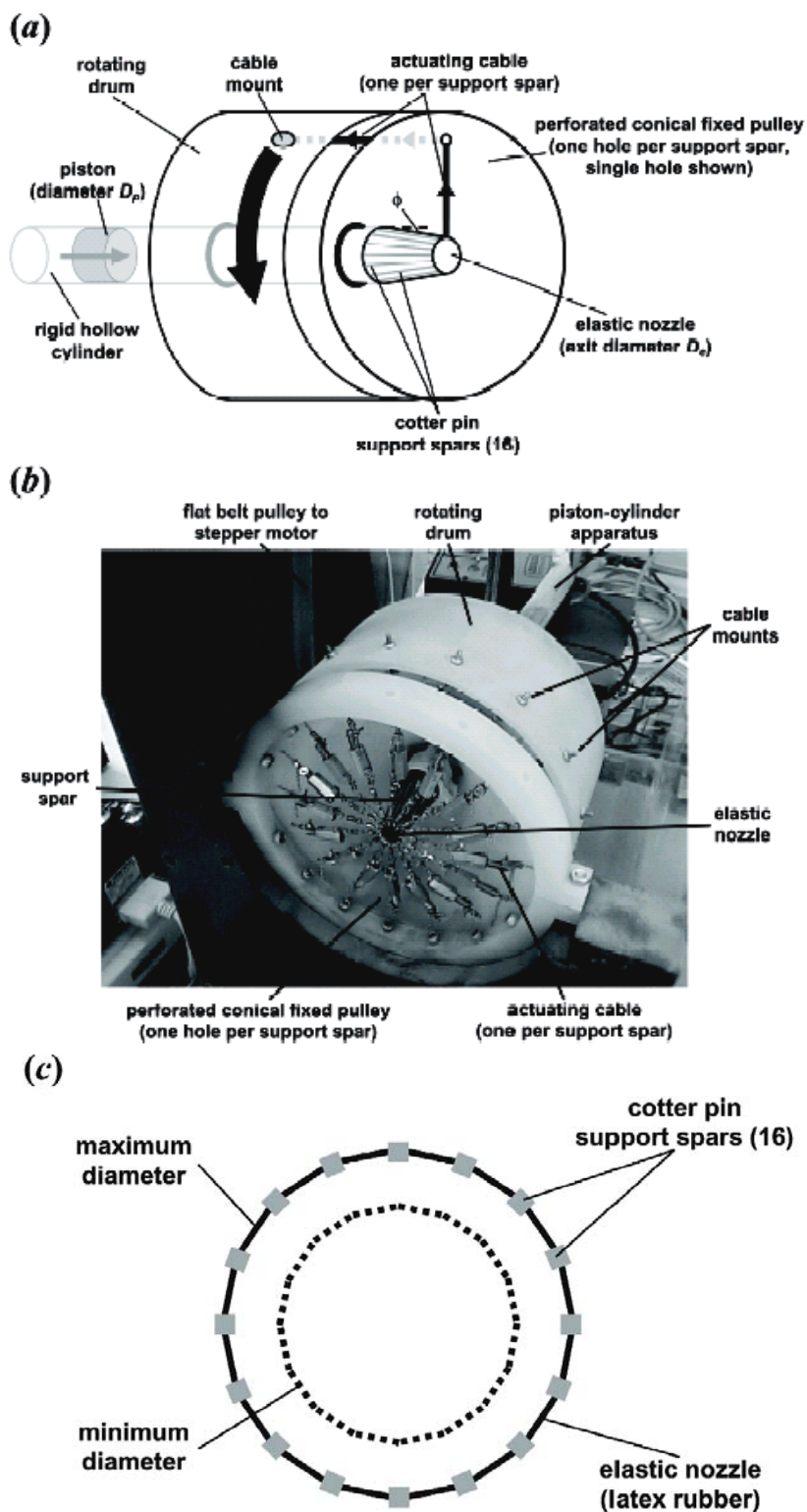


Figure 6.1 Apparatus for temporal variation of nozzle exit diameter. (a) schematic. (b) laboratory image. (c) front view of nozzle exit plane.

6.2.2 *Effects of noncircular nozzle shape*

Although most of the design requirements are satisfied *ipso facto* the apparatus described above, an important concern must be directly addressed regarding the shape of the nozzle exit. Figure 6.1(c) shows the front view of the nozzle at the exit plane, in proportions that are approximately to scale. The cotter pin support spars, with dimensions of 0.13 cm azimuthally and 0.08 cm per prong radially, act as a finite amplitude disturbance with wavenumber 16 on the starting flow. It is reasonable to question the behavior of this disturbance in time, especially as it relates to the forming leading vortex ring.

The stability theory for an exact representation of this flow is unresolved and also beyond the scope of this paper. However, we can appeal to the classical inviscid theory and make use of qualitative experiments to develop a convincing argument for the negligible effect of the nozzle shape perturbations on the flow.

Azimuthal wave development on vortex rings has been appreciated for decades, beginning with the experimental work of Krutzsch (1939). The physics of the phenomenon were elucidated by Widnall, Bliss, and Tsai (1974) and further refined by Widnall and Tsai (1977), Saffman (1978), and Shariff, Verzicco, and Orlandi (1994). The work of Saffman (1978) is especially useful in the present context, as it examines the dependence of the most unstable wavenumber on the Reynolds number (based on ring celerity and nozzle exit diameter) and diameter-normalized length of the ejected slug of fluid T^* . Combining equations (4.4) and (4.6) of his paper leads to a relationship between the most unstable wavenumber, the critical Reynolds number, and the parameter T^* . The equations predict that the growth of azimuthal disturbances of large wavenumber is suppressed at low Reynolds numbers. For the normalized fluid slug length in the vortex rings studied here (T^*

≤ 8), the Reynolds number corresponding to an unstable wavenumber 16 (i.e., $Re \approx 6 \times 10^4$) is approximately two orders of magnitude higher than the conditions of the present experiments.

We are quick to note that this is a simplified calculation. To further support the above conclusion, we conducted dye visualization experiments of the starting jet formed by the apparatus at the minimum and maximum nozzle exit diameter. In both cases the vortex ring remained laminar and did not retain visible signs of the shape perturbation at the nozzle exit (at wavenumber 16 or otherwise) throughout observation of the rings until the dye began to dissipate far downstream. Especially in light of the fact that our observations will focus on the near-field flow, we proceed under the assumption that the measured dynamics do not represent artifacts from non-idealities in the experimental apparatus. The nozzle exit diameter in each case is defined based on an equivalent circle with cross-sectional area equal to the measured nozzle exit area.

6.2.3 *Quantitative flow visualization*

Kinematics of the flow field are measured using digital particle image velocimetry (DPIV, cf. Willert and Gharib, 1991; Adrian, 1991). The hardware and parameters of the technique are essentially the same as described in Dabiri and Gharib (2004c). A laser sheet from a Nd:YAG laser source illuminates a plane of symmetry relative to the vortex generator, providing an azimuthal view of the axisymmetric starting flow from an orthogonally oriented digital CCD camera at 30 Hz. In the present experiments the flow field measures 7.8 cm ($3.1 D_p$) radially from the axis of symmetry and from 0.77 cm ($0.3 D_p$) to 15.8 cm ($6.2 D_p$) downstream. The field is imaged at a resolution of approximately 65 pixels per cm, sufficient to resolve the vorticity distribution in the vortex ring core.

Timing of source flow initiation, nozzle actuation, laser firing, and image capture is coordinated by an in-house code and LabVIEW data acquisition hardware. Velocity and vorticity measurements possess an uncertainty of 1 percent and 3 percent, respectively.

6.2.4 *Experimental parameter space*

The extreme positions of the nozzle exit diameter are plotted to approximate scale in figure 6.1(c). The maximum nozzle exit area is nearly 200 percent of the minimum exit area. These positions are the end points of the temporal exit diameter variation in each of the experiments conducted. Figure 6.2 plots the specific programs of nozzle exit diameter variation studied in these experiments. The diameter profiles were measured from frontal view video recordings of the nozzle undergoing each actuation program. The measured diameter at each instant is an effective value computed as $D_e = 2(A_e/\pi)^{1/2}$, where A_e is the nozzle exit area. This method accounts for the reduced nozzle exit area due to the presence of cotter pin support spars at the exit plane (figure 6.1c) and is the source of the lower minimum exit diameter (i.e., $D_e = 1.21$ cm) relative to the nominal pre-installation tube diameter (i.e., $D_e = 1.5$ cm). Static nozzle cases at minimum ($D_e = 1.21$ cm = $0.48 D_p$; henceforth SMIN) and maximum ($D_e = 1.69$ cm = $0.67 D_p$; henceforth SMAX) diameter are included as control sets. The dynamic nozzle cases consist of a slower-opening (SO) case, a faster-opening (FO) case, a slower-closing (SC) case, and a faster-closing (FC) case.

The time derivative of the nozzle exit diameter change is shown in figure 6.3. These plots indicate that the peak temporal variation in the faster cases is double that of the slower cases. The slight modulation in nozzle exit diameter rate of change for the SO and FO cases (at time $t = 1.2$ s and 0.6 s, respectively) occurred due to artifacts related to elastic

deformation of the nozzle by the support spars, but did not measurably affect the observed vortex dynamics. Dynamic nozzle programs are repeatable to within 3%.

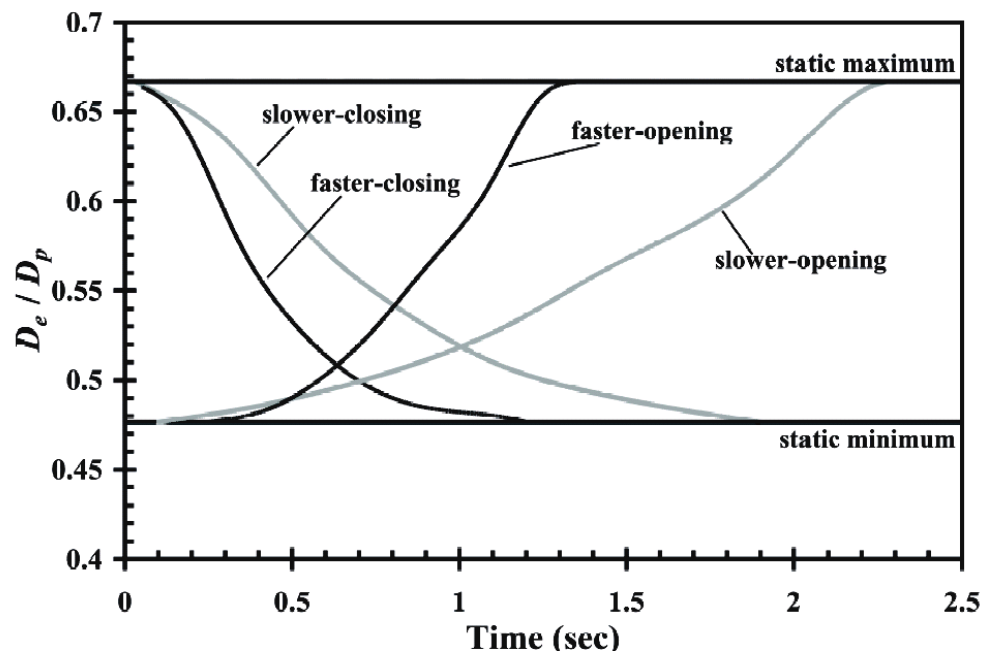


Figure 6.2 Programs of nozzle exit diameter temporal variation.

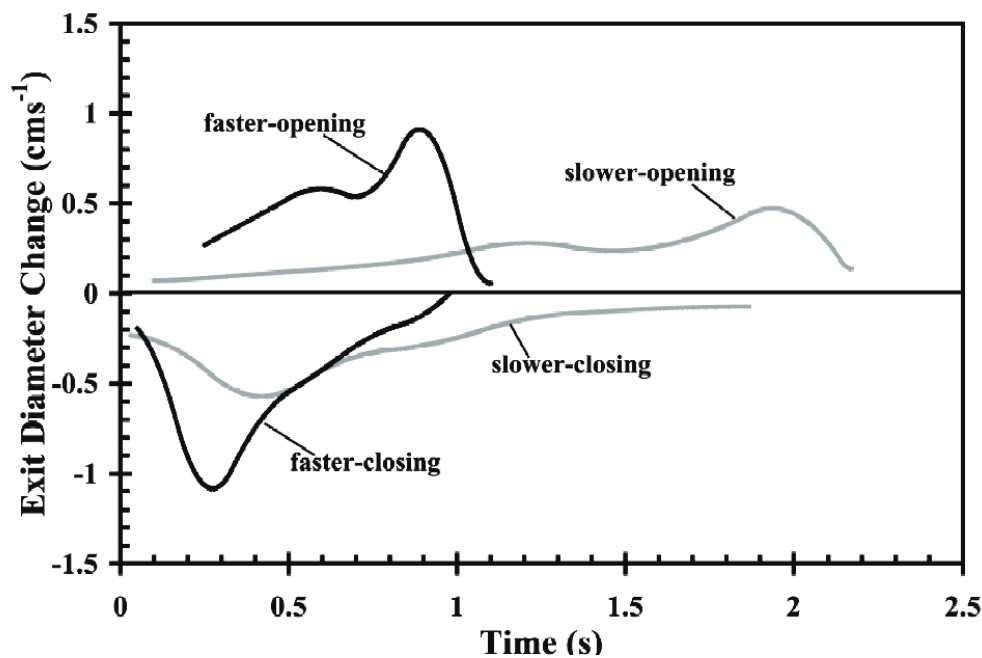


Figure 6.3 Rate of diameter change for each program of nozzle exit diameter temporal variation.

Nozzle contraction angle ϕ varies between 12 degrees when the exit diameter is in its maximum position, and 18 degrees when in its minimum position.

The Reynolds numbers at which these experiments were conducted range between 660 and 920 based on the nozzle exit velocity and diameter, and between 1500 and 3500 based on the circulation of the leading vortex ring. These Reynolds numbers are consistent with several of the biological systems discussed in the Introduction, such as jellyfish (Daniel, 1983; Dabiri and Gharib, 2003) and juvenile squid (Bartol et al., 2001), but are below the range of some higher-speed jetters such as adult squid (Anderson and DeMont, 2000). Given that Gharib et al. (1998) have demonstrated the process of vortex ring formation in starting jets to be robust up to at least a Reynolds number of 6000 (based on the circulation of the leading vortex ring), the present results should be applicable to many of the higher-speed flows as well.

Measurement results are presented herein typically using single representative data sets for each nozzle program (figure 6.6 is a notable exception). Three or more iterations were conducted for each program of nozzle exit diameter temporal variation to ensure that stated values accurately represent each test case. The maximum uncertainty in each representative data set is $\pm 5\%$.

6.2.5 Boundary layer dynamics

Didden (1979) clearly demonstrated the special role of boundary layer dynamics in the development of starting flows, especially in relation to leading vortex ring formation. Using laser Doppler velocimetry (LDV) measurements, he observed quantitatively how the motion of the boundary layer at flow initiation dominates the roll-up of the leading vortex ring. In addition, boundary layer growth within the hollow cylinder of the vortex generator

was shown to lead to an increase in vorticity flux into the starting jet. These interesting aspects of starting flows cannot be captured by a simplified slug model of the flow, which neglects boundary layer effects altogether (cf. Shariff and Leonard, 1992; Krueger and Gharib, 2003).

Shusser et al. (2002) suggested incorporating a Rayleigh-Stokes solution to account for boundary layer growth within the hollow cylinder of a piston-cylinder vortex generator. A modified version of their solution, presented by Dabiri and Gharib (2004b), achieved close agreement with DPIV measurements of the generated vorticity flux.

In the present apparatus, we must address the added complexity of a spatially and temporally accelerating mean flow due to the presence of a nozzle with temporally variable contraction ratio D_p/D_e downstream of the piston-cylinder apparatus. The effect of this unsteady flow on the boundary layer that formed upstream in the piston-cylinder apparatus will largely dictate the nature of the starting flow that emerges from the nozzle exit.

A quasi-steady analysis predicts that the boundary layer entering the nozzle from the piston-cylinder apparatus will become thinner due to the nozzle contraction, perhaps eliminating the need for the correction of Dabiri and Gharib (2004b) to the starting flow. However, the combination of spatial and temporal accelerations in the real starting flow adds complexity that cannot be easily captured by a quasi-steady analysis.

Our piston-cylinder flow rate data and nozzle exit velocity profile measurements obtained using DPIV are sufficient to determine the level of boundary layer thinning achieved in each of the experiments performed here. This information will be critical for properly modeling these starting flows, especially in predicting the vorticity flux from the nozzle in each experiment.

Measurements of the exit velocity profile for each temporal pattern of nozzle diameter variation indicate that those cases with larger average nozzle contraction ratio during initiation of the starting jet (i.e., SMIN, SO, and FO cases) exhibit significantly less boundary layer thinning than those with smaller average nozzle contraction ratio over the same period of time (i.e., SMAX, SC, and FC cases). Figure 6.4 exemplifies these trends for the SMIN and SMAX diameter cases. Initially the boundary layer dynamics are similar in the two cases (figure 6.4*a*). However, at later times the larger nozzle contraction ratio in the SMIN case causes boundary layer vorticity from the upstream piston-cylinder apparatus to be convected downstream out of the nozzle faster than it is rearranged by diffusion, allowing the upstream velocity profile (i.e., at the nozzle entrance) to pass through the nozzle essentially unchanged. Thus, the velocity profile in the SMIN case does not exhibit thinning similar to that expected in a quasi-steady flow. By contrast, the SMAX case has a smaller nozzle contraction ratio and therefore a lower spatial acceleration in the nozzle. Accordingly, upstream vorticity from the piston-cylinder apparatus persists in the nozzle for a longer duration, allowing viscous diffusion to rearrange the boundary layer. In these cases boundary layer thinning is more substantial (figure 6.4*b*).

The observed dynamics of the boundary layers in these starting flows are a consequence of the specific experimental apparatus implemented for vortex generation. There exist various methods to mitigate the effect of the boundary layer so that it does not play such a large role in the fluid dynamics (e.g., Joslin, 1998). Our strategy is to embrace the nonessential boundary layer effects in order to better understand these starting flows in general, and to better relate to biological systems, most of which appear to lack immediate methods for boundary layer elimination.

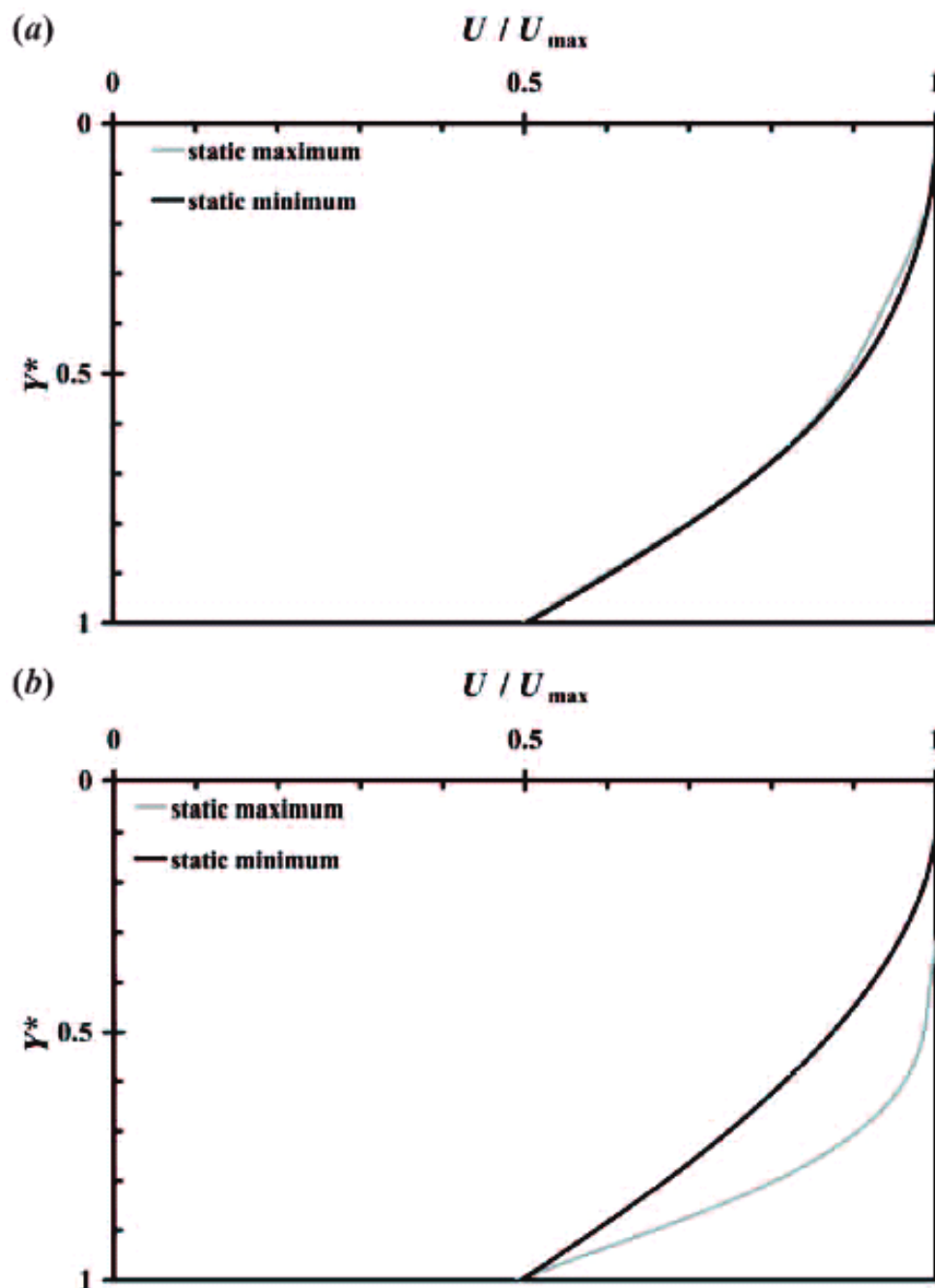


Figure 6.4 Velocity profile of fluid efflux at $X = 0.3 D_p$ for static minimum and maximum diameter cases. (a) $T = 0.67$ s. (b) $T = 2.0$ s. Y^* is the radial coordinate normalized by the location at which $U/U_{max} = 0.5$.

In the following sections we will model the starting flow for the SMAX, SC, and FC nozzles as if the piston-cylinder boundary layer has completely thinned in the nozzle, while modeling the SMIN, SO, and FO cases as if the piston-cylinder boundary layer has passed through the nozzle unchanged. We do recognize that boundary layer thinning will occur to some degree in every test case. However we will show that this approximation is sufficient to generate a realistic picture of the starting flows in these experiments.

6.3 Results

6.3.1 Vorticity flux

The flux of vorticity from the starting flow boundary layer provides a useful measure of the dynamical contribution of the vortex generator to the ambient fluid. Measuring the flux of vorticity in practice typically requires a precise velocimeter, a prospect that is often inconvenient when studying biological systems or engineering technologies with auxiliary components that interfere with controlled experimental observations. It is therefore desirable to develop analytical models to accurately predict the vorticity flux from starting flows, based on known parameters of the vortex generator. Naturally, our focus is directed toward starting flows through temporally variable nozzles.

In the case of a piston-cylinder apparatus, the classical slug model result for the vorticity flux is

$$\left. \frac{d\Gamma}{dt}(t) \right|_{\text{slug}} \approx \frac{1}{2} U_p^2(t), \quad (6.3.1)$$

where Γ is the circulation delivered by the vortex generator, and U_p is the (possibly time-dependent) piston speed.

By replacing the piston velocity with the fluid volume flux $\dot{\Omega}$ and the circular nozzle or orifice exit diameter D_e , we arrive at a generalized vorticity flux model for an arbitrary source flow with circular nozzle or orifice exit:

$$\left. \frac{d\Gamma}{dt}(t) \right|_{\text{slug}} \approx \frac{8\dot{\Omega}^2(t)}{\pi^2 D_e^4(t)}. \quad (6.3.2)$$

Boundary layer growth inside the vortex generator results in a decreased flow velocity near the walls and concomitant increase in velocity outside the boundary layer in order to satisfy continuity. As mentioned in the previous section, only a simplified model of this process is tractable in the present context. Using the result of Dabiri and Gharib (2004b), the vorticity flux in this case is predicted by

$$\left. \frac{d\Gamma}{dt}(t) \right|_{\text{BLG}} \approx \frac{8\dot{\Omega}^2(t)}{\pi^2 D_e^4(t)} \left[1 + \frac{8(\nu t)^{1/2}}{\pi^{1/2} D_e(t)} \right]^2. \quad (6.3.3)$$

According to the conclusions of the preceding section, (6.3.2) was used to predict the vorticity flux in the SMAX, SC, and FC cases, while (6.3.3) was applied to the SMIN, SO, and FC cases. The results are plotted in figure 6.5. After initial vortex ring roll-up, the agreement is very good in each case, especially considering that no empirical scaling factors have been used. Discrepancies shortly after flow initiation at time $T = 0$ are due to difficulties in measuring the flow field close to the nozzle exit, and due to vortex ring roll-up and overpressure effects previously documented by Didden (1979) and Krueger (2001), which cannot be captured by these models. The former issue, which causes an uncertainty in the measured time of flow initiation, will be revisited in the following section. Notably, the global flow—represented by the total generated circulation—is accurately predicted by the models.

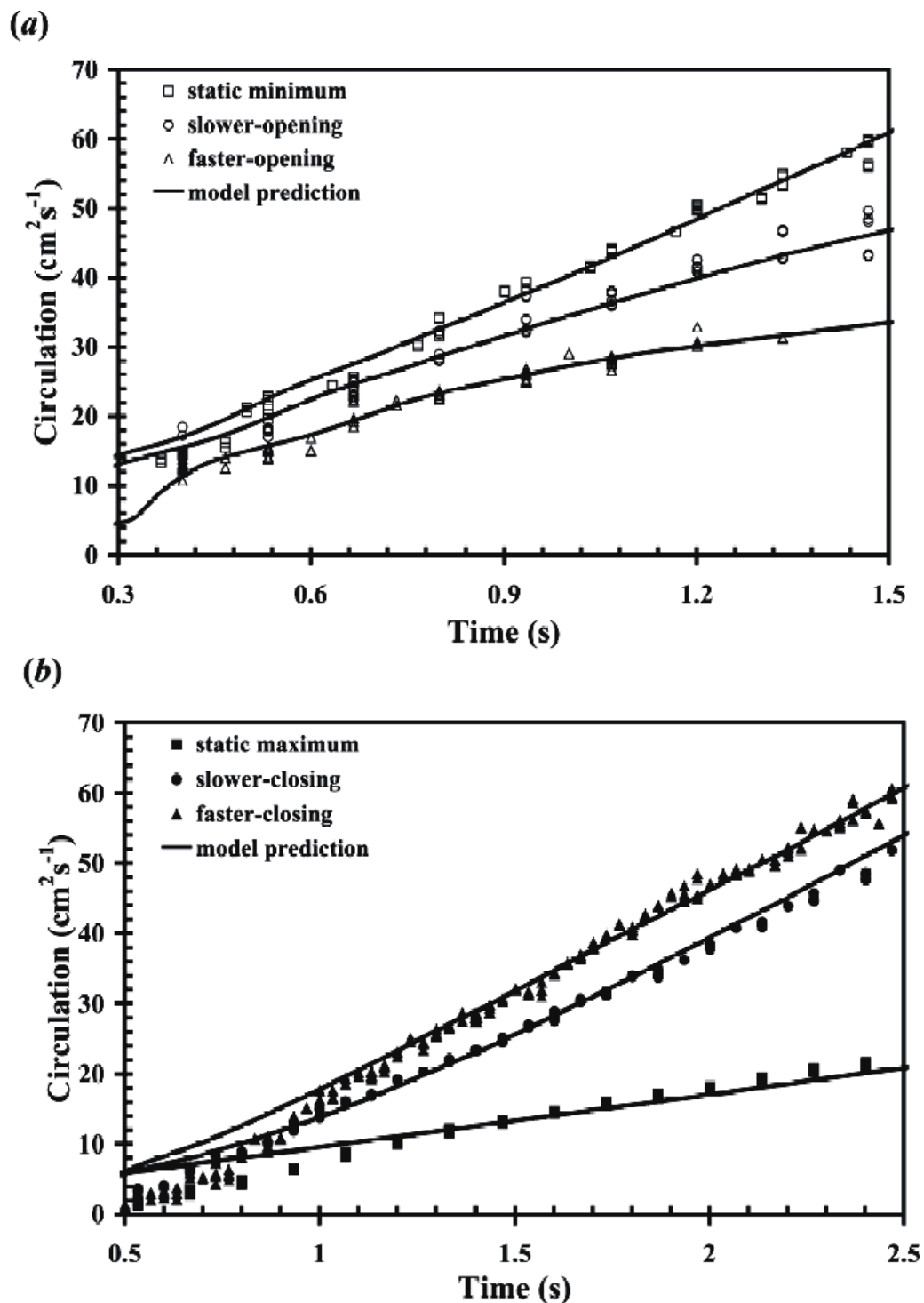


Figure 6.5 Measured and predicted circulation generated for each program of nozzle exit diameter temporal variation. (a) SMIN, SO, and FO cases. (b) SMAX, SC, and FC cases.

6.3.2 Dimensional analysis

In preparation for the ensuing discourse on leading vortex ring dynamics, it is useful to prepare a dimensionless framework in which to present the results. Gharib et al. (1998) define a vortex ring formation time corresponding to the dimensionless length of the fluid slug ejected from a piston-cylinder apparatus:

$$T_{\text{GRS}}^* \equiv \frac{\overline{U_p} t}{D_p}, \quad (6.3.4)$$

where the overbar denotes a running time average. Mohseni et al. (2001) use a modified form of this definition, in which the piston speed is replaced by the vortex ring celerity.

The difficulty with these definitions in a general starting flow is that the former is valid strictly for a constant-diameter vortex generator, and the latter requires knowledge of the motion of the leading vortex ring, which may be inaccessible or even irrelevant to the particular flow of interest.

A generalized dynamic dimensionless time scale based on the parameters of the vortex generator can be derived by considering an infinitesimal increment in the formation time of Gharib et al. (1998):

$$dT^* = \frac{U_e(t)}{D_e(t)} dt. \quad (6.3.5)$$

In (6.3.5), the nozzle exit velocity U_e (i.e., the free-stream flow velocity outside the boundary layer as in Dabiri and Gharib 2004b) is used as the appropriate characteristic velocity instead of the piston speed. Integrating over the duration of fluid ejection, we arrive at a dimensionless time scale that properly accounts for temporal changes in the exit diameter:

$$T^* = \int_0^t \frac{U_e(\tau)}{D_e(\tau)} d\tau = \overline{\left(\frac{U_e}{D_e} \right)} t. \quad (5.3.6)$$

This new dimensionless parameter is monotonically increasing for any temporal variation of the exit diameter, as it must be to accurately reflect the irreversible nature of the fluid ejection process. In contrast, definition (5.3.4) of Gharib et al. (1998) gives a spurious result of decreasing formation time when the instantaneous or time-averaged exit diameter is increasing.

Consistent with the preceding result, the circulation is properly normalized using the terms $\overline{(U_e/D_e)}$ and $\overline{U_e^2}$ as

$$\Gamma^* = \frac{\Gamma \overline{(U_e/D_e)}}{\overline{U_e^2}}. \quad (5.3.7)$$

Despite the inclusion of a boundary layer correction to the exit velocity in the SMIN, SO, and FO cases, a plot of normalized circulation versus formation time should still possess a slope of 1/2 in accord with the slug model equation (6.3.1). The slope is preserved because the boundary layer correction appears in both the circulation and time normalizations, leaving their ratio unaffected. Figure 6.6 shows the circulation trends from several iterations of each nozzle case. The data are shifted along the abscissa so that the linear portion of each trend has its intercept at the origin. After initial scatter, all of the data collapses to the reference line with slope equal to 1/2.

Data scatter at early formation time is largely due to differences in the manner in which the leading vortex ring enters the DPIV measurement window from the upstream boundary at $X = 0.3D_p$. The trend of increasing measured circulation during this time is dominated by propagation of the vortex ring core vorticity into the measurement window at

the upstream boundary. Hence, the measured data trends at early formation time are not necessarily indicative of the actual rate of vorticity generation by the starting flow. This effect has been previously observed by Didden (1979) using LDV measurements and Dabiri and Gharib (2004b) using DPIV. Since this effect occurs well before vortex ring pinch-off, it is an artifact with little influence on the measurements of importance to these experiments. Nonetheless, we can quantitatively bound this effect by assuming that the vortex cores possess a Gaussian vorticity distribution and enter the measurement window in a quasi-steady fashion. The fluid circulation entering the measurement window due to this motion will then be an error function of time by definition, since the circulation measurement is the definite integral of an assumed normal distribution of vorticity (centered at the vortex core) over the finite spatial region $0.3D_p \leq X \leq 6.2D_p$. Figure 6.6 indicates one such curve that effectively bounds the scatter in these experiments.

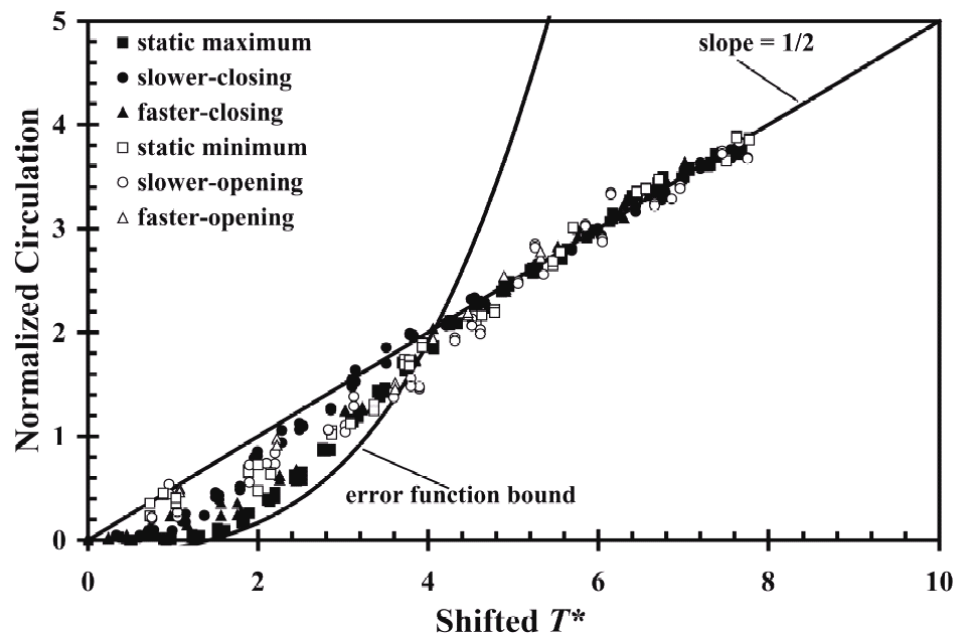


Figure 6.6 Normalized circulation versus formation time for each program of nozzle exit diameter temporal variation. Solid lines indicate slope = 1/2 and error function bound.

As an aside, the reader may be tempted to correlate the observed intersection of the linear and error function curves in figure 6.6 to the fact that pinch-off typically occurs at this same location in the space of normalized circulation versus formation time (i.e., $[T^*, \Gamma^*] = [4, 2]$). We strongly suggest that this is merely a coincidence in the present case. This conclusion is supported by the fact that, as previously mentioned, the data has been artificially shifted in formation time to force the linear trends to intersect the origin. In addition, the error function curve chosen to represent the lower bound of data scatter will change depending on the location of the upstream boundary of the measurement window. These choices are completely independent of the dynamics of leading vortex ring pinch-off.

6.3.3 *Leading vortex ring pinch-off and vorticity distribution*

With a dimensionless perspective on the fluid dynamics in place, we are prepared to examine the physics of leading vortex ring pinch-off. To reiterate, our focus on the pinch-off process is motivated by its dynamical significance as discovered by Krueger (2001), and the possibility of generating vortex rings of low dimensionless energy as implied by the results of Mohseni et al. (2001).

The method of Gharib et al. (1998) is used to determine the dimensionless vortex formation time corresponding to the onset of pinch-off, i.e., the *formation number* F . By measuring the circulation of the leading vortex ring after pinch-off, the formation time at which this circulation was generated by the starting flow is found. Figure 6.7 plots the dimensionless circulation versus formation time for the SMIN, SO, and FO nozzle cases. The formation time at the onset of pinch-off consistently falls between 3.7 and 4.4 for each group. These data are in agreement with the range observed by Gharib et al. (1998).

Contrary to the prediction of Mohseni et al. (2001), we do not observe a significant delay in vortex ring pinch-off for the cases with temporally increasing nozzle exit diameter.

Our finding is consistent with the results of Allen (2003), who also did not observe a beneficial effect of a temporally increasing exit diameter on vortex ring formation. Further examination of the leading vortex ring vorticity profile for each case provides the insight necessary to understand why the method has been ineffective. Figure 6.8 plots the vorticity profile along a radial section of the leading vortex ring at the formation number. For the SMIN case, the core vorticity distribution is qualitatively similar to a Gaussian-type profile. When the nozzle exit diameter is increased temporally as the starting flow emerges, the locations of peak core vorticity and the core vorticity centroid are both moved radially away from the axis of symmetry, as Mohseni et al. (2001) predicted. Furthermore, the radial motions of the vorticity peak and centroid occur nearly in direct proportion to the radial motion of the nozzle exit diameter.

However, in each case the portions of the shear layer closer to the axis of symmetry are unaffected by the nozzle motion; the near-axis vorticity consistently extends to the symmetry axis at the same formation time as the static nozzle case. We can conclude that although the temporal increase in nozzle exit diameter was effective in manipulating the radial location of peak vorticity in the core, the nozzle motion was insufficient to prevent the entire shear layer from encroaching on the axis of symmetry. Movement of the entire shear layer away from the centerline is necessary to delay vortex ring pinch-off.

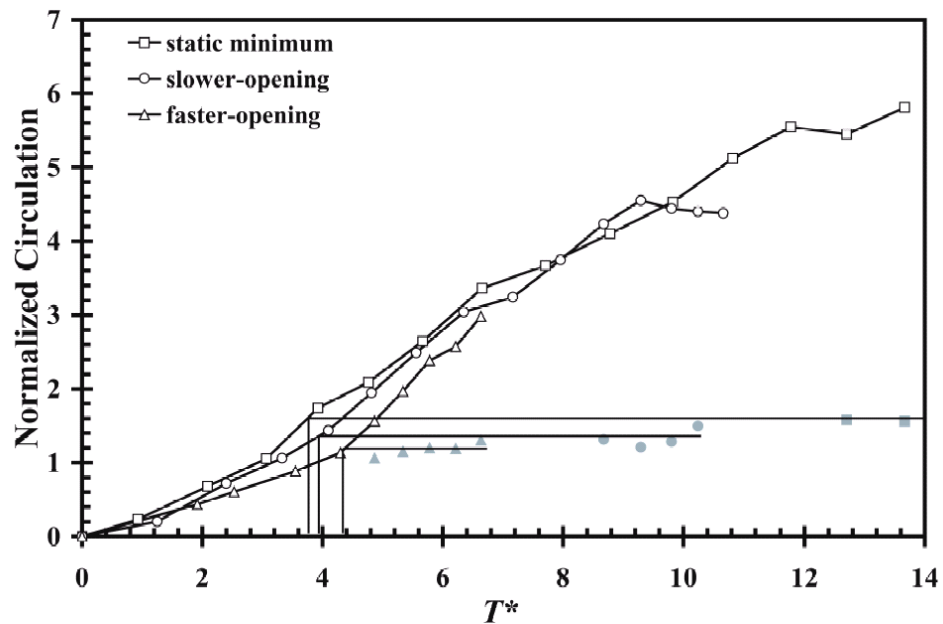


Figure 6.7 Normalized circulation versus formation time for SMIN, SO, and FO cases. Gray symbols indicate circulation of leading vortex ring after pinch-off.

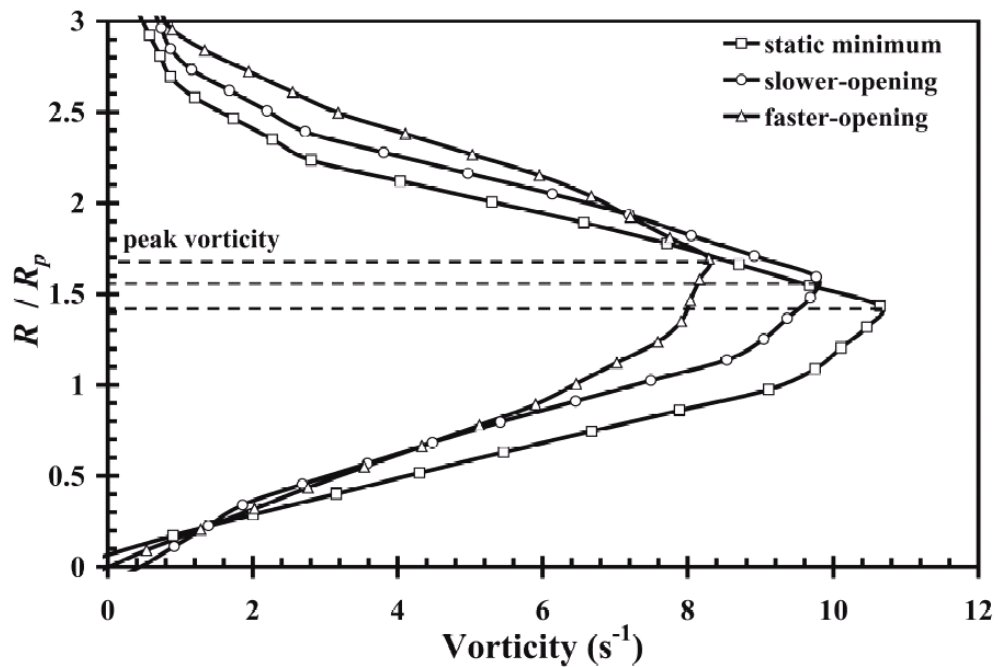


Figure 6.8 Vorticity profile along radial section of vortex ring core for SMIN, SO, and FO cases. Dashed lines indicate location of peak vorticity in each profile.

The present results may be attributed in part to the thickness of the shear layer at the relatively low Reynolds numbers of these experiments. We remain open to the possibility that at much higher Reynolds numbers, the shear layer might be sufficiently thin that it uniformly follows the motion of the vorticity peak. A more general discussion of dynamical benefits of the temporally increasing nozzle exit diameter is reserved for the concluding section of this chapter.

Circulation data for the SMAX, SC, and FC nozzle cases is shown in figure 6.9. In the absence of nozzle motion (i.e., SMAX case), leading vortex ring pinch-off occurs at a maximum formation number of 4.6. This is reasonably consistent with the range reported by Gharib et al. (1998). When a temporally decreasing nozzle exit diameter is introduced, the formation number increases substantially, to 6.9 for the SC case and to 8.0 for the FC case. This delay in vortex ring pinch-off is dramatically greater than that achieved by Dabiri and Gharib (2004a) using an external bulk counter-flow. Normalized circulation of the leading vortex ring is also increased by up to 35% over the static nozzle case.

For consistency with the preceding analysis, we plot the vorticity distribution along a radial section of the vortex ring core for the SMAX, SC, and FC cases at the formation number (figure 6.10). Unlike the trend observed for the radially-increasing exit diameter, the radially-decreasing exit diameter has little effect on the location of peak vorticity or the core vorticity centroid. There is, however, a large change in the magnitude of peak vorticity. The FC nozzle case exhibits peak vorticity at nearly double the peak level of the static nozzle. In addition, the temporally decreasing exit diameter nozzle cases possess a distinct discontinuity in the slope of the vorticity distribution approximately $1R/R_p$ from the axis of symmetry.

The vortex dynamics leading to these observed pinch-off and vorticity distribution trends are best explained in the context of a discourse on the leading vortex ring energy, as follows.

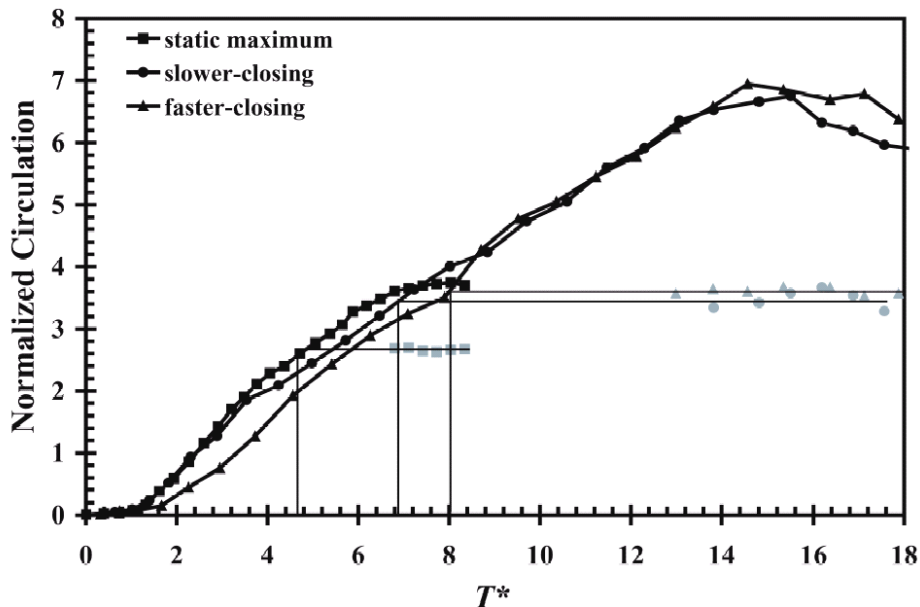


Figure 6.9 Normalized circulation versus formation time for SMAX, SC, and FC cases. Gray symbols indicate circulation of leading vortex ring after pinch-off.

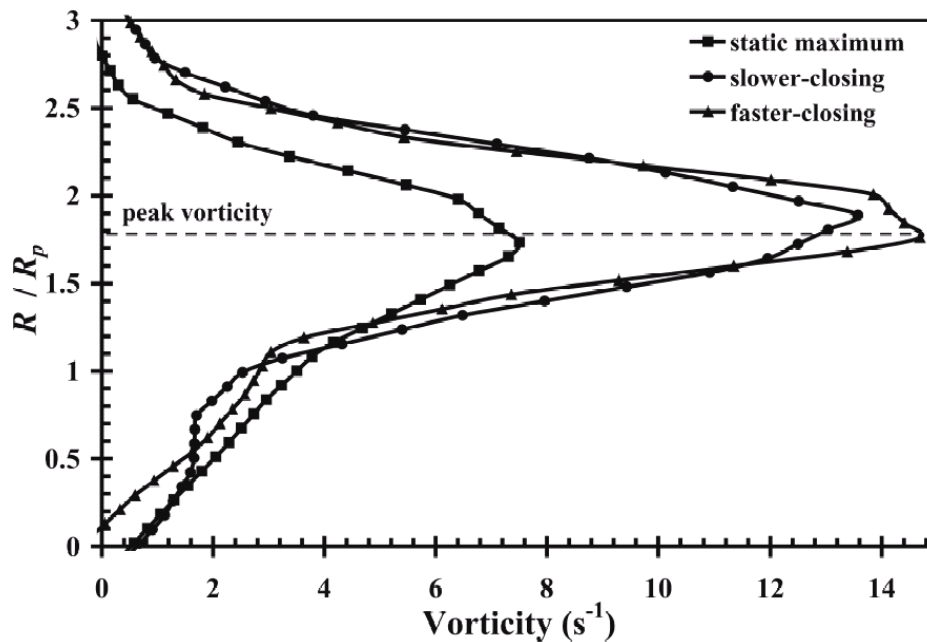


Figure 6.10 Vorticity profile along radial section of vortex ring core for SMAX, SC, and FC cases. Dashed line indicates approximate location of peak vorticity in each profile.

6.3.4 Leading vortex ring energy

The dimensionless vortex ring energy E^* is an especially useful parameter for investigating the dynamics of these starting flows, as it invokes the dynamical invariants being delivered from the vortex generator. Measuring the vortex ring energy is difficult in practice because it requires powers, quotients, and integrals of the velocity and vorticity fields:

$$E^* = \frac{E}{I^{1/2} \Gamma^{3/2}} = \frac{\pi \int \omega \psi dx dr}{\left[\pi \int \omega r^2 dx dr \right]^{1/2} \left[\int \omega dx dr \right]^{3/2}}, \quad (6.3.8)$$

where E , I , and Γ are the dimensional energy, impulse, and circulation, respectively, and ψ is the streamfunction. The velocity and vorticity fields have been measured with nonzero error, which will subsequently compound when computing the dimensionless energy. An additional source of uncertainty arises in selection of the vorticity contour that will be used to define the vortex core. Definitions of the vortex core based on a given vorticity contour level are *ad hoc* and make comparison between different cases somewhat tenuous.

A reliable method of obtaining the leading vortex ring energy is indicated in the work of Gharib et al. (1998). As dictated by the Kelvin-Benjamin variational principle, we can exploit the fact that the leading vortex ring energy is equal to the instantaneous energy of source flow delivered by the vortex generator at the formation number.

Using this strategy, we first revisit the pinch-off results for nozzle cases with temporally increasing exit diameter. Figure 6.11(a) plots the dimensionless energy supplied by the vortex generator in the SMIN, SO, and FO cases (using the exit velocity $U_e(t)$ to compute source flow impulse and energy), along with the leading vortex ring energy. For the SMIN case, the dimensionless energy of the leading vortex ring is 0.40. This value is

higher than that found by Gharib et al. (1998) but in the range of Mohseni et al. (2001) for vortex rings with similar normalized circulation. Movement of the peak vorticity away from the axis of symmetry by the nozzle motion results in vortex ring vorticity distributions with larger normalized energy, over 0.5 for the FO nozzle.

It is interesting to note that the nozzles with temporally increasing exit diameter successfully deliver source flow at higher dimensionless energy than the static nozzle case. Gharib et al. (1998) predict that this condition of increased dimensionless energy from the vortex generator is necessary in order to achieve a delay in pinch-off of the leading vortex ring. However, in the present experiments the concomitant increase in leading vortex ring energy due to vorticity redistribution (viz. radial movement of the core vorticity peak and centroid) negates any potential benefit from the increased energy source. If the source flow could be delivered at the same elevated energy level without affecting the leading vortex ring vorticity distribution, a substantial delay in vortex ring pinch-off might be achieved.

The dynamics of the SC and FC cases are more complex. In these nozzle cases, we observed substantial increases in the formation number and the normalized circulation of the leading vortex ring. One of two effects (or perhaps a combination thereof) can be expected to play a role in the augmented starting flow dynamics. In the first case, one might suspect that the increasing source flow velocity enables delay of leading vortex ring pinch-off, as predicted by Shusser and Gharib (2000) and Mohseni et al. (2001). Alternatively, the nozzle motion may have induced a change in the distribution of vortex ring vorticity, resulting in a lower dimensionless energy of the leading vortex ring and an associated decrease in the required source flow energy to sustain ring growth.

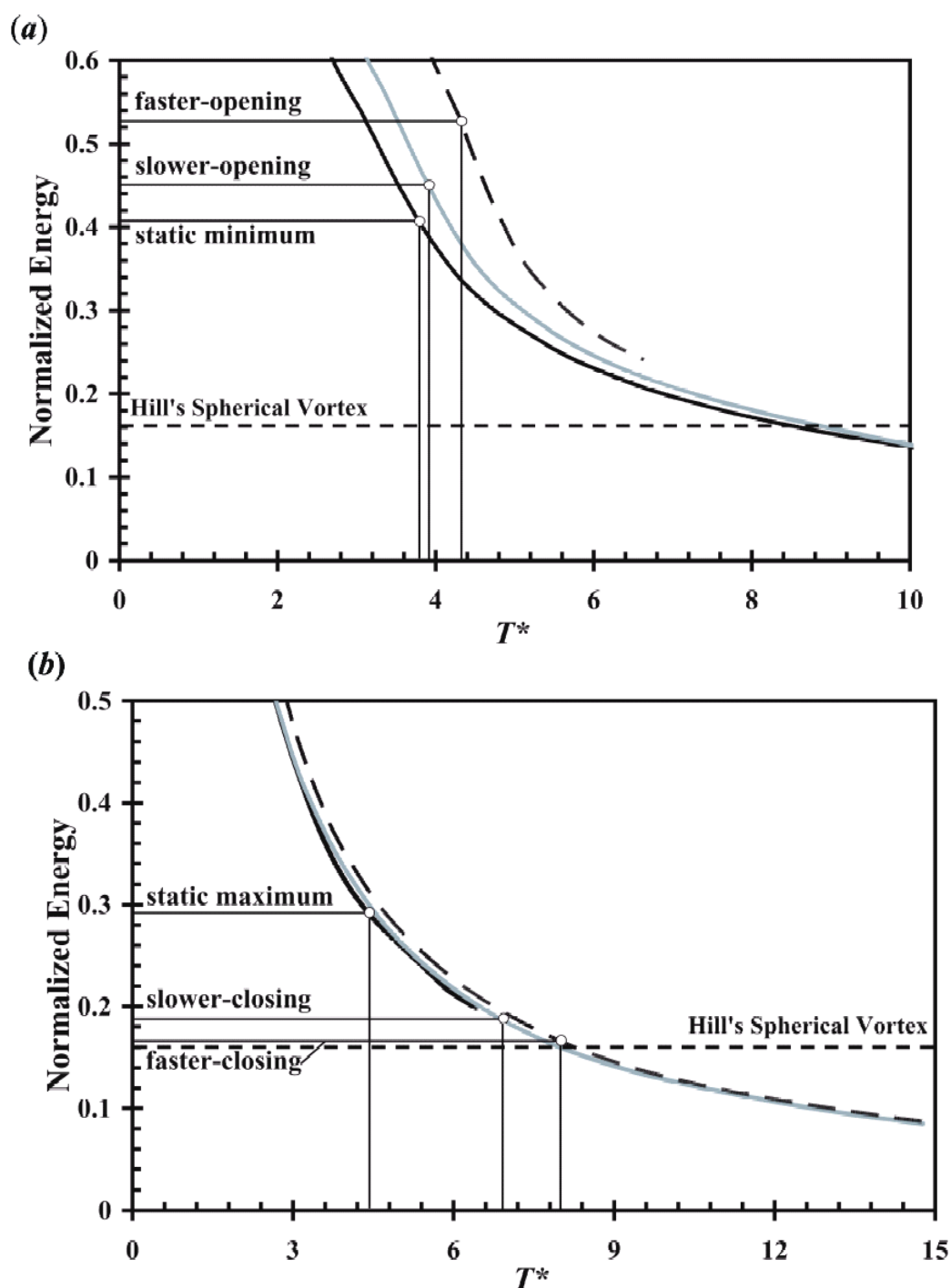


Figure 6.11 Normalized vortex generator energy versus formation time. Circled points in each plot indicate leading vortex ring energy. (a) SMIN, SO and FO cases. (b) SMAX, SC and FC cases.

Figure 6.11(b) indicates that the latter of these two effects is present. Unlike the temporally-increasing nozzle exit diameter, the temporally-decreasing cases have little effect on the dimensionless energy carried by source flow from the vortex generator. Hence we can conclude that it is changes in the vortex ring vorticity distribution that have led to the observed delay in vortex ring pinch-off, and not some characteristic of the source flow such as its velocity.

The development of the leading vortex ring vorticity distribution in temporally-decreasing nozzle exit diameter cases is distinct from both the static nozzle and the temporally increasing nozzle exit diameter cases. Vorticity contours of the normal process are shown in figure 6.12, just before and after pinch-off from the SMAX nozzle. The shear layer efflux behaves in the expected fashion, emerging parallel to the axis of symmetry and possessing a larger region of concentrated vorticity in the leading vortex ring core. In the case of nozzle exit diameter contraction (figure 6.13), the vorticity flux is ejected closer to the axis of symmetry as time progresses. A portion of this vorticity is convected axially toward the front stagnation point of the starting flow by the circulatory motion of the leading vortex ring. Figures 6.13(b)-(d) track the vorticity traveling from the rear of the ring to the front stagnation point. The remainder of the shear layer efflux left behind the leading vortex ring interacts with its mirror image across the axis of symmetry, contributing to disconnection of the leading vortex ring.

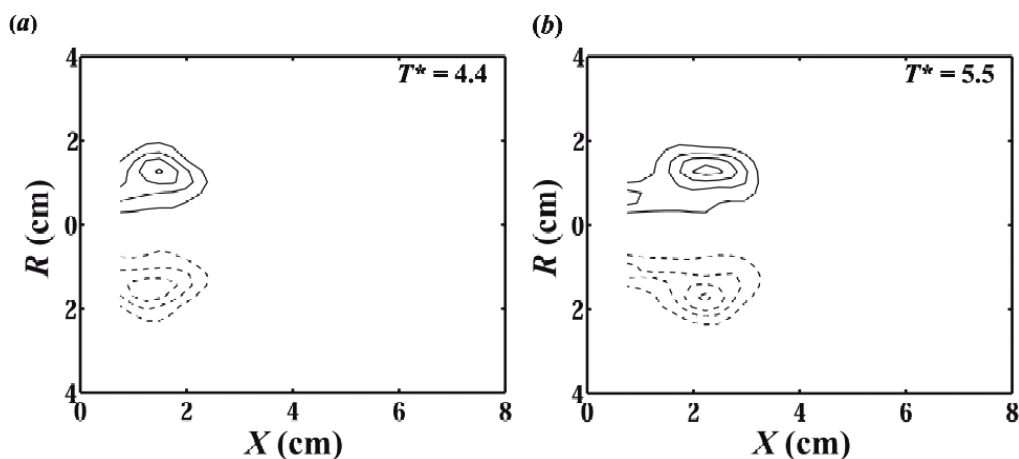


Figure 6.12 Vorticity contours of the flow downstream of the static maximum diameter nozzle. Flow is from left to right. Solid and dashed lines indicate positive and negative vorticity, respectively. Contour spacing is 2 s^{-1} .

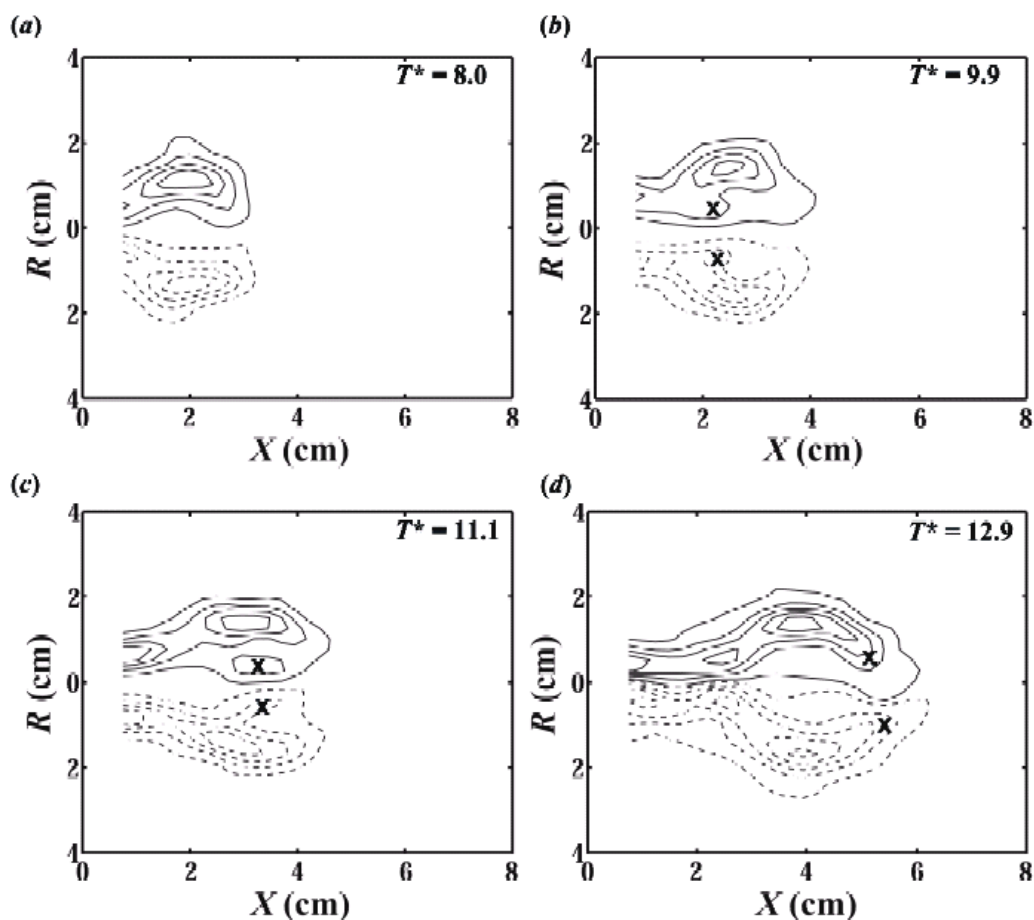


Figure 6.13 Vorticity contours of the flow downstream of the FC diameter nozzle. Flow is from left to right. Solid and dashed lines indicate positive and negative vorticity, respectively. Contour spacing is 3 s^{-1} . Downstream convection of vorticity along the axis of symmetry is tracked by a cross symbol placed at the local vorticity peak.

Crescent-shaped vorticity patches arise in the leading vortex ring after this process (e.g., figure 6.13*d*), in contrast with the typical elliptic patches. In the preceding section, the vorticity distribution near the axis of symmetry was noted to display a trend different from the typical Gaussian profile. From figure 6.13 we can now see that this effect is due to the shear layer vorticity that was fed close to the axis of symmetry and subsequently passed from the rear of the ring to the front stagnation point. The motion of this vorticity also appears to have prevented the leading vortex ring cores from following the nozzle wall motion toward the axis of symmetry, as was observed (in the opposite sense) in the temporally-increasing nozzles. This explains the difference in the dynamics of the vorticity peaks plotted in figures 6.8 and 6.10.

Vortex rings with very low dimensionless energy are generated by the process described above. Starting flow through the FC nozzle formed leading vortex rings with dimensionless energy equal to 0.165 ± 0.009 . This value agrees with direct measurements using equation (6.3.8), which gave values in the range of 0.16 ± 0.02 . For comparison, Hill's spherical vortex has a dimensionless energy of 0.160. The vortex rings generated in the present experiments are not Hill's vortices, however, because the vorticity distribution is not uniformly linear in the radial direction. Furthermore, the rings could potentially have dimensionless energy lower than that of Hill's vortex, as demonstrated by Mohseni et al. (2001) for vortex rings formed at low Reynolds numbers (i.e., less than 1000 based on the leading vortex ring circulation). Nonetheless, the comparison with Hill's vortex is noteworthy because previous analytical studies of the pinch-off process have invoked the Norbury family of vortices, which includes Hill's vortex as its limiting member (e.g., Gharib et al., 1998; Mohseni et al. 2001; Linden and Turner, 2001). In particular Linden

and Turner (2001) predict that vortex rings with dimensionless energy equal to Hill's vortex can be achieved by a constant-diameter piston-cylinder apparatus if pinch-off is delayed until a dimensionless vortex formation time of 7.83. That predicted pinch-off time is very close to the values observed here for vortex rings with Hill-type dimensionless energy formed by the FC nozzle.

6.3.5 *Leading vortex ring fluid transport*

Finally, we present an aspect of starting flow dynamics that is largely absent from the literature; namely, the issue of how much fluid is transported by the leading vortex ring of the starting flow. Although the preceding sections have identified effective means to delay pinch-off and produce vortex rings with low dimensionless energy and high normalized circulation, we must ask if there is any penalty being paid in the process of mass transfer relative to the static nozzle cases. Since the volume flux through each nozzle is identical, such a comparison can be made given the available data.

Figure 6.14 plots the volume of source flow carried in the leading vortex ring of each starting flow through a temporally variable nozzle exit diameter, $\Omega(t)$, relative to its static nozzle counterpart at pinch-off Ω_0 . Temporal increases in the nozzle exit diameter have a minor effect on the volume of fluid transported by the leading vortex ring. In contrast, the temporally decreasing nozzle exit cases deliver only 80% of the fluid that the static nozzle is capable of transporting via the leading vortex ring. The practical significance of this performance limit will depend on the details of a particular application, especially the expense of reciprocating the motion to generate additional vortex rings. Nonetheless this result clearly demonstrates the need to examine starting flow performance from several perspectives, both dimensional and independent of physical units.

Table 1 summarizes relevant dimensional parameters of the leading vortex rings measured in each test case. This data complements the dimensionless perspective commonly taken to study the dynamics of vortex ring pinch-off.

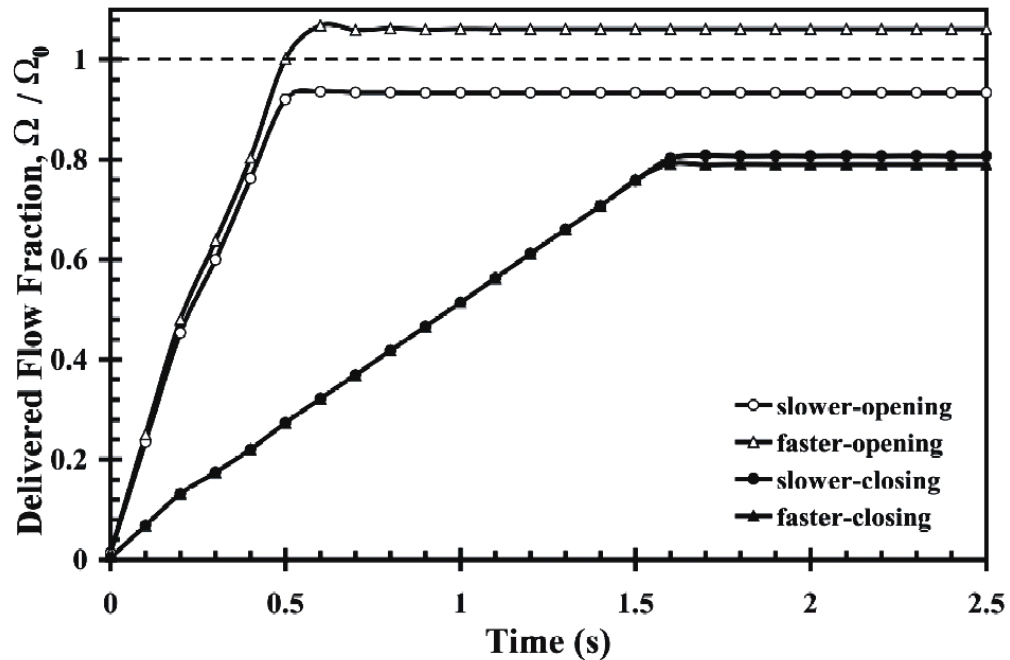


Figure 6.14 Delivered fluid fraction for leading vortex rings in nozzle cases with temporally variable exit diameter.

Nozzle Program	Formation Number	Pinch-off Time	Vortex Circulation	Vortex Diameter
SMIN	3.7	0.57 s	17.5 cm ² s ⁻¹	3.6 cm
SO	3.9	0.53	14.5	4.1
FO	4.3	0.60	13.4	4.3
SMAX	4.6	1.95	17.9	4.4
SC	6.9	1.56	30.2	4.8
FC	8.0	1.54	32.8	4.5

Table 6.1 Dimensional parameters of the leading vortex ring for each nozzle program. Values are representative and possess a maximum uncertainty of $\pm 5\%$.

6.4 Summary and Conclusions

This chapter has described a detailed experimental study of starting flow through nozzles with temporally variable exit diameter. Our strategy has been to decouple the source flow from the nozzle dynamics in order to successfully facilitate comparison among various classes of nozzle motion.

An important tool in these analyses has been the use of a dimensionless perspective on the evolution of the starting flows. We have defined a new parameter to track the temporal development of the dynamics, which properly accounts for the effect of a temporally variable exit diameter. Improved kinematic models based on a generalized description of the source flow are demonstrably successful in predicting the circulation delivered by the vortex generator after initial vortex ring roll-up. These models have also helped to emphasize the important contribution of the boundary layer to starting flow dynamics.

Several previously unresolved questions regarding the nature of the leading vortex ring in starting flows have been answered or at least refined, through a study of the pinch-off process and vortex ring vorticity distribution and energy. We have shown that temporally increasing the nozzle exit diameter as the starting flow emerges leads to a measurable increase in the radial location of peak vorticity in the leading vortex ring. Consequently, the energy of the leading vortex ring is increased. Since the energy delivered by the vortex generator is also increased in the process, the two effects counteract one another, preventing a change in the normalized circulation of the leading vortex ring or the dimensionless time at which pinch-off occurs.

These experiments have demonstrated the ability of a temporally decreasing nozzle exit to facilitate substantial increases in the formation number and normalized circulation of the leading vortex ring. In the process, vortex rings with very low normalized energy were produced. Examination of the vorticity contours revealed a unique transient effect during development of these starting flows, in which vorticity from the trailing shear layer was forced through the center of the forming vortex ring by the nozzle motion and induced velocity of the ring.

Finally, we have briefly discussed the concept of dimensional fluid transport by the leading vortex ring, to demonstrate a trade-off that may possibly exist between energetic improvements to the starting flow process and the ability of the flow to facilitate mass transfer.

The existing research related to this specific problem is limited; however, the present results are consistent in principle with those previous findings. It has been observed here that the prediction of Mohseni et al. (2001) of thick vortex ring generation by increasing the spatial extent of flow forcing may possibly be achieved if the shear layer efflux is sufficiently thin that it behaves uniformly with the vorticity peak. In the present experiments, the spatially-increasing nozzle motions effectively actuated the location of peak vorticity; however, the shear layer was too thick to prevent encroachment of the near-axis vorticity on the centerline. Allen (2003) appears to have also been unable to prevent this from occurring with his apparatus.

These experiments indicate that the benefit of a temporally decreasing nozzle diameter for generation of thick, low-energy vortex rings is related to changes in the vorticity distribution of the forming leading vortex ring that are induced by the nozzle

motion. Although we suggest that this mechanism is dynamically distinct from the alternative explanation based on the velocity of the trailing source flow (e.g., Shusser and Gharib, 2000; Mohseni et al. 2001), it could be reasonably argued that the two effects are similar from a kinematic perspective. Again, these results are at least qualitatively in agreement with the observations of Allen (2003).

It is prudent to discuss the limitations of the experimental techniques and strategy employed herein. Perhaps the most immediate observation is that these experiments have all been conducted with a single nozzle-type exit geometry. Given that the vortex ring trajectory can be influenced by the nature of the vortex generator exit boundary conditions (e.g., nozzle or orifice; Auerbach, 1987), the quantitative trends measured in the present work may be adjusted for other exit geometries. This is especially true in the application of these results to biological systems, many of which also deviate from axisymmetry in the exit shape. Two common examples are the lappets at the bell margin of many scyphozoan jellyfish (e.g., Dabiri and Gharib, 2003) and the funnels of some squids (e.g., Anderson and DeMont, 2000).

Fluid continuity demands that our decision to decouple the source flow volume flux from the nozzle motion must be paid for in a new coupling between the diameter and flow velocity at the nozzle exit plane. This could potentially complicate interpretation of the results, since the exit plane velocity will be decreasing as the exit diameter increases and *vice versa*.

The plots of dimensionless energy in figure 6.11 confirm that this was not an important factor in the present experiments. Despite the decrease in nozzle exit plane velocity while the exit diameter was increasing, we see that the delivered energy still

increased, following the trend commanded by the nozzle exit diameter (figure 6.11*a*).

Similarly, despite the relatively large increase in nozzle exit velocity while the exit diameter was decreasing, the delivered energy remained unaffected (figure 6.11*b*).

It remains plausible that for experiments with constant flow velocity at the exit plane, the temporally increasing nozzle exit diameter cases might show even greater increase in the delivered energy, and the temporally decreasing nozzle exit diameter cases might suffer decreases in the delivered energy. These scenarios can be neither conclusively affirmed nor refuted given the available experimental apparatus; however, we can anticipate that any effect will be consistent across each class of nozzle motion and therefore preserve the qualitative trends observed here. As a final support of the selected strategy of allowing coupling between the exit plane diameter and flow velocity, we note that in the biological systems of relevance to these experiments, such a coupling is commonly observed (e.g., Yoganathan and Lemmon, 2002; Dabiri and Gharib, 2003).

We conclude with a brief summary of some anticipated benefits of temporal variation of the exit diameter during pulsatile flow generation, based on the results of this study. Temporal increases in the exit diameter will be primarily useful for enhancing the impulse delivered by the vortex generator source flow, at the expense of ejection efficiency. In addition, the corresponding increase in the radial extent of the leading vortex ring cores can provide substantial augmentation of ambient fluid entrainment by the starting flow, facilitating transfer of the impulse to a greater volume of fluid (Dabiri and Gharib, 2004c). This strategy will be useful in systems that occasionally require rapid momentum or mass transport at high cost (i.e., energy input), such as the escape

mechanism of squid and cardiac pumping at elevated heart rates associated with systemic stress.

Temporal decreases in the nozzle exit diameter during flow initiation will increase efficiency of the flow ejection process, as measured by the impulse carried in each vortex ring per unit of energy expended. Systems requiring robust, high-efficiency performance will benefit from this strategy. These experiments have demonstrated that the volume of fluid delivered in each vortex ring is reduced for this class of nozzle motion. However, the enhanced efficiency will facilitate additional iterations of the ejection mechanism in order to compensate without severe penalty. The measured kinematics of jellyfish swimming are consistent with this strategy, although empirical measurements of locomotive efficiency have not yet been achieved for these animals.

In final analysis, these experiments have conclusively demonstrated potential dynamical benefits from both spatially increasing and decreasing classes of temporal nozzle exit diameter variation. Many of the trends observed here cannot be predicted by quasi-steady analysis—unsteady mechanisms must be considered. Optimal nozzle actuation will be dictated by the particular application of interest and external constraints imposed on the design of the vortex generator. We have shown here that the search for these optimal points can lead to substantial improvements in system performance.

6.5 Chapter References

Adrian R. J. 1991 Particle-imaging techniques for experimental fluid-mechanics. *Annu. Rev. Fluid Mech.* **23**, 261-304.

- Anderson E. J. and DeMont M. E. 2000 The mechanics of locomotion in the squid *Loligo pealei*: locomotory function and unsteady hydrodynamics of the jet and intramantle pressure. *J. Exp. Biol.* **203**, 2851-2863.
- Auerbach D. 1987 Experiments on the trajectory and circulation of the starting vortex. *J. Fluid Mech.* **183**, 185-198.
- Bartol I. K., Patterson M. R. and Mann R. 2001 Swimming mechanics and behavior of the shallow-water brief squid *Lolliguncula brevis*. *J. Exp. Biol.* **204**, 3655-3682.
- Benjamin T. B. 1976 The alliance of practical and analytical insights into the non-linear problems of fluid mechanics. In *Applications of Methods of Functional Analysis to Problems in Mechanics*, (ed. Germain P. and Nayroles B.). *Lect. Notes Math.* **503**, 8-28.
- Dabiri J. O. and Gharib M. 2003 Sensitivity analysis of kinematic approximations in dynamic medusan swimming models. *J. Exp. Biol.* **206**, 3675-3680.
- Dabiri J. O. and Gharib M. 2004 Delay of vortex ring pinch-off by an imposed bulk counter-flow. *Phys. Fluids* **16**, L28-L30.
- Dabiri J. O. and Gharib M. 2004 A revised slug model boundary layer correction for starting jet vorticity flux. *Theor. Comput. Fluid Dyn.* **17**, 293-295.
- Dabiri J. O. and Gharib M. 2004 Fluid entrainment by isolated vortex rings. *J. Fluid Mech.* **511**, 311-331.
- Daniel T. L. 1983 Mechanics and energetics of medusan jet propulsion. *Can. J. Zool.* **61**, 1406-1420.
- Didden N. 1979 Formation of vortex rings—rolling-up and production of circulation. *Z. Angew. Math. Phys.* **30**, 101-116.

- Gharib M., Rambod E. and Shariff K. 1998 A universal time scale for vortex ring formation. *J. Fluid Mech.* **360**, 121-140.
- Glezer A. and Amitay M. 2002 Synthetic jets. *Annu. Rev. Fluid Mech.* **34**, 503-529.
- Gorman J. H. III, Gupta K. B., Streicher J. T., Gorman R. C., Jackson B. M., Ratcliffe M. B., Bogen D. K. and Edmunds L. H. Jr. 1996 Dynamic three-dimensional imaging of the mitral valve and left ventricle by rapid sonomicrometry array localization. *J. Thorac. Cardiovasc. Surg.* **112**, 712-726.
- Handke M., Heinrichs G., Beyersdorf F., Olschewski M., Bode C. and Geibel A. 2003 In vivo analysis of aortic valve dynamics by transesophageal 3-dimensional echocardiography with high temporal resolution. *J. Thorac. Cardiovasc. Surg.* **125**, 1412-1419.
- Joslin R. D. 1998 Aircraft laminar flow control. *Annu. Rev. Fluid Mech.* **30**, 1-29.
- Kelvin W. T. 1875 Vortex statics. *Collected Works* **4**, 115-128. Cambridge University Press.
- Krueger P. S. 2001 The significance of vortex ring formation and nozzle exit over-pressure to pulsatile jet propulsion. Ph.D. Thesis, California Institute of Technology, Pasadena, CA.
- Krueger P. S. and Gharib M. 2003 The significance of vortex ring formation to the impulse and thrust of a starting jet. *Phys. Fluids* **15**, 1271-1281.
- Krutzsch C.-H. 1939 Über eine experimentell beobachtete erscheinung an wirbelringen bei ihrer translatorischen bewegung in wirklichen flüssigkeiten. *Ann. Phys.* **35**, 497-523.

- Linden P. F. and Turner J. S. 2001 The formation of 'optimal' vortex rings, and the efficiency of propulsion devices. *J. Fluid Mech.* **427**, 61-72.
- Mohseni K. 2001 Statistical equilibrium theory for axisymmetric flows: Kelvin's variational principle and an explanation for the vortex ring pinch-off process. *Phys. Fluids* **13**, 1924-1931.
- Mohseni K. and Gharib M. 1998 A model for universal time scale of vortex ring formation. *Phys. Fluids* **10**, 2436-2438.
- Mohseni K., Ran H. Y. and Colonius T. 2001 Numerical experiments on vortex ring formation. *J. Fluid Mech.* **430**, 267-282.
- Rosenhead L. 1963 *Laminar Boundary Layers*. Clarendon Press.
- Rosenfeld M., Rambod E. and Gharib M. 1998 Circulation and formation number of laminar vortex rings. *J. Fluid Mech.* **376**, 297-318.
- Saffman P. G. 1978 The number of waves on unstable vortex rings. *J. Fluid Mech.* **84**, 625-639.
- Shariff K. and Leonard A. 1992 Vortex rings. *Annu. Rev. Fluid Mech.* **24**, 235-279.
- Shariff K., Verzicco R. and Orlandi P. 1994 A numerical study of 3-dimensional vortex ring instabilities—viscous corrections and early nonlinear stage. *J. Fluid Mech* **279**, 351-375.
- Shusser M. and Gharib M. 2000 Energy and velocity of a forming vortex ring. *Phys. Fluids* **12**, 618-621.
- Shusser M., Gharib M., Rosenfeld M. and Mohseni K. 2002 On the effect of pipe boundary layer growth on the formation of a laminar vortex ring generated by a piston/cylinder arrangement. *Theor. Comput. Fluid Dyn.* **15**, 303-316.

- Vogel S. 1988 *Life's Devices*. Princeton University Press.
- Vogel S. 1994 Nature's pumps. *Am. Sci.* **82**, 464-471.
- Widnall S. E., Bliss D. B. and Tsai C.-Y. 1974 The instability of short waves on a vortex ring. *J. Fluid Mech.* **66**, 35-47.
- Widnall S. E. and Tsai C.-Y. 1977 The instability of the thin vortex ring of constant vorticity. *Philos. T. Roy. Soc. A* **287**, 273-305.
- Willert C. E. and Gharib M. 1991 Digital particle image velocimetry. *Exp. Fluids* **10**, 181-193.
- Yogonathan A. P., Lemmon J. D. and Ellis J. T. 2002 Heart valve dynamics. In *The Biomedical Engineering Handbook*. CRC Press LLC.
- Zhao W., Frankel S. H. and Mongeau L. G. 2000 Effects of trailing jet instability on vortex ring formation. *Phys. Fluids* **12**, 589-596.

CHAPTER 7: Sensitivity analysis of kinematic approximations in dynamic medusan swimming models

Submitted to Journal of Experimental Biology July 14, 2003

7.0 Chapter Abstract

Models of medusan swimming typically rely on kinematic approximations to observed animal morphology to make such investigations tractable. The effect of these simplifications on the accuracy of predicted dynamics has not been examined in detail. We conduct a case study of the scyphozoan jellyfish *Chrysaora fuscescens* to isolate and quantify the sensitivity of dynamic models to common kinematic approximations. It is found that dynamic models exhibit strong dependence on the nature of some approximations and the context in which they are implemented. Therefore it is incorrect and potentially misleading to assume that achieving kinematic similarity in models of measured animal locomotion will necessarily provide dynamically correct models.

7.1 Introduction

The apparent simplicity of the medusan propulsive mechanism has enabled the development of models describing associated kinematics and dynamics. Daniel (1983) derived equations of motion for medusan jet propulsion, based on the principle that swimming thrust is produced by the flux of fluid momentum from the bell during the contraction phase of each propulsive cycle. This thrust is used to overcome drag on the bell surface, and to accelerate the medusa and surrounding fluid (i.e., added-mass effect, cf. Batchelor, 1967; Webb, 1982). While a synergy of experiment and theory has been

successfully implemented to further examine relationships between mechanics and energetics of medusan propulsion (Daniel, 1985; DeMont and Gosline, 1988a-c), studies of kinematics and dynamics have relied primarily on empirical data. The morphology of several species of medusae has been measured *in situ* (Gladfelter, 1972; Costello and Colin, 1994, 1995; Ford et al., 1997; Ford and Costello, 2000; Colin and Costello, 2002). However, with the exception of comparisons made by Daniel (1983) between dynamical model predictions and measured kinematics, few explicit comparisons between theory and experiment have been made.

Recently, Colin and Costello (2002) undertook this type of study in a comparative analysis of prolate and oblate forms of hydromedusae. They reported agreement between observed swimming acceleration and model predictions for a prolate medusa (*Sarsia* sp.), but significant discrepancy for an oblate form (*Phialidium gregarium*). They attributed this result to differences in swimming mode between oblate and prolate medusae, where prolate forms may be more amenable to momentum jet models of swimming. Notwithstanding, there are substantial kinematic differences between prolate and oblate medusa that will be realized via kinematic inputs to the model, irrespective of swimming mode. This effect has not been examined. More generally, it is important in all comparative studies of animal locomotion models to contrast the effects of each kinematic approximation before attributing observed differences in the results of the model to behavior.

Specifically, there has been no complete, quantitative determination of the effects of various kinematic approximations employed in medusan swimming models. Two common assumptions are that the velar aperture area is constant throughout the propulsive cycle, and that the rate of bell volume change is constant during both the contraction and

expansion phases of the cycle. Perhaps more prevalent is the use of a single-parameter ‘finesness ratio’—the bell height divided by diameter—to completely describe the animal shape. Corollary to this parameter is the assumption that the bell can be approximated as a hemiellipsoid.

In sum, modeling of medusan swimming currently proceeds under the assumption that close kinematic approximation to observed animal morphology will necessarily yield corresponding approximate solutions to the dynamical equations of motion; this has not been verified. The mandate for this study is further amplified when one considers the prevalent use of this assumption in most models of animal locomotion. We report a quantitative case study of swimming scyphomedusae *Chrysaora fuscescens* that isolates the effect of each kinematic approximation mentioned above on the predictions of the dynamical model. As a baseline for comparison, an image-processing algorithm is developed to measure observed kinematics precisely.

7.2 Materials and Methods

7.2.1 Video recording and image processing

Chrysaora fuscescens (Brandt 1835) were observed in an optically backlit kriesel facility at the Aquarium of the Pacific (Long Beach, CA, USA). Video recordings of swimming motions were captured using a three-channel (RGB) digital video CCD camera with 30 Hz frame speed. To resolve the surface of selected medusae with sufficient precision for subsequent image processing, a lens was used to enlarge each medusa image to the outer boundary of the CCD array. The camera was manually positioned to track translation of the medusa as it swam upward in a vertical plane of the kriesel. Video

recordings of swimming medusae that did not occur in vertical planes were discarded so that no scaling of the final video was necessary to correct for changes in depth of the viewing plane.

Each three-channel (by 8-bit) frame of a selected set of swimming contractions was converted to black-and-white using a binary threshold filter. The threshold level was selected such that pixels containing portions of the bell were assigned logic-0 (black) and all others were assigned logic-1 (white). An uncertainty of 3% was associated with binary conversion, due to limited resolution of the boundary between the medusa bell surface and surrounding water.

A search algorithm was created to identify pixels at the logic-0 to logic-1 transitions, corresponding to the bell surface. These pixels were connected using a cubic spline interpolation method (Hanselman and Littlefield 2000). The spline data from one half of the bell (apex to margin) were then revolved around the medusa oral–aboral axis of symmetry to generate a three-dimensional, axisymmetric description of the bell morphology. The appropriateness of the axisymmetric description is suggested by axial symmetry of the locomotor structure in medusae (cf. Gladfelter, 1972). User input was required to determine the location of the bell margin, due to optical obstruction by the tentacles and oral arms. Uncertainty of the user input was determined to be 3-4%, based on measurement repeatability. An example half-spline is displayed in figure 7.1 on a frame of the swimming medusa, along with the three-dimensional reconstruction.

Kinematic data were obtained from the reconstructed medusa, including bell volume (assuming a thin mesogleal wall), aperture diameter, and fineness ratio. Wall thickness is not negligible near the apex. Bell volume measurements are not substantially

affected, however, due to limited volume change in the apical region throughout the propulsive cycle. Total uncertainty in bell volume and aperture area measurements was calculated to be 8% and 5%, respectively.

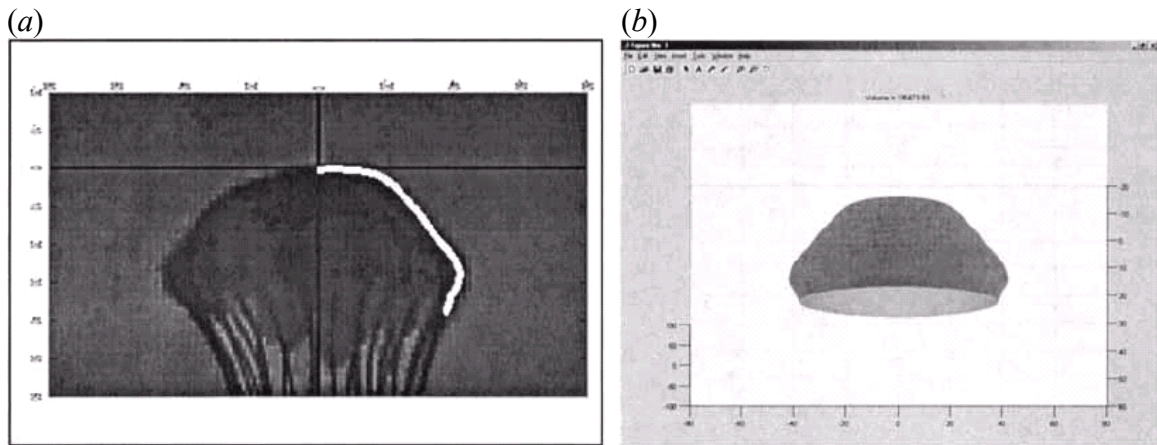


Figure 7.1 Video recording and image processing. (a) Video image frame with half-spline overlay. (b) Three-dimensional bell reconstruction generated by revolution of half-spline around axis of revolution.

7.2.2 Dynamical model

The implemented dynamical model for medusan swimming is principally that of Daniel (1983). The essence of the model is that thrust for swimming is generated by the flux of fluid momentum from the bell during each contraction phase. This thrust is used to accelerate the animal and surrounding fluid, and to overcome drag. By assuming a uniform profile of ejected fluid velocity, the generated thrust T can be computed as a function of time t , given the water density ρ , instantaneous bell volume V , and aperture area A :

$$T = \frac{\rho}{A} \left(\frac{dV}{dt} \right)^2. \quad (7.2.1)$$

Similarly, the drag and acceleration reactions can be computed from these parameters by utilizing the fact that medusae are nearly neutrally buoyant so that body

mass can be neglected (Denton and Shaw, 1961). Therefore, the dynamical equation of motion for the translational velocity $u(t)$ can be expressed as a nonlinear differential relationship:

$$V(t) \left[1 + \left(\frac{3V(t)}{2} \sqrt{\frac{\pi}{A(t)}} \right)^{1.4} \right] \frac{du}{dt} + \left(\frac{12\pi^{0.35} A(t)^{0.65}}{2^{0.7}} \right) u^{1.3} = T(t). \quad (7.2.2)$$

The fractional powers in (7.2.2) arise from empirical expressions for drag and added-mass coefficients. Equation (7.2.2) was solved using a fourth-order Runge–Kutta algorithm with time step equal to twice the temporal (frame rate) resolution of the data. The kinematic parameters $V(t)$ and $A(t)$ were input according to protocol described in the following sections.

7.2.3 Sensitivity analysis—bell volume and aperture area

The first set of experiments examined the effect of two common kinematic inputs to the dynamical model: approximating the aperture area as constant throughout the propulsive cycle, and assuming a constant rate of change of volume during both the contraction and expansion swimming phases. Table 7.1 indicates combinations of $V(t)$ and $A(t)$ that were input to the dynamical model.

The measured $V(t)$ and $A(t)$ refer to values obtained from the image processing algorithm. The approximate $V(t)$ was defined by assuming constant dV/dt during each contraction and expansion phase. The approximate $A(t)$ was defined as the average value of bell aperture area over several contractions.

Data Set Title	$V(t)$	$A(t)$
mVmA (baseline)	measured	Measured
aVmA	approximate	Measured
mVaA	measured	Approximate
aVaA	approximate	Approximate

Table 7.1 Data set definitions for kinematic inputs in first set of experiments. m, measured; a, approximate; V , volume; A , area; $V(t)$, $A(t)$, see text for explanation.

7.2.4 Sensitivity analysis—fineness ratio

The second set of experiments examined the effect of using a fineness ratio (bell height h divided by diameter d) to characterize the bell morphology. The characteristic diameter d was measured by two methods, using the bell aperture diameter and the maximum bell diameter. A volume $V(t)$ and area $A(t)$ were assigned to each fineness ratio measurement using a hemiellipsoid geometrical approximation; the semi-major and minor axes of the hemiellipsoid correspond to the medusa bell height and radius, respectively. Based on these kinematic inputs, the results of the dynamical model (equation 7.2.2) were then compared to the baseline case mVmA defined in table 7.1.

The need to video-record swimming medusae in a non-inertial frame of reference (i.e., to achieve sufficient image resolution) meant that we were unable to record absolute position, velocity, and acceleration of the animal. This limitation was circumvented in the comparative data analyses by referencing these dynamic quantities to the relative maxima in each experiment.

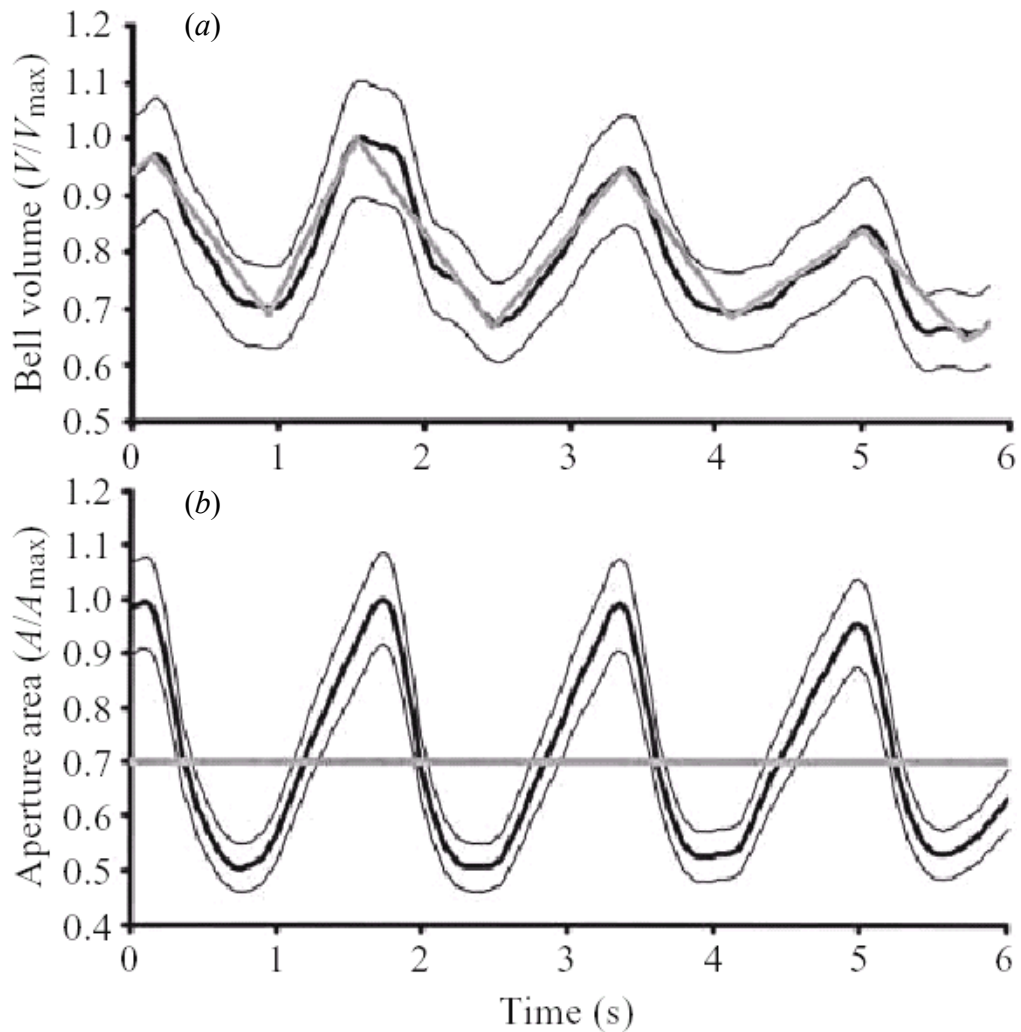


Figure 7.2 Measurements of *Chrysaora fuscescens* swimming. (a) Measured volume versus time. Thick black line, curve fit; thin black line, uncertainty boundaries; gray line, approximate $V(t)$. (b) Measured aperture area versus time. Thick black line, curve fit; thin black line, uncertainty boundaries; gray line, approximate $A(t)$. Values are normalized by maximum in the plot.

7.3 Results

7.3.1 Bell volume and aperture area approximations

Figure 7.2 plots measured bell volume V and aperture area A with their respective approximated curves. The amplitude of the volume curve is observed to decrease throughout the series of propulsive cycles, perhaps as a mechanism for drag reduction at higher speeds. Although this is of no immediate consequence, it demonstrates the ability of the measurement technique to capture both transient and long-term effects.

Dynamical model predictions of medusa acceleration, velocity, and position for each data set defined in table 7.1, are shown in figure 7.3. Data sets $mVmA$ and $mVaA$ show substantial peaks in acceleration at the beginning of each contraction. This is consistent with observations by Colin and Costello (2002) for hydromedusae with similar Bauplane. The remaining two data sets, $aVmA$ and $aVaA$, do not realize the spikes in acceleration. They are more qualitatively similar to the acceleration simulated by Daniel (1983). The velocity and position predictions of the dynamical model, as expected, show a trend similar to the acceleration. The predicted medusa velocity and position for measured volume cases $mVmA$ and $mVaA$ show qualitative agreement with previous experimental measurements (e.g., Costello and Colin, 1994, 1995; Colin and Costello, 2002), whereas the approximated volume results correspond well with simulated dynamical predictions (e.g., Daniel, 1983).

7.3.2 Fineness ratio approximation

Ultimately, the purpose of the fineness ratio in the dynamical model is to provide an estimate of bell volume, assuming the bell can be approximated by a hemiellipsoid. Therefore, it is useful to compare direct fineness ratio measurement with the corresponding fineness ratio computed from measured volume data.

Both data sets are plotted in figure 7.4. The direct measurement appears to provide a good estimate of the fineness ratio needed to satisfy the ellipsoidal approximation exactly. The trend of decreasing maximum fineness ratio in each propulsive cycle is similar to observations of *Mitrocoma cellularia* and *Phialidium gregarium* by Colin and Costello (2002).

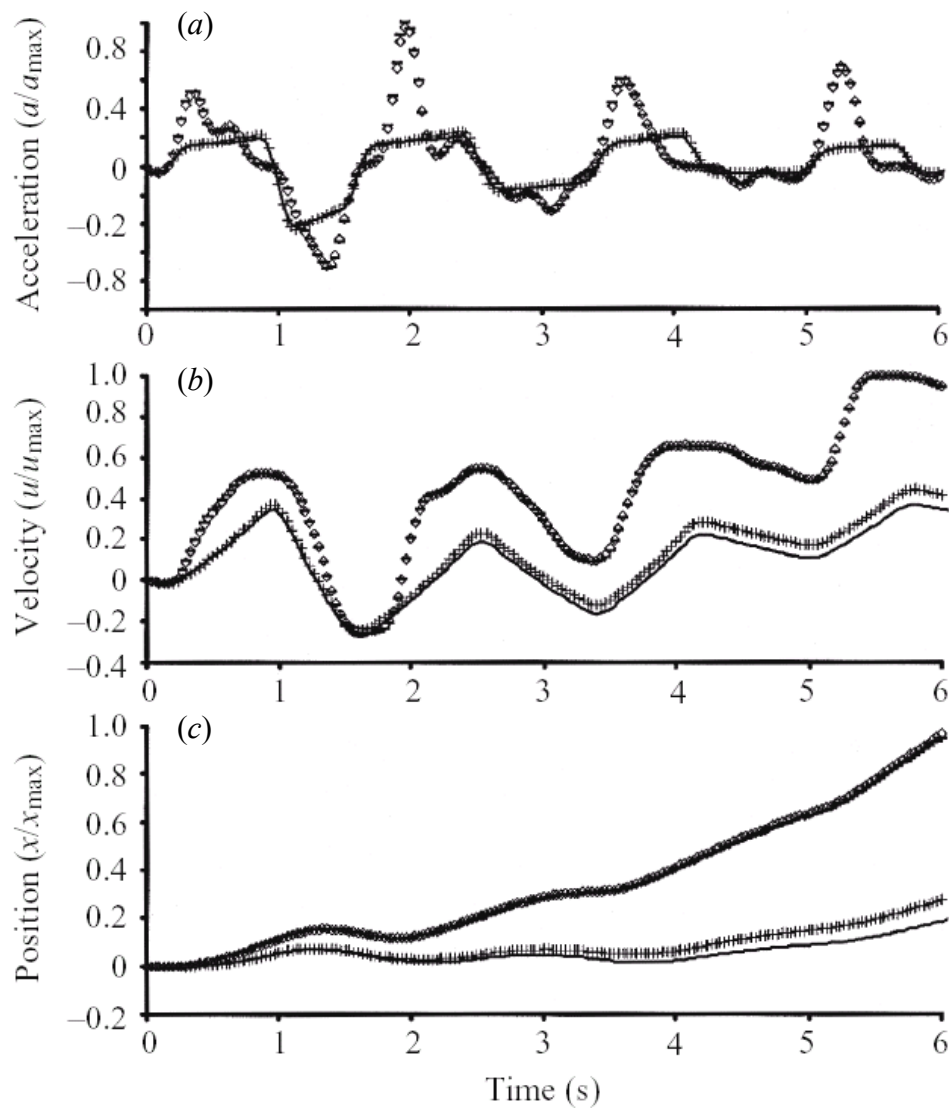


Figure 7.3 Dynamical swimming models for each test case. (a) acceleration versus time, (b) velocity versus time, and (c) position versus time. Horizontal bars, $mVmA$; open diamonds, $mVaA$; solid black line, $aVmA$; +, $aVaA$ (see Table 7.1). Values are normalized by maximum in the plot.

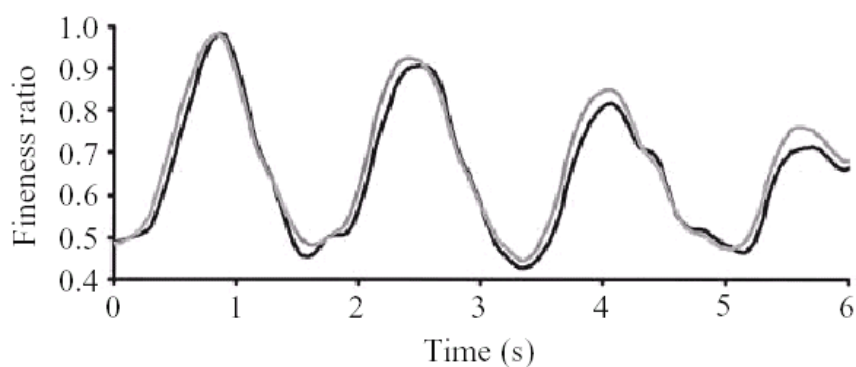


Figure 7.4 Measured and computed fineness ratio. Gray line, direct measurement; black line, values computed from bell volume and aperture measurements using hemiellipsoid approximation.

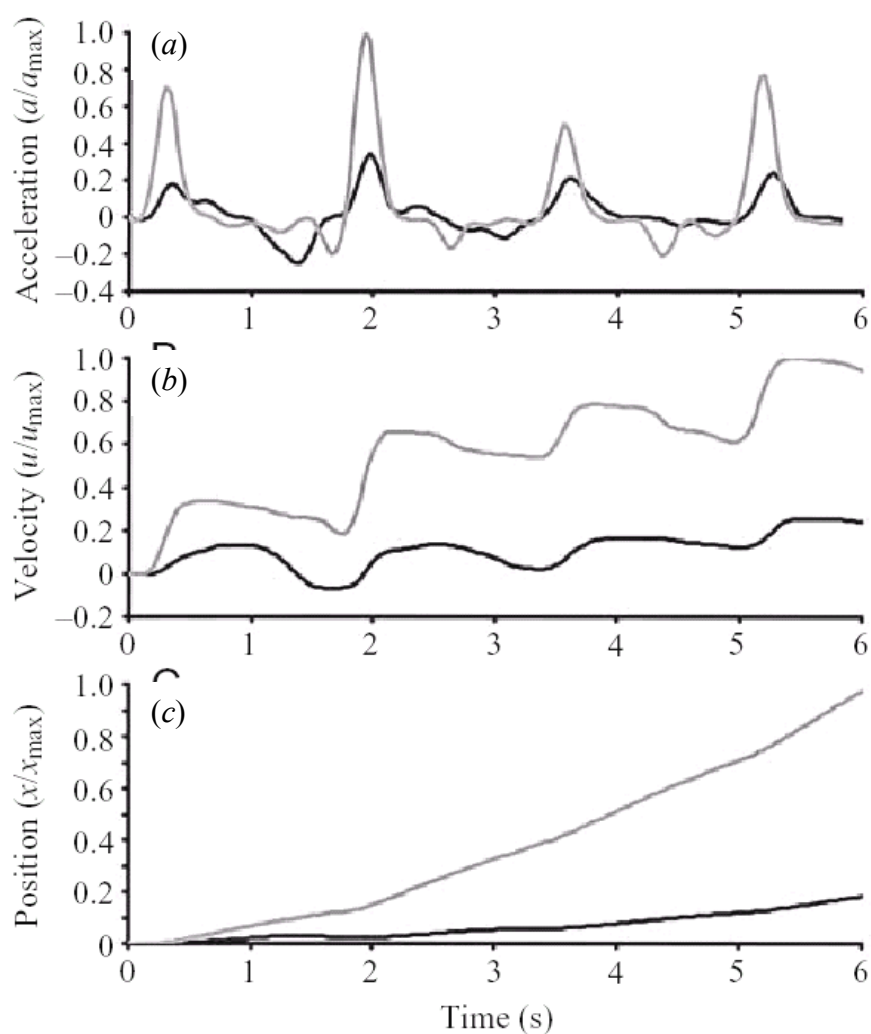


Figure 7.5 Modeled swimming dynamics from fineness ratio measurement inputs. (a) acceleration, (b) velocity, and (c) position. Gray line, fineness ratio result; black line, mV/mA baseline data set. Values are normalized by maximum in the plot.

Using the direct fineness ratio measurement and hemiellipsoid approximation, bell volume and aperture area were computed. This kinematic data was input to the dynamical model to compute swimming motions. They are plotted in figure 7.5 and compared with the baseline data set mV/mA .

The swimming dynamics predicted using the fineness-hemiellipsoid approximation severely overestimate thrust generated by the swimming medusa. Accordingly, the velocity and position of the animal are also highly overestimated. This result is especially striking considering that measured fineness ratios appear to agree well with values computed from the hemiellipsoid approximation.

7.4 Discussion

Two sets of experiments were conducted in this sensitivity analysis to deduce the effects of kinematic approximations on the accuracy of predicted medusan swimming dynamics in a momentum flux model of thrust generation. In both cases, bell volume approximations were observed to agree well with directly measured kinematic inputs to the dynamical model (e.g., figures 7.2a, 7.4). By contrast, the area approximation was rough, both qualitatively and quantitatively (figures 7.2b). Interestingly, the crude area approximation was found to have negligible effect on the accuracy of dynamical model predictions, whereas the model was observed to be strongly dependent on the volume approximation. The constant dV/dt approximation in the first set of experiments and the fineness-hemiellipsoid approximation in the second resulted in severe underestimation and overestimation, respectively, of thrust generation and associated swimming dynamics from the model.

Although this result might be unexpected from an *a priori* qualitative study of the approximations, immediate insight can be gained by examining the quantitative nature of the model in equations (7.2.1) and (7.2.2). Here we see that thrust is dependent on the square of the rate of volume change, but only on the first power of area. The fact that the rate of volume change enters (7.2.1) and not the volume itself suggests that a more appropriate qualitative check would be comparison of the time derivatives of figures 7.2(a) and 7.4. There are substantial differences in this parameter between the measured and approximated volume, especially at the beginning of each contraction and expansion phase.

Errors in the fineness-hemiellipsoid approximation are more complex and depend on geometrical considerations. It is to be expected that this approximation is most accurate when the shape of the medusa bell resembles a hemiellipsoid. Fundamental to the fineness-hemiellipsoid approximation is the assumption that maximum bell diameter occurs at the bell margin. Under these circumstances, the volume and its rate of change can be accurately represented. For *Chrysaora fuscescens*, the bell shape approaches a hemiellipsoid when in its relaxed state. The maximum bell diameter occurs near the bell margin, and the fineness ratio can effectively describe the morphology. However, upon contraction the bell aperture diameter reduces substantially, and the location of maximum bell diameter is midway between the bell margin and apex. The shape can no longer be accurately described as a hemiellipsoid. If the bell aperture diameter is still used to define the fineness ratio, the volume of the medusa is significantly underestimated. The total volume change during each phase of the propulsive cycle is overestimated, as is the time rate of volume change. Such was demonstrated in these experiments. Alternatively, one might attempt to use the maximum bell diameter consistently to define the fineness ratio,

but the volume would then be overestimated upon contraction and the time rate of volume change underestimated.

Using the measured bell volume and aperture area, it is possible to deduce the proper diameter that should be used to compute the fineness ratio *a priori* for an accurate hemiellipsoid approximation. The result is shown in figure 7.6, as the ratio between this reference diameter and the bell aperture diameter. In addition, the maximum value of bell diameter on the entire medusa is plotted at points of maximum contraction and expansion.

The variation in reference diameter relative to the bell aperture diameter is subtle, remaining within 10% of the aperture diameter throughout the series of propulsive cycles. Nonetheless, using the bell aperture in favor of the reference diameter has been shown to result in large errors, demonstrating the strong dependence on this parameter.

Consistent with the above arguments, the maximum bell diameter approaches the bell aperture diameter at points of maximum medusa expansion. By contrast, the maximum bell diameter is much larger than the reference diameter during phases of maximum contraction.

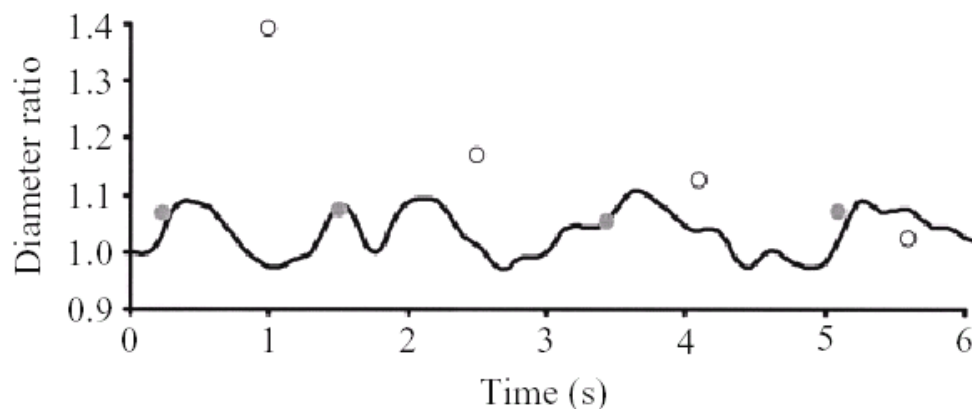


Figure 7.6 Ratio of diameter for exact fineness-hemiellipsoid model to bell aperture diameter. Solid black line, diameter ratio; gray circles, maximum bell diameter at maximum expansion; open circles, maximum bell diameter at maximum contraction.

We are left with the dilemma of properly modeling medusan morphology and swimming in the general case, while maintaining the tractability of the problem. The measurement algorithm created for this sensitivity analysis presents an alternative, although it is cumbersome to implement relative to morphological models using geometrical approximations and a few descriptive parameters. It has been shown here that such models must have as a priority an accurate representation of medusa bell volume effects, especially their temporal variation. A single parameter can be insufficient to provide a robust, accurate description of the animal kinematics. It may be necessary to augment the fineness ratio description with a parameter to capture the effect of large deformations at the bell margin. An effective solution may be to incorporate information regarding the location of maximum bell diameter. This can be accomplished using a truncated-ellipsoid description of the bell, as a more general case of the hemiellipsoid model. Further examination of the relationship between volume transients and hydrodynamic forces may suggest more effective swimming models.

Generally, any dynamic model of locomotion that implements a combination of kinematic assumptions is vulnerable to a combined effect wherein competing errors of underestimation and overestimation may go unnoticed in the final result. In the present study, underestimation of swimming thrust due to the assumption of constant rate of volume change can be compensated by overestimation of thrust in the fineness-hemiellipsoid approximation. Should the two errors effectively cancel one another, one may be led to the spurious conclusion that because the measurements agree with the model, the theory is sufficient. Therefore it is critical in all animal studies of locomotion to isolate

the error associated with each kinematic assumption before implementing them in combination.

An important step has been taken in this sensitivity analysis to isolate the kinematic parameters of greatest importance in medusan swimming and to quantify the sensitivity of the dynamic model to these inputs. More generally, these results urge similar analyses of other animal locomotion models to avoid potentially misleading results that can arise by assuming an *ipso facto* link between kinematic and dynamic similarity.

7.5 Chapter References

- Batchelor, G. K. 1967 *An Introduction to Fluid Dynamics*. Cambridge University Press.
- Colin, S. P. and Costello, J. H. 2002 Morphology, swimming performance, and propulsive mode of six co-occurring hydromedusae. *J. Exp. Biol.* **205**, 427-437.
- Costello, J. H. and Colin, S. P. 1994 Morphology, fluid motion and predation by the scyphomedusa *Aurelia aurita*. *Mar. Biol.* **121**, 327-334.
- Costello, J. H. and Colin, S. P. 1995 Flow and feeding by swimming scyphomedusae. *Mar. Biol.* **124**, 399-406.
- Daniel, T. L. 1983 Mechanics and energetics of medusan jet propulsion. *Can. J. Zool.* **61**, 1406-1420.
- Daniel, T. L. 1985 Cost of locomotion: unsteady medusan swimming. *J. Exp. Biol.* **119**, 149-164.
- DeMont, M. E. and Gosline, J. M. 1988 Mechanics of jet propulsion in the hydromedusan jellyfish, *Polyorchis penicillatus*. I. Mechanical properties of the locomotor structure. *J. Exp. Biol.* **134**, 313-332.

- DeMont, M. E. and Gosline, J. M. 1988 Mechanics of jet propulsion in the hydromedusan jellyfish, *Polyorchis penicillatus*. II. Energetics of the jet cycle. *J. Exp. Biol.* **134**, 333-345.
- DeMont, M. E. and Gosline, J. M. 1988 Mechanics of jet propulsion in the hydromedusan jellyfish, *Polyorchis penicillatus*. III. A natural resonating bell; the presence and importance of a resonant phenomenon in the locomotor structure. *J. Exp. Biol.* **134**, 347-361.
- Denton, E. J. and Shaw, T. I. 1961 The buoyancy of gelatinous marine animals. *Proc. Physiol. Soc.* **161**, 14-15.
- Ford, M. D. and Costello, J. H. 2000 Kinematic comparison of bell contraction by four species of hydromedusae. *Sci. Mar.* **64**, 47-53.
- Ford, M. D., Costello, J. H., Heidelberg, K. B. and Purcell, J. E. 1997 Swimming and feeding by the scyphomedusa *Chrysaora quinquecirrha*. *Mar. Biol.* **129**, 355-362.
- Gladfelter, W. G. 1972 Structure and function of the locomotory system of the scyphomedusa *Cyanea capillata*. *Mar. Biol.* **14**, 150-160.
- Hanselman, D. and Littlefield, B. R. 2000 *Mastering MATLAB 6*. Prentice Hall.
- Webb, P. W. 1982 Fast-start resistance of trout. *J. Exp. Biol.* **96**, 93-106.

CHAPTER 8: The role of optimal vortex formation in biological fluid transport

Submitted to Proceedings of the Royal Society of London B October 14, 2004

8.0 Chapter Abstract

Animal phyla that require macro-scale fluid transport for their function have repeatedly and often independently converged on the use of jet flows. During flow initiation these jets form fluid vortex rings, which facilitate mass transfer by stationary pumps (e.g., cardiac chambers) and momentum transfer by mobile systems (e.g., jet-propelled swimmers). Previous research has shown that vortex rings generated in the laboratory can be optimized for efficiency or thrust, based on the jet length-to-diameter ratio (L/D), with peak performance occurring between $3.5 < L/D < 4.5$. Attempts to determine if biological jets achieve this optimization have been inconclusive, due to the inability to properly account for the diversity of jet kinematics found across animal phyla. We combine laboratory experiments, *in situ* observations, and a framework that reduces the kinematics to a single parameter, in order to show that individual animal kinematics can be tuned in correlation with optimal vortex ring formation. This new approach facilitates comparative biological studies of jet flows across animal phyla irrespective of their specific functions and can be extended to unify theories of optimal jet-based and flapping-based vortex ring formation.

8.1 Introduction

Jet flows in biological systems are typically created by the action of positive displacement pumps, which eject fluid from a source chamber through a nozzle or orifice (Vogel, 1994). The flow regime of the jet can be characterized by the velocity of fluid exiting the chamber (U), the diameter of the jet at the chamber exit (D), and the kinematic viscosity of the fluid (ν). For Reynolds numbers $Re = UD/\nu > 6$, the period of rapid jet acceleration during flow initiation causes the leading portion of the jet to roll into a toroidal fluid mass known as a vortex ring (Cantwell, 1986; see figure 8.1). Laboratory experiments have demonstrated that the leading vortex makes a proportionally larger contribution to mass and momentum transport than an equivalent straight jet of fluid (Krueger and Gharib 2003; Dabiri and Gharib 2004). This fact, along with the discovery that physical processes terminate growth of the leading vortex ring at a jet length-to-diameter ratio between $3.5 < L/D < 4.5$ (Gharib, Rambod and Shariff, 1998; Mohseni and Gharib, 1998), has spurred interest in the possibility that biological systems may optimize vortex formation for effective fluid transport (Gharib et al., 1998; Mohseni, Ran and Colonius, 2001; Linden and Turner, 2001; Krueger and Gharib, 2003; Linden and Turner, 2004; Dabiri and Gharib, 2004).

Inferences drawn from vortex rings generated in the laboratory are limited due to kinematic constraints on the vortex generators. Typically the vortices are created by ejecting fluid through a tube with constant exit diameter (Didden, 1979; Gharib et al., 1998; Krueger and Gharib, 2003; Dabiri and Gharib, 2004). This is in contrast with the complex, time-dependent kinematics of positive displacement pumps found in nature (e.g., Vogel, 1994). In situ measurements of fluid jet length-to-diameter ratio (L/D , hereafter referred to

as the dimensionless “formation time” following Gharib et al., 1998) have suffered from an inability to unambiguously incorporate the observed time-varying exit diameter $D(t)$. Attempts to reduce the observed kinematics using a time-averaged exit diameter (\bar{D}) have been unsuccessful in determining a clear correlation between vortex formation dynamics and animal kinematics (e.g., Bartol, Patterson and Mann 2001; Linden and Turner 2004).

The average jet diameter is by itself an insufficient index of jet kinematics because it lacks critical information regarding temporal trends in the jet exit diameter. As mentioned above, laboratory experiments have pointed to the existence of a critical formation time after which growth of the leading vortex ring ceases, and any additional fluid ejected takes the form of a trailing straight jet (Gharib et al., 1998). Since this vortex-limiting formation time is dictated by the time-history of the jet exit diameter and not its average value, an effective kinematic index must preserve this information. From this we can properly record how jet flow is manipulated by changes in the exit diameter both before and after the vortex-limiting formation time is reached.

The goal of this paper is to combine laboratory experiments, *in situ* observations, and a framework that reduces the kinematics to a single parameter, in order to show that individual animal kinematics can be tuned in correlation with optimal vortex ring formation.

8.2 Methods

8.2.1 Kinematic analysis

A suitable kinematic parameter to describe observed animal motions can be derived by considering an infinitesimal increment in the formation time, $\Delta(L/D)^* \equiv (U(\tau)/D(\tau))\Delta\tau$, where $\Delta\tau$ is a small increment in dimensional time. Here the jet exit velocity and diameter are instantaneous values at time τ . Integrating the formation time increment from flow initiation at $\tau = 0$ to termination at $\tau = t$, we arrive at a parameter for vortex formation that effectively incorporates time-dependent jet kinematics: $(L/D)^* \equiv \overline{U/D} t$. The over-bar again denotes a time average, and t is the duration of fluid ejection.

For the case of a constant jet exit diameter, this new index is identical to the traditional definition. In addition, when the exit velocity and diameter follow the same temporal trend (e.g., both linearly increasing) the new index also gives the same result as the traditional definition. This occurs because the parameter is dimensionless and therefore does not account for overall changes in the scale of the fluid transport mechanism. The benefit of this property of the parameter is that it facilitates comparison between biological systems of differing function, morphology, and scale. Conversely, the parameter is limited in that it does not account for changes in the fluid dynamics due to Reynolds number effects. However Gharib et al. (1998) demonstrated that the process of vortex ring formation is relatively insensitive to the Reynolds number of the flow.

Although the new index also involves a time average, the velocity and diameter data are properly coupled in the calculation. In contrast, previous time-averaging techniques treated the exit velocity and diameter data as independent trends. It is that

decoupling that has led to spurious conclusions regarding the correlation between vortex formation and animal pump kinematics.

8.2.2 Laboratory apparatus

To test this result experimentally, we studied jet flow vortex formation by creating an apparatus that incorporates a controllable variable-diameter exit nozzle on the flow tube of a traditional laboratory vortex generator (figure 8.1, cf. Dabiri and Gharib, 2005). This technique was used to probe the effects of a temporally increasing exit diameter on jet flows as is observed, for example, during tail-first swimming motions of squid (O’Dor, 1988; Anderson and DeMont, 2000; Bartol et al., 2001) and the early refilling phase of ventricular diastole (Verdonck, et al., 1996). Fluid forces were determined from the time-integrated jet thrust, or fluid impulse, $I = \int_V \mathbf{x} \times (\nabla \times \mathbf{u}) dV$. This first moment of vorticity was computed given the position vector (\mathbf{x}) of fluid particles relative to the nozzle exit plane and axis of symmetry, the velocity field (\mathbf{u}) measured using digital particle image velocimetry (Willert and Gharib, 1991), and the measurement volume (V).

8.3 Results

8.3.1 Laboratory results

Importantly, measurements showed that temporal increases in jet exit diameter do not change the vortex-limiting formation time (now computed using $(L/D)^*$) from the constant-diameter value of 4.0 ± 0.5 (cf. Dabiri and Gharib, 2005). This observed robustness of the vortex formation process for the various jet kinematics tested suggests that conclusions regarding the fluid dynamics can be applied beyond the specific kinematics of this experimental apparatus.

Temporal increases in jet exit diameter during formation of the leading vortex ring were found to increase thrust and impulse generated by the apparatus by increasing the moment arm of the generated vorticity flux. This effect is predicted by a thin vortex ring model of the flow (Shariff and Leonard, 1992), in which the impulse can be approximated from the vortex ring circulation (area-integrated vorticity, Γ) and diameter (D_R), as $I = \frac{1}{4}\pi\Gamma D_R^2$. Figure 8.2 indicates that the radial extent D_R of the leading vortex rings increased in proportion to temporal growth of the jet exit diameter.

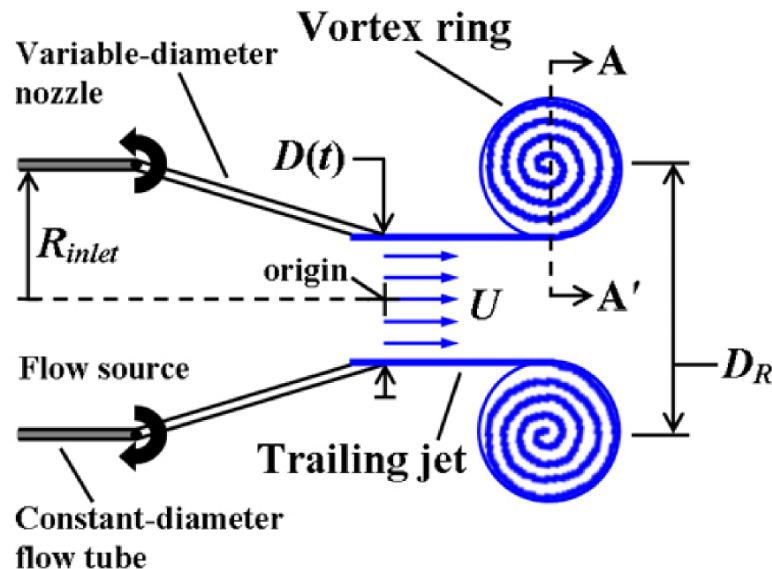


Figure 8.1 Schematic of jet flow apparatus with time-varying nozzle exit diameter.

All components are depicted as they appear in a meridian cross-section of the axisymmetric device. Nozzle actuators are not shown. Jet flow at the exit plane (i.e., through the origin and normal to the symmetry axis) is from left to right. Jet was initiated upstream using a piston-cylinder mechanism (cf. Gharib et al., 1998) that impulsively created a constant volume flux of $8.8 \text{ cm}^3 \text{ s}^{-1}$, with a rise time of 300 ms.

Nozzle exit diameter was varied temporally between 45% and 67% of the inlet diameter, $D_{inlet} = 2.54 \text{ cm}$, in each experiment. Variables indicated in the schematic are referred to in the text.

8.3.2 Biological optimization strategy

These results indicate that biological systems requiring rapid impulse generation during jet initiation will benefit from a strategy of enlarging their orifice or nozzle during early vortex formation. If the animal is capable of ejecting the entire fluid jet with a formation time $(L/D)^*$ approaching 4, it will also benefit from gains in system efficiency (Krueger and Gharib 2003).

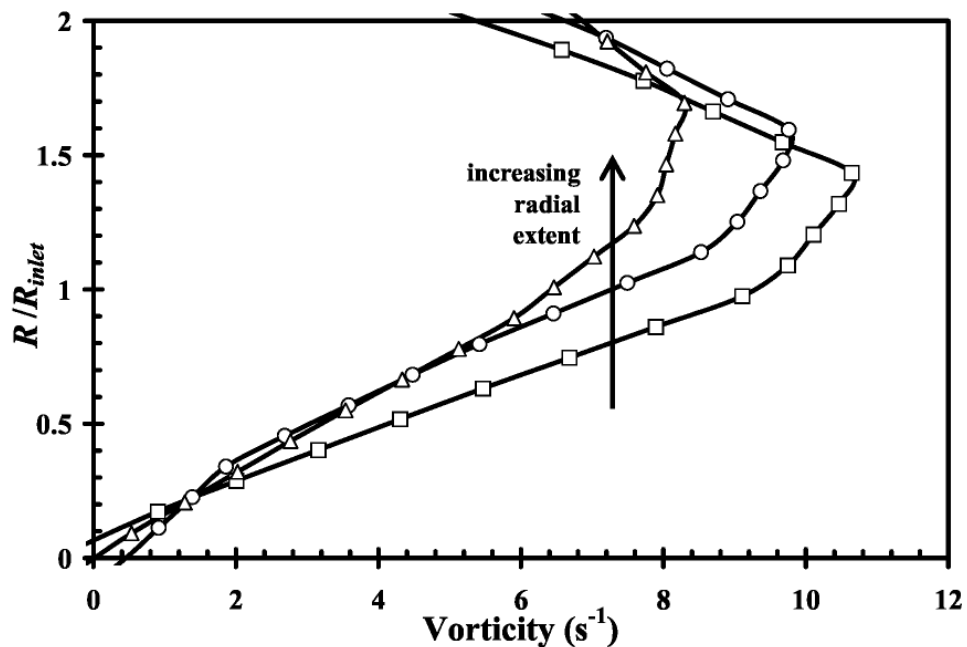


Figure 8.2 Vorticity profiles for different rates of jet exit diameter temporal increase. Radial variable (R) is measured along section A-A' indicated in figure 8.1. Square symbols indicate vorticity profile for constant exit diameter $D = 0.45 D_{inlet}$. Circle symbols indicate increase from $D = 0.45 D_{inlet}$ to $0.67 D_{inlet}$ in 2.2 s. Triangle symbols indicate increase from $D = 0.45 D_{inlet}$ to $0.67 D_{inlet}$ in 1.2 s.

Where efficiency is secondary in importance to absolute thrust or impulse production, it will be useful to extend the duration of fluid ejection beyond the formation time of 4. Here, quasi-steady fluid dynamics can be exploited to further augment the thrust. For a given volume flow rate (\dot{Q}) ejected from the source pump after leading vortex ring

growth has terminated, the exit flow velocity will be inversely proportional to the square of the exit diameter, $U \sim \dot{Q}/D^2$. Since the rate of fluid impulse production is proportional to U^2 , decreasing the exit diameter after growth of the leading vortex ring has ceased will provide substantial gains in momentum transport by the jet flow.

In sum, animals that face selective pressures for efficiency will create flows with jet formation times approaching 4. Conversely, systems that require large thrust production—possibly at the expense of operational efficiency—will increase the exit diameter until a formation time of 4 is achieved, and then subsequently decrease the exit diameter for optimal performance during extended fluid ejection.

8.3.3 Comparison with in situ squid measurements

We confirmed these predictions for two biological systems on opposite ends of the spectrum (functionally speaking) of biological jet flows. In the first case, we considered tail-first swimming of the brief squid *Lolliguncula brevis*. This mode of locomotion is employed by squid for high-speed maneuvers, including their jet-propelled escape mechanism (Gosline and DeMont, 1985; O’Dor, 1988; Anderson and DeMont, 2000; Bartol et al., 2001). A premium is accordingly placed on thrust production during this swimming mode. Following the foregoing discussion, the formation time should be larger than 4, with a transition from temporally increasing squid funnel exit diameter to temporal decrease occurring near the vortex-limiting formation time. Figure 8.3 plots data from published measurements of the time dependent funnel exit diameter during successive swimming cycles (i.e., Bartol et al. 2001) versus jet formation times computed using the methods presented above. When the funnel exit diameter is plotted versus the traditional formation time definition (L/\bar{D}), there is no clear correlation between changes in the

funnel exit diameter and the vortex-limiting formation time (crosses). However, using the parameter $(L/D)^*$ developed here, a sharper transition between initial funnel exit diameter increase and subsequent decrease is observed (closed circles). Furthermore, the transition between the two phases follows the predicted behavior, occurring in the range $3.5 < (L/D)^* < 4.5$.

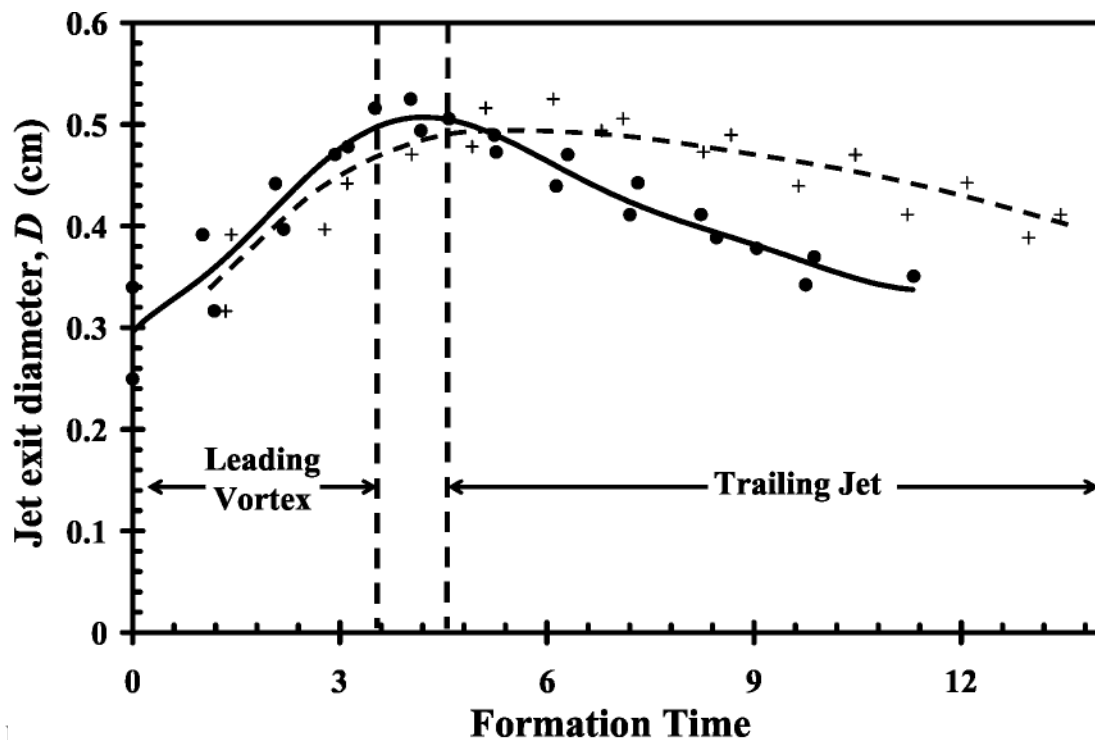


Figure 8.3 Tail-first swimming kinematics of *Lolliguncula brevis*. Jet exit diameter and velocity data from successive swimming cycles were compiled from Bartol et al. 2001. Dashed vertical lines indicate range of vortex-limiting formation time, $3.5 < (L/D)^* < 4.5$. Cross symbols indicate trends computed using L/\bar{D} defined in the text. Circle symbols and solid line indicate trend computed using $(L/D)^*$ defined in the text.

8.3.4 Comparison with in vivo cardiac measurements

As a second example, we examined published data from trans-mitral blood flow during early left ventricle diastolic filling in patients (i.e., Verdonck et al., 1996) measured using M-mode echocardiography (Nishimura et al., 1989). Figure 8.4 plots the mitral valve

exit diameter versus jet formation time $(L/D)^*$ computed for normal and pathological conditions observed in the patients.

During normal function (solid line), the entire jet is ejected in a formation time less than 4, indicating efficient operation. The initial rate of valve opening increases with heart rate (closed circles), providing the augmented fluid impulse required under the systemic stress. When those stresses are exacerbated, as in pathologies such as cardiac ischemia (Gaasch and Zile 2004), a response is observed in the mitral valve kinematics in which the degree of temporal valve opening is increased (closed squares). Again this is in accord with the principles we have outlined whereby such temporal increases in jet diameter provide increased impulse generation. Although this compensatory mechanism can be effective in the short term, further deterioration of the pump mechanism in the form of reduced performance at flow initiation (i.e., reduced E/A wave ratio; Appleton, Hatle and Popp, 1988) can force the system to abandon efficient function for the sake of merely producing sufficient fluid impulse to survive. In these cases, the jet formation time is increased beyond $(L/D)^* \approx 4$ (closed triangles). Similar to the behavior observed in the squid jet flows, the resulting exit diameter kinematics follow our prediction of a temporally increasing exit diameter until the vortex-limiting formation time is reached, followed by temporal decrease thereafter.

Certainly, not all pathologies of left ventricle diastole can exploit these compensatory mechanisms. When the function of the valves themselves is affected as in mitral valve stenosis (Gaasch and Zile 2004), any correlation between valve kinematics and the vortex-limiting formation time is lost (dashed line). However, this observation in itself serves as a useful diagnostic for pathologies that are localized near the jet exit plane.

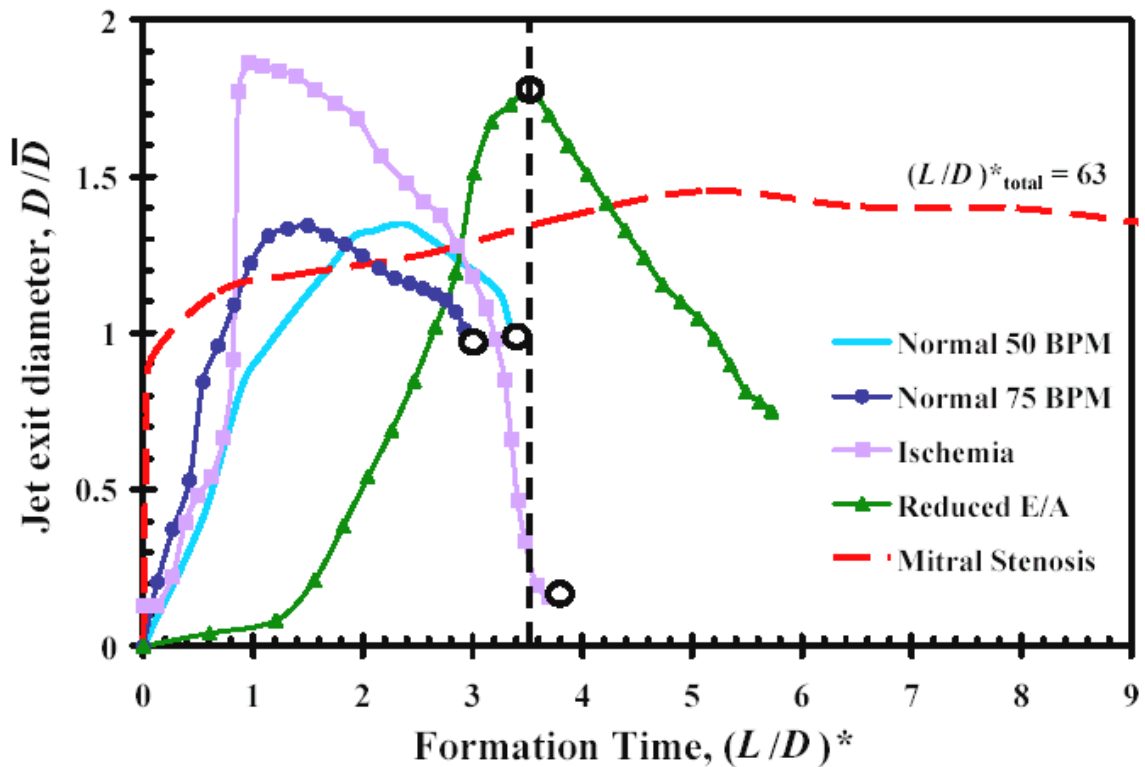


Figure 8.4 Trans-mitral flow during normal and pathological early diastolic filling. Jet exit diameter and velocity data for each patient were compiled from Verdonck et al., 1996. Diameter data are normalized by the time-averaged mitral valve exit diameter in each patient to facilitate quantitative comparison. Dashed vertical line indicates lower bound of vortex-limiting formation time, $(L/D)^* = 3.5$. Open circle symbols indicate points of correlation with optimal vortex formation time.

8.4 Discussion

This work has shown that functionally and morphologically diverse biological fluid transport systems can be designed and tuned in accordance with the dynamics of vortex ring formation. The framework introduced here for studying biological jet flows has the potential to connect functionally disparate systems in comparative studies and to improve our understanding of jet flow pathologies relative to normal function.

We also suggest that the analytical method developed here can be used to develop a connection between the observed robustness of jet-based vortex ring formation in aquatic

propulsion (Linden and Turner 2004) and the previously discovered optimal Strouhal parameter for flapping-based vortex ring formation in insect and bird flight (Taylor, Nudds and Thomas 2003). In an analysis of the latter group, the jet exit diameter of relevance in the present paper will be replaced with considerations for the time-dependent flap morphology and flapping kinematics.

8.5 Chapter References

- Anderson, E. J. and DeMont, M. E. 2000 The mechanics of locomotion in the squid *Loligo pealei*: locomotory function and unsteady hydrodynamics of the jet and intramantle pressure. *J. Exp. Biol.* **203**, 2851-2863.
- Appleton, C. R., Hatle, L. K. and Popp, R. L. 1988 Relation of transmitral flow velocity patterns to left ventricular diastolic function: new insights from a combined hemodynamic and Doppler echocardiographic study. *J. Am. Col. Cardiol.* **12**, 426-440.
- Bartol, I. K., Patterson, M. R. and Mann, R. 2001 Swimming mechanics and behaviour of the shallow-water brief squid *Lolliguncula brevis*. *J. Exp. Biol.* **204**, 3655-3682.
- Cantwell, B. J. 1986 Viscous starting jets. *J. Fluid Mech.* **173**, 159-189.
- Dabiri, J. O. and Gharib, M. 2004 Fluid entrainment by isolated vortex rings. *J. Fluid Mech.* **511**, 311-331.
- Dabiri, J. O. and Gharib, M. 2005 Starting flow through nozzles with temporally variable exit diameter. *J. Fluid Mech.*, in press.
- Didden, N. 1979 Formation of vortex rings—rolling-up and production of circulation. *Z. Angew. Math. Phys.* **30**, 101-116.

- Gaasch, W. H. and Zile, M. R. 2004 Left ventricular diastolic dysfunction and diastolic heart failure. *Annu. Rev. Med.* **55**, 373-394.
- Gharib, M., Rambod, E. and Shariff, K. 1998 A universal time scale for vortex ring formation. *J. Fluid Mech.* **360**, 121-140.
- Gosline, J. M. and DeMont, M. E. 1985 Jet-propelled swimming in squids. *Scient. Am.* **252**, 96-103.
- Krueger, P. S. and Gharib, M. 2003 The significance of vortex ring formation to the thrust and impulse of a starting jet. *Phys. Fluids* **15**, 1271-1281.
- Linden, P. F. and Turner, J. S. 2001 The formation of 'optimal' vortex rings, and the efficiency of propulsion devices. *J. Fluid Mech.* **427**, 61-72.
- Linden, P. F. and Turner, J. S. 2004 'Optimal' vortex rings and aquatic propulsion mechanisms. *P. Roy. Soc. Lond. B* **271**, 647-653.
- Mohseni, K. and Gharib, M. 1998 A model for universal time scale of vortex ring formation. *Phys. Fluids* **10**, 2436-2438.
- Mohseni, K., Ran, H. Y. and Colonius, T. 2001 Numerical experiments on vortex ring formation. *J. Fluid Mech.* **430**, 267-282.
- Nishimura, R. A., Abel, M. D., Hatle, L. K. and Tajik, A. J. 1989 Assessment of diastolic function of the heart: background and current applications of Doppler echocardiography. Part 2: clinical studies. *Mayo Clin. Proc.* **64**, 181-204.
- O'Dor, R. K. 1988 The forces acting on swimming squid. *J. Exp. Biol.* **137**, 421-442.
- Shariff, K. and Leonard, A. 1992 Vortex rings. *Annu. Rev. Fluid Mech.* **24**, 235-279.
- Taylor, G. K., Nudds, R. L. and Thomas, A. L. R. 2003 Flying and swimming animals cruise at a Strouhal number tuned for high power efficiency. *Nature* **425**, 707-711.

- Verdonck, P., Segers, P., Missault, L. and Verhoeven, R. 1996 In vivo validation of a fluid dynamics model of mitral valve M-mode echocardiogram. *Med. Biol. Eng. Comput.* **34**, 192-198.
- Vogel, S. 1994 *Life in Moving Fluids*. Princeton University Press.
- Willert, C. E. and Gharib, M. 1991 Digital particle image velocimetry. *Exp. Fluids* **10**, 181-193.

CHAPTER 9: Flow patterns generated by oblate medusan jellyfish: field measurements and laboratory analyses

Submitted to Journal of Experimental Biology November 12, 2004

9.0 Chapter Abstract

Flow patterns generated by medusan swimmers such as jellyfish are known to differ according to the morphology of the various animal species. Oblate medusae have been previously observed to generate vortex ring structures during the propulsive cycle. Due to the inherent physical coupling between locomotor and feeding structures in these animals, the dynamics of vortex ring formation must be robustly tuned to facilitate effective function of both systems. To understand how this is achieved, we employed dye visualization techniques on swimming scyphomedusae (*Aurelia aurita*) observed swimming in their natural marine habitat. The flow created during each propulsive cycle consists of a toroidal starting vortex formed during the power swimming stroke, followed by a stopping vortex of opposite rotational sense generated during the recovery stroke. These two vortices merge in a laterally-oriented vortex superstructure that induces flow both toward the subumbrellar feeding surfaces and downstream. The lateral vortex motif discovered here appears to be critical to the dual function of the medusa bell as a flow source for feeding and propulsion. Furthermore, vortices in the animal wake exhibit greater volume and closer spacing than predicted by prevailing models of medusan swimming. These effects are shown to be advantageous for feeding and swimming performance and are an important consequence of vortex interactions that have been previously neglected.

9.1 Introduction

Medusan swimmers propel themselves forward via periodic bell contractions that act to decrease the volume of their subumbrellar cavity and jet water out of the oral end of their bell. Described as jet propulsion, prevailing models of this process focus on the fluid efflux that emerges during bell contraction: a toroidal volume of rotating fluid known as the power stroke starting vortex ring (figure 9.1).

Any vortex formation that may occur during the recovery stroke of the propulsive cycle is neglected in existing models of the swimming process (e.g., Daniel, 1983; Colin and Costello, 2002; McHenry and Jed, 2003). Therefore interactions between adjacent vortex rings in the wake have been previously examined based on the assumption of a uniform train of starting vortex rings in the animal wake, each with identical rotational sense.

Weihhs (1977) uses a quasi-steady model of such a vortex ring train to conclude that substantial thrust augmentation can occur—up to 150% relative to a steady jet—if the vortex rings are spaced sufficiently close together (i.e., $C/(B+D)$ is small; see figure 9.1). The thrust benefit arises due to the induced downstream velocity of the vortex ring train on each of its members. Interestingly, the flow pattern depicted by Ford et al. (figure 5, 1997) for the oblate jellyfish *Chrysaora quinquecirrha* shows a train of closely spaced vortex rings.

The proximity of the wake vortex rings to each other and to the swimming animal as measured by Ford et al. (1997) is unexpected given the tendency of individual vortex rings to rapidly propagate away from the flow source due to self-induced velocity (Lamb, 1932) and convection by any jet-like flow that is present behind each ring. An estimate by

Daniel (1983) of the medusan wake vortex ring train using these assumptions predicts a spacing of 10 vortex ring radii between adjacent rings. This result agrees with a physical intuition for the formation of successive vortex rings with identical rotational sense, but is incompatible with the experimental measurements of Ford et al. (1997).

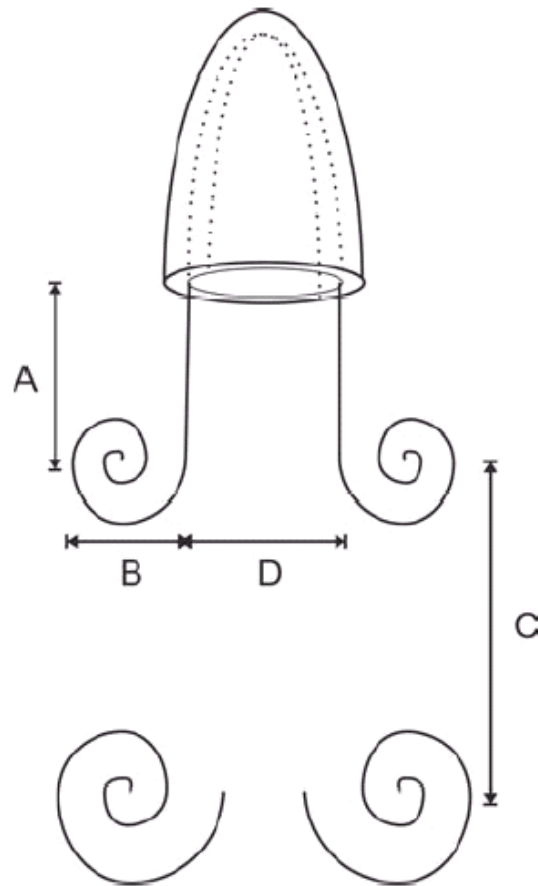


Figure 9.1 Schematic of a jetting medusa with vortex rings in the wake. Vortex rings shown in cross-section. *A*, jet length; *B*, vortex ring thickness; *C*, vortex ring spacing; *D*, jet diameter.

Given difficulties in quantitatively measuring vortex ring properties using particle tracking methods, one cannot make *a priori* preference for either the measurements of Ford et al. (1997) or the model estimate of Daniel (1983). An experimental reexamination of both the measured flow patterns of Ford et al. (1997) and the assumptions leading to the

model of Daniel (1983) is necessary to clarify this issue. The importance of this effort is underscored by the heavy reliance on both the model of Daniel (1983) and observations of power stroke vortex ring formation to develop generalized dynamical models of medusan swimming (e.g., Colin and Costello 2002; McHenry and Jed 2003).

Of further concern is the fact that existing models of medusan behavior make little association between swimming and the prey capture mechanisms required for feeding. Yet, a clear relationship between swimming and feeding has been documented for a variety of medusae, notably larger oblate forms (Costello and Colin, 1994, 1995).

Due to the inherent physical coupling between the locomotor and feeding structures in medusae, it is important to investigate how the generated flow patterns can efficiently meet the demands of both systems. Fluid motions must be heavily utilized in the process of capturing prey and transporting it to feeding surfaces, while maintaining a capability to generate thrust for swimming. The physical mechanisms whereby the observed vortex ring structures accomplish both tasks are currently unknown.

The objective of this chapter is to elucidate the nature and utility of flow structures generated by oblate swimming medusae. In order to understand how flow contributes to both thrust production and feeding mechanisms, we utilized *in situ* flow visualization to qualitatively and quantitatively examine flow patterns surrounding the oblate scyphomedusa *Aurelia aurita*.

Specifically, we observed the motion of fluorescent dye markers injected at several locations around the bells of *A. aurita* swimming *in situ*. These *in situ* observations eliminate the need for an imposed flow current, as is necessary in typical laboratory tanks that house medusae (i.e., kreisel facilities). The swimming kinematics and dynamics

measured by this method should be more relevant to animal behavior in the marine water column than compared to those achieved by any type of laboratory tank. Further, the use of a continuous dye marker instead of discrete prey for particle tracking simplifies the identification of large-scale fluid structures in the flow, such as vortex rings. In addition, the three dimensional nature of the flow (in the absence of significant vortex stretching) does not limit the effectiveness of the dye marker technique, as is the case with particle tracking. By observing vortex dynamics in the wake and fluid-structure interactions near the medusa bell, the role of the observed flow structures is clarified.

9.2 Methods

9.2.1 Video measurements

Field data were collected from a marine lake (145 hectares, maximum depth 46 m) on the island of Mljet, Croatia, located in the Adriatic Sea (Lat: 42.75° N Long: 17.55° E) during July 2003. All of the video was taken in shallow water (< 20 m) by SCUBA using natural light. Video recordings followed the methods of Costello et al. (1998), whereby medusae were videotaped on miniDV videotape using a Sony DCR VX2000 camera with a zoom lens contained within an Amphibico underwater housing. A second diver injected 20 μ l pulses of concentrated fluorescein dye into the fluid at specific locations around the medusae. This second diver was located to the side of the medusae at 90° to the orientation of the video camera. Both divers took care to avoid disturbing the fluid around the medusa being video taped. The dye made any disturbances by the divers obvious allowing these shots to be excluded from the video analysis. The length of the pipette used to administer the dye (approximately 4 cm) was used as a calibrating size scale in later analysis.

Several hours of video were recorded in which medusae were observed swimming both in large groups and in isolation. The swimming kinematics were qualitatively consistent throughout the observations using the dye technique. In order to achieve more quantitative results, a subset of the full video database was analyzed in greater detail.

9.2.2 Kinematic analyses

Select recordings of animal swimming in the field were collected for further laboratory analysis. For kinematic analyses, sequences of recorded swimming motions in two medusae were chosen according to visibility of the medusa subumbrellar surface, motion in planes parallel to the camera, separation from other medusae, and sufficient dye marker in the flow. In addition, the upper and lower limits of animal size were sought to facilitate comparisons of fluid dynamic and geometric scaling. The larger medusa in the kinematic analyses is an order of magnitude larger than the smaller medusa (10.2-cm maximum bell diameter versus 3.6-cm maximum bell diameter, or 22 times larger by volume).

Video recordings of up to 5 successive swimming contractions in each animal were analyzed using the algorithm of Dabiri and Gharib (2003). Between 10 and 20 control points along the subumbrellar surface of each medusa were tracked during swimming motions to generate a computational reconstruction of the medusae kinematics. The entire subumbrellar surface was clearly visible through the transparent mesoglea in each of the selected frames, and any fluorescent dye carried inside the medusa bell further improved the resolution of the interface location.

In addition to measuring the shape of the bell, the properties of the formed vortex rings were analyzed. Specifically, the volume of each vortex ring and the inter-ring spacing of the vortex ring train in the animal wake were measured. The physical extent of each vortex ring was measured based on the distribution of the dye marker in the flow.

The kinematic analyses include only frames in which the animals are swimming parallel to the image plane of the camera. Hence, the orientation of the vortex rings can be assumed to be such that the ring axis is also parallel to the image plane. To calculate the volume of the visible toroidal vortex rings, we therefore require only measurements of the diameter across the toroid ($B+D$ in figure 9.1) and the diameter of the vortex core (B in figure 9.1).

Important caveats associated with this measurement technique are discussed in the following section. Each set of measurements is presented conservatively, with an uncertainty calculated as the maximum difference between any individual measurement and the average of the set. This metric is used in lieu of the standard deviation, since the standard deviation tends to underestimate the data spread for relatively small sample sizes such as those studied here (Freeman et al., 1998).

9.2.3 Strategies for dye marker interpretation

Despite the convenience of a passive dye marker for qualitative flow visualization, there are important limitations to the technique. First, although all of the dye labels fluid, not all of the fluid is labeled by dye. Therefore if one desires to track the evolution of a fluid structure such as a vortex ring using the passive dye marker, the visible labeled structure may be smaller than the actual fluid structure. When identifying vortex rings in the flow, the dye-labeled ring represents a lower bound on the size of the vortex.

Secondly, the diffusion coefficient of dye markers such as that used in these experiments (fluorescence) is substantially less than the diffusion coefficient of fluid vorticity (i.e., rotation and shear), as measured by the kinematic viscosity of water ($\sim 10^{-2} \text{ cm}^2\text{s}^{-1}$). Hence, regions of compact vorticity such as the wake vortex rings will tend to spread by diffusion at a rate faster than can be observed in the dye. Again, the result is that the visibly labeled structure may be smaller than the actual fluid structure. Consequently, all of our estimates of vortex ring volume are conservative values.

Our strategy is to exploit these limitations by assuming that the measurements represent a lower bound on the size of the vortex rings. The effects of a departure from the lower bound case can be inferred from the available data.

9.3 Results

9.3.1 Vortex formation process

The swimming cycle of *Aurelia aurita* consists of a bell contraction phase (i.e., power stroke) and a bell relaxation phase (i.e., recovery stroke). Observations of fluorescent dye that was injected into the fluid outside the bell along the bell margin of swimming *A. aurita* revealed that the two phases of the swimming cycle interacted with the surrounding fluid to form distinct vortex rings at separate locations relative to the bell.

During the power stroke the bell contracted and initiated the formation of a starting vortex ring. The starting vortex ring induced a motion of fluid originating from regions both inside the subumbrellar volume and outside the bell via entrainment of ambient fluid. The direction of induced motion was oriented at an angle away from the bell margin and

toward both the central axis of the bell and downstream (figure 9.2). At maximum contraction the starting vortex was fully developed and traveling away from the medusa.

As the bell relaxed, a stopping vortex was formed inside the subumbrellar cavity. The stopping vortex induced a motion of fluid originating from outside the bell and toward the subumbrellar cavity. Consequently, as the subumbrellar volume increased with bell relaxation, the stopping vortex served to refill the subumbrellar volume with fluid from outside the bell.

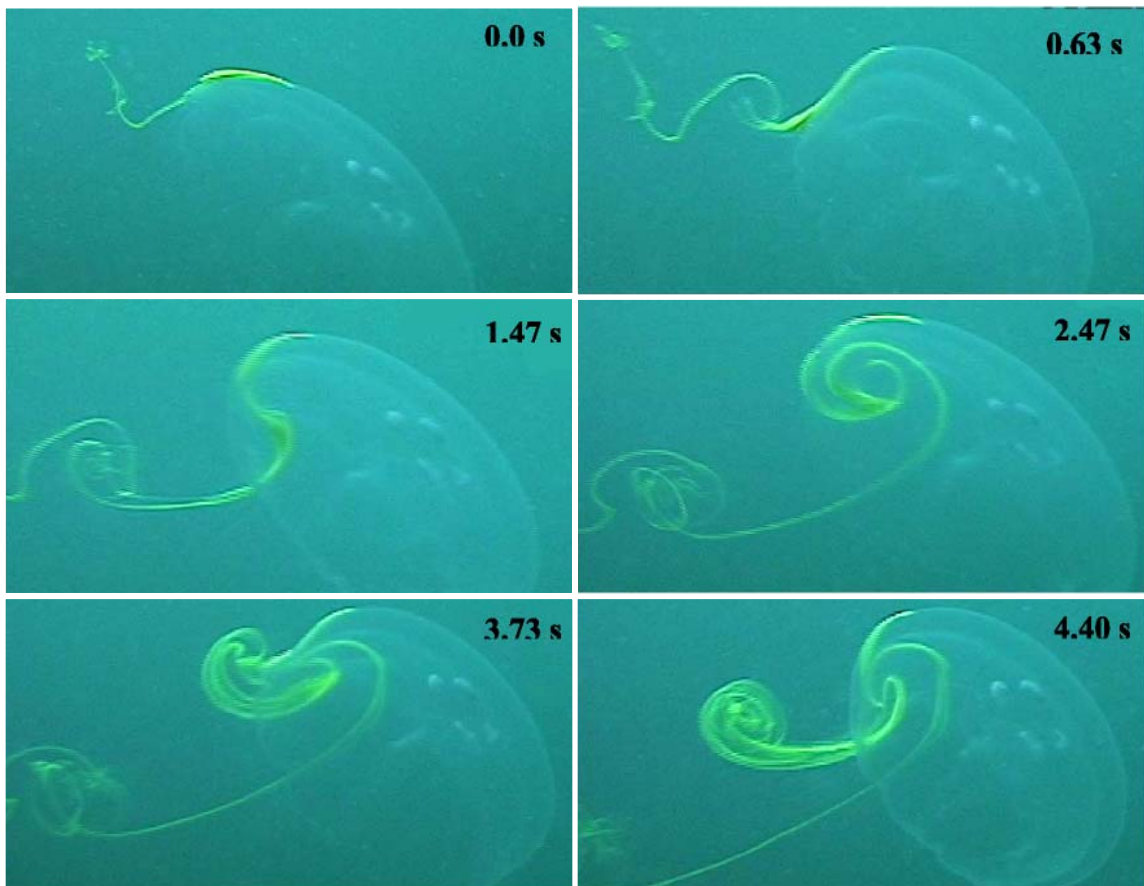


Figure 9.2 Video sequence of vortex ring formation during two swimming cycles of *Aurelia aurita*. At 0.0 and 2.47 seconds the bell is relaxed and fully expanded. Frames at 0.63 and 3.73 seconds show the contraction phase and the formation of the starting vortex. Frames at 1.47 and 4.40 seconds show the relaxation phase, the trailing starting vortex, and the formation of the stopping vortex. The frame at 2.47 shows a fully developed stopping vortex in the subumbrellar cavity.

The stopping vortex remained in the subumbrellar cavity during the beginning of the contraction phase of the next swimming cycle. As the bell contracted, a part of the stopping vortex ring was ejected out from the subumbrellar cavity and interacted with the starting vortex of the new cycle. In the interaction, a portion of the fluid from the stopping vortex co-joined with the starting vortex ring, completing formation of the downstream lateral vortex superstructure. The kinematics of the starting, stopping, and co-joined lateral vortex structure are illustrated in figure 9.3.

Although the schematic in figure 9.3(b) suggests a clear distinction between power and recovery stroke vortices in the wake, the two components actually become highly amalgamated due to fluid mixing. This process makes the individual vortices increasingly difficult to distinguish as the wake develops.

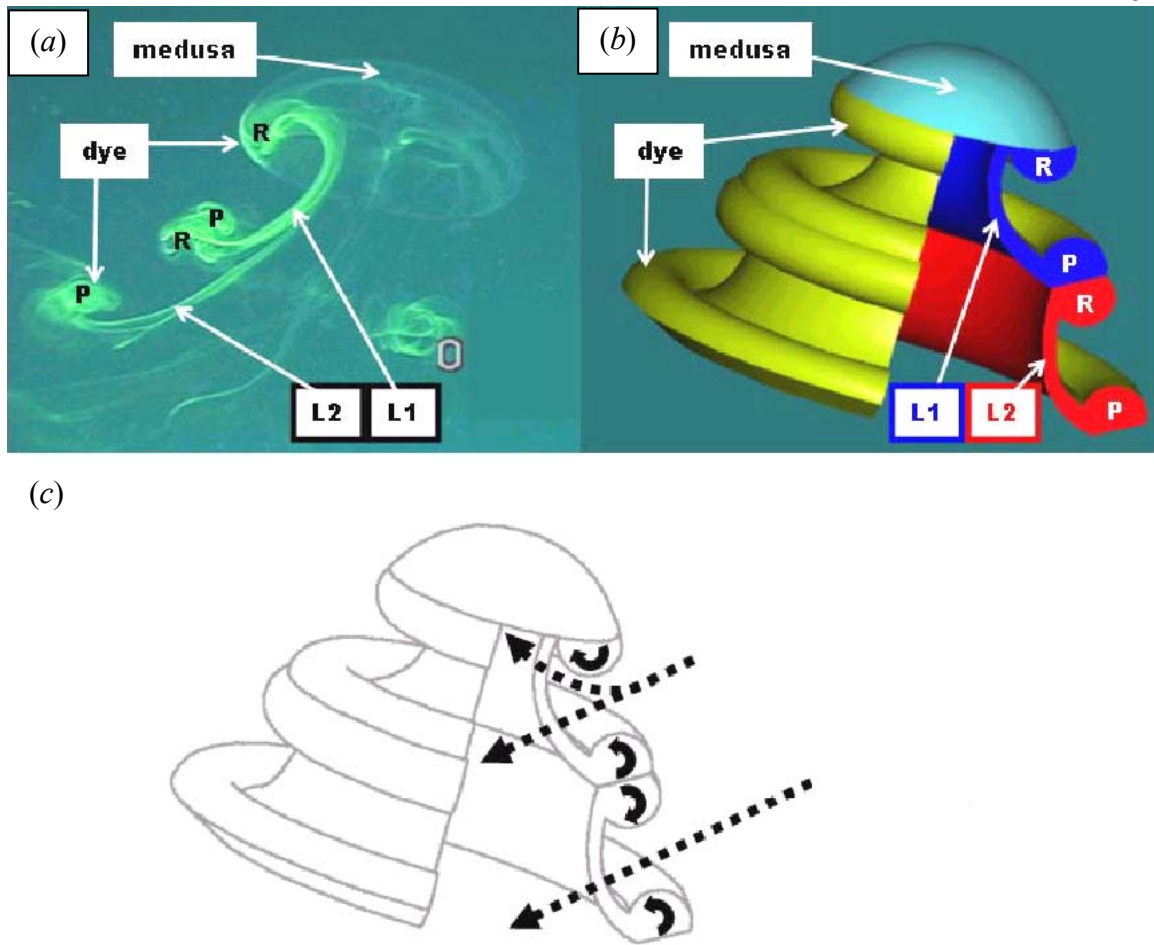


Figure 9.3 Kinematics of the starting, stopping, and co-joined lateral vortex structures. (a) Image of medusa vortex wake. (b) Corresponding schematic of medusa vortex wake. P, power stroke starting vortex ring; R, recovery stroke stopping vortex ring; L1/L2, adjacent lateral vortex superstructures. (c) Flow paths in vortex wake. Solid arrows indicate directions of vortex rotation. Dashed arrows indicate flow induced by vortex rotation.

There are several important observations to be made from the qualitative analysis of the formation and interaction of the starting and stopping vortex rings during swimming cycles. First, throughout the swim cycle, from the onset of the contraction phase through the relaxation phase, there is a continual flow of water from outside the bell, adjacent to the bell margin. During the contraction, the flow contributes to the fluid in the starting vortex ring, but during bell relaxation it contributes to the fluid in the stopping vortex ring.

Second, during a sequence of propulsive cycles we observed that the stopping vortex ring from the preceding lateral vortex structure persists in the bell and contributes to the formation of the subsequent starting vortex (figure 9.2). A complex interaction occurs as the starting vortex ring grows and the previous stopping vortex is convected downstream away from the bell margin. The interaction appears to increase the volume but decrease the velocity of the starting vortex ring, via cancellation of starting vortex vorticity by the preceding stopping vortex ring of opposite rotational sense (cf. Lim and Nickels, 1995). As a result of this interaction, the vortex ring volume and vortex ring spacing of swimming oblate medusae do not relate to thrust in the manner predicted for a unidirectional pulsed jet of fluid through an orifice (i.e., Table 9.1). Existing models for the time-dependent thrust neglect recovery stroke vortex formation altogether and therefore do not apply to these medusae.

The interaction between starting and stopping vortices described above tends to increase the total momentum of each wake vortex. This is because the mass of each wake vortex increases (i.e., the starting and stopping vortex masses combine in the wake) to a greater degree than the wake vortex velocity decreases via vorticity cancellation. The effect of vorticity cancellation is limited because it is a viscosity-dependent process that occurs only at the interface between the starting and stopping vortices (Shariff and Leonard, 1992).

Dye injected into the middle of the subumbrellar volume is not ejected directly outwards during bell contraction but instead spreads laterally along the subumbrellar surface of the bell. All of the dye leaves the subumbrellar cavity at the bell margin. However, it takes the medusa several swim cycles to eject all of the dye from the

subumbrellar region. No fluid is ever directly ejected from the central subumbrellar region. In fact, there is always a net flow into the subumbrellar cavity in the central portion trailing to the bell. This is due to the direction of rotation of the stopping vortex ring in this region (figure 9.3).

9.3.2 *Tentacle positioning*

Throughout the pulsation cycle the tentacles of *A. aurita* were primarily located in vortex rings (figure 9.4). At the beginning of the contraction phase they were in the subumbrellar cavity in the stopping vortex ring. As the bell contracted the tentacles became entrained in the starting vortex ring, which oriented the tentacles in a trailing position. At the end of the contraction phase and the onset of the relaxation phase, the tentacles became entrained in the stopping vortex ring, which drew them back up into the subumbrellar cavity.

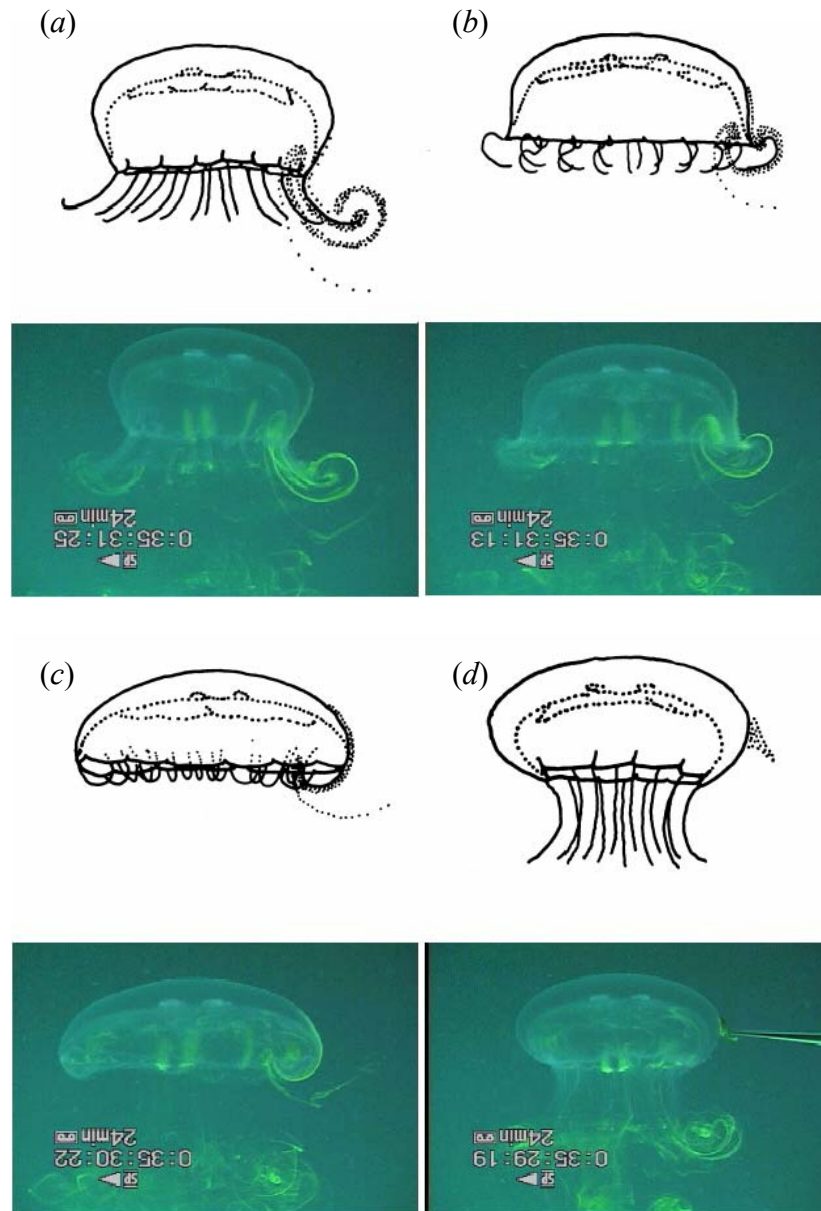


Figure 9.4 Video sequence and schematic of fluorescent dye relative to the tentacles of *Aurelia aurita* during a swimming cycle. Sequence is ordered from (d) to (a).

9.3.3 Vortex ring kinematic measurements

Several important aspects of the fully formed wake vortices were investigated quantitatively. Wake vortices visualized with dye markers allow for quantitative evaluation

of thrust production mechanisms. In this regard, an important variable is the volume of each wake vortex ring relative to the volume of fluid ejected by the medusa. Although the results of the preceding section suggest a more complex relationship between swimming thrust and vortex kinematics than has been previously appreciated, we can anticipate that, for a fixed swimming frequency (and corresponding characteristic flow velocity), swimming thrust will maintain a direct relationship with vortex volume (cf. Daniel, 1983). We cannot neglect the fact that the characteristic flow velocity is reduced by vorticity cancellation between the starting and stopping vortices. However, as mentioned previously, this effect is limited in the present case. Therefore, volume measurements provide the most useful index of swimming thrust in the present study.

The volume contained by the bell at full contraction and relaxation was measured using the subumbrellar surface profiles obtained from the video analysis. The difference between these two values gives the volume of fluid ejected. The ratio of wake vortex ring volume, Ω_w , to ejected fluid volume, Ω_b , was relatively insensitive to animal size: 3.09 ± 0.35 for the smaller animal, and 3.57 ± 0.40 for the larger. Two primary effects contribute to the large volume of the wake vortex rings relative to the volume of fluid ejected. First of these is the presence of the stopping vortex ring, which is created from fluid external to the bell. This stopping vortex is complexed with the starting vortex ring of the subsequent lateral vortex to create each wake vortex ring. Secondly, both starting and stopping vortex ring formation processes involve substantial entrainment of ambient fluid from outside the bell.

Given the vortex ring kinematic measurements, we can also determine the interring spacing in the wake vortex ring train. In both the larger and smaller medusa, the wake

vortex rings are very closely spaced. The inter-ring spacing is 1.36 ± 0.08 ring radii in the smaller medusa and 1.06 ± 0.06 ring radii in the large medusa.

9.4 Discussion

9.4.1 Implications for medusan swimming behavior

Dye studies of the swimming oblate medusa, *Aurelia aurita*, demonstrated the formation of two vortex rings during each bell pulsation cycle. As expected, we observed the formation of a starting vortex ring during bell contraction but, unexpectedly, we observed the formation of a stopping vortex ring during bell relaxation and an interaction of these two vortices to form a lateral vortex superstructure in the wake of the medusa. The discovery of co-joined starting-stopping vortex ring structures in these oblate medusan wakes requires modification of prevailing jet-propulsion models that assume medusan wakes to consist of a simple train of discrete single-sign vortex rings.

The observation of stopping vortex ring formation is not entirely new. It is well known from experiments on vortex ring formation by mechanical apparatus that such structures appear at the end of fluid ejection—hence their title (e.g., Didden, 1979). The source of vorticity for these structures is the interaction between flow external to the vortex ring generator and its outer surface. In a swimming medusa, this corresponds to the interaction of external fluid with the expanding bell margin. The strength of the stopping vortex ring will be directly proportional to the velocity of external fluid past the bell (Didden, 1979) and is therefore coupled to the swimming speed of the animal and the local kinematics of the bell margin.

The presence of such a pronounced stopping vortex ring has profound consequences on thrust production and estimates of thrust. As mentioned, it substantially increases the volume of fluid in each wake vortex ring, Ω_w , relative to the volume of fluid from inside the bell Ω_b . For laboratory-generated vortex rings in the absence of background flow, Dabiri and Gharib (2004a) found that approximately 1/3 of the vortex ring volume originates from ambient fluid external to the jet flow. If we assume that the medusa stopping vortex ring is approximately the same size as the starting vortex ring (a reasonable assumption based on the dye visualizations), then a 1/3 entrained fluid fraction in each starting and stopping vortex ring will lead to a ratio of wake vortex ring volume to ejected fluid volume equal to 3, i.e.,

$$\frac{\Omega_w}{\Omega_b} = \frac{\Omega_{start} + \Omega_{stop}}{\Omega_b} = \frac{\frac{3}{2}\Omega_b + \frac{3}{2}\Omega_b}{\Omega_b} = 3. \quad (9.4.1)$$

Comparing this value with the present measurements, it appears the two effects that we have identified to contribute to the relatively large wake vortex ring volume are sufficient to explain the observations. It is prudent to note that the starting and stopping vortex volumes are indeed additive in equation (9.4.1), despite the fact that the vortices possess opposite rotational sense. This is because the volume of each individual vortex is conserved despite the dynamical influences of vorticity cancellation and induced velocity effects (Lim and Nickels, 1995).

Since the swimming thrust increases directly with wake vortex volume (for a fixed swimming frequency and characteristic flow velocity), the presence of a stopping vortex ring has the potential to greatly increase thrust. Based on the present measurements, the swimming thrust from the co-joined wake vortex ring motif would be larger than a steady

jet of bell fluid by more than a factor of 3. However, the estimated thrust advantage would likely be mitigated in practice by a lower convective velocity for the wake vortex rings relative to a steady jet flow, due to vorticity cancellation effects presented earlier.

The starting-stopping vortex interactions could also potentially increase swimming thrust via the velocity field that the opposite-sign vortices induce on one another, in a manner similar to the effect experienced by vortices near solid surfaces (i.e., ground effect, Rayner and Thomas, 1991; Shariff and Leonard, 1992). Quantitative visualization techniques will be necessary to validate the existence of such an effect in these animals.

The swimming efficiency is difficult to define for these animals because the flow is highly unsteady, and there is no clear protocol for including the relaxation phase in such a calculation. However, we can anticipate an increase in swimming efficiency, given that a Froude-type calculation predicts higher efficiencies for cases in which fluid is transported in high volume and at low velocity, as is observed here (Vogel, 1994).

These findings demonstrate that the effect of the complex vortex ring wake structure must be considered in any realistic model of oblate medusan swimming. Specifically, it is insufficient to estimate thrust production by swimming oblate medusae using measurements of bell kinematics (e.g., Colin and Costello 2002; McHenry and Jed 2003) without a wake vortex ring analysis since the stopping vortex is fully-formed from the beginning of the bell motion. Also, the fluid inside the bell is not at rest (with respect to the medusa) when bell contraction is initiated, as must be assumed in a paddle model of bell kinematics (e.g., McHenry and Jed 2003).

In addition to the relationship between vortex volume and thrust, the relation between inter-vortex ring spacing and thrust may also differ from established models of jet

propulsion. Similar to the observations of Ford et al. (1997), we observed reduced downstream propagation of wake vortices and, hence, a very close spacing between adjacent wake vortex rings. The flow visualization methods employed here enable us to resolve the apparent conflict between measurements and physical intuition for the dynamics of individual vortex rings. Reduced downstream propagation of the wake vortices is the result of vorticity cancellation. For rapid self-induced motion of vortex rings from a flow source it is fundamental that the vortex rings possess a single sign of rotation (Lamb, 1932). In the event that opposite-sign rotation is present, vorticity cancellation will occur in the vortex ring structure, resulting in a vortex ring with weaker self-induced motion. Oblate medusae encounter vorticity cancellation by two means as the flow pattern is being generated. First, the motion of each starting vortex toward the bell axis of symmetry leads to vorticity cancellation with mirror-image portions of the vortex on the opposite side of the bell margin. This effect is enhanced by motion of the bell margin toward the axis of symmetry during bell contraction. This type of vorticity cancellation commences almost immediately after bell contraction is initiated.

Secondly, as previously mentioned, the stopping vortex of the preceding lateral vortex structure interacts with each newly forming starting vortex ring. This additional vorticity cancellation occurs in proportion to the strength of the stopping vortex. Vorticity cancellation by this means can occur almost immediately after bell contraction due to the close proximity of the vortex structures carrying opposite-signed vorticity. The combined result of these processes is reduced downstream propagation of wake vortices and, hence, a very close spacing between adjacent wake vortex rings.

Although it is tempting to further suggest that the thrust benefits due to close inter-ring spacing predicted by Weihs (1977) may be applicable to the dynamics of these medusae, one must remember that the derivation of Weihs (1977) assumes a train of single-sign vortex rings. Whether or not a similar benefit could be derived for the co-joined wake vortex rings studied here is a question still to be resolved.

9.4.2 Implications for medusan feeding behavior

Vortex formation and the use of accompanying induced flows are fundamentally important to feeding by swimming *Aurelia aurita*. Medusae that feed as cruising predators, such as *A. aurita*, are highly dependent on locally generated flow currents to capture prey (Costello and Colin, 1994, 1995; Sullivan et al., 1994; Ford et al., 1997). For these animals, it is beneficial to generate flow regimes that increase encounter rates with prey. The stopping and starting vortex rings and the lateral vortex superstructure generated by *A. aurita* during swimming serve this role. First, both the starting and the stopping vortices entrain fluid from outside the bell throughout the pulsation cycle. This fluid is drawn past the bell margin toward the tentacles, which are positioned in the starting vortex during bell contraction and the stopping vortex during bell relaxation (figure 9.4). Since the starting and stopping vortex rings entrain fluid during both the bell contraction and relaxation, respectively, *A. aurita* is able to use the full pulsation cycle for prey capture. Second, as discussed, the two vortex rings interact enabling the starting vortex ring to entrain a greater volume of fluid than could be entrained by simplified jet flow. Therefore, medusae that generate starting and stopping vortices during swimming are able to process a large volume of water with each pulse. Finally, the prey entrained by the swimming medusae propagates away from the bell at a reduced rate due to the rotational flow of the wake vortex rings.

These observed structures differ considerably from the jet-propulsion flow model (figure 9.1) in which the flow structures take the form of a uniform slug with minimal fluid entrainment. Consequently, the flow structures of swimming oblate medusae, such as *A. aurita*, have the potential to greatly increase encounter rates with prey relative to the flow structures of jet-propulsion.

The reduction in wake vortex ring propagation away from the bell can be amplified at higher swimming speeds because the strength of the stopping vortex (used for vorticity cancellation) possesses direct proportionality to the fluid velocity past the bell (cf. Didden, 1979). The combined effect is a feeding mechanism that uses both bell contraction and relaxation productively for prey capture while being passively tuned for a range of swimming speeds. These flows provide potentially powerful mechanisms for prey encounter with the medusae.

The present dye visualization methods are insufficient to conclusively validate the existence of the passive fluid dynamic tuning mechanisms hypothesized here. However, future work using methods of quantitative velocimetry (e.g., digital particle image velocimetry, Willert and Gharib, 1991) will enable the direct measurements of starting and stopping vortex strength that are necessary to solidify these conclusions.

9.4.3 Implications for prolate medusae

Colin and Costello (2002) suggested that oblate and prolate medusae differ in their dependence on jet propulsion for thrust generation. Specifically, they concluded that prolate medusae display a strong jet flow component in the wake, whereas oblate species are dominated by vortex ring formation. Hence the results of the present study are primarily

applicable to oblate forms. In several respects, however, our results may be relevant to prolate medusae.

The most important effect to recognize is that any accelerated jet with flow separation from a circular orifice and sufficiently large Reynolds number can form a vortex ring. Cantwell (1986) computed that the minimum Reynolds number required for vortex ring formation is approximately six. This is well below the swimming regime of medusan swimmers, both prolate and oblate (Gladfelter, 1973; Colin and Costello, 2002). We can therefore expect that prolate medusae will also experience vortex ring formation.

A primary difference between the wake of a prolate swimmer and that of an oblate form, however, lies in the duration of fluid ejection, as measured by the formation time (A/D ; see figure 9.1). In laboratory experiments, Gharib et al. (1998) demonstrated that when the formation time exceeds a value of 4, the leading vortex ring at the front of the fluid discharge stops growing and pinches off from the remaining fluid discharge behind it. In the swimming medusae, several additional parameters become important such as temporal variation in the bell diameter and swimming speed (Dabiri and Gharib, 2004b; Krueger et al., 2003). These factors will likely affect the ratio, changing it from the nominal value of four. Nonetheless, we can expect the physical principles to remain unchanged. Oblate medusae tend to eject fluid with small A/D ratios, thereby avoiding both pinch-off of the leading vortex ring and formation of a trailing jet flow. This leads to the observed dominance of vortex ring structures in the wake of oblate swimmers. By contrast, prolate medusae will tend to eject fluid with larger A/D ratios, leading to a substantial presence of jet flow behind the leading vortex rings in the flow. The difference in these ratios appears to be consistent with the different foraging strategies of the two forms. The low formation

numbers of oblate forms suggest that their mode of propulsion may be more efficient, which is consistent with their cruising strategy (Table 9.1). Conversely, larger A/D ratios in prolate forms are consistent with their roles as ambush predators that periodically require large thrust generation, perhaps at the expense of swimming efficiency.

Colin and Costello (2002) show that the dominant presence of jet flow in prolate medusae makes them more amenable to models based on jet flow such as that of Daniel (1983). However, one cannot neglect to also examine the vortex ring formation that will occur early during bell contraction in prolate medusae. Some form of the co-joined wake vortex ring structures observed in the present study may also appear in the wakes of a variety of medusae, particularly those with intermediate bells between prolate and oblate morphologies. Further examination of wake structure and thrust generation will be necessary to properly model the dynamic swimming behavior of these animals.

Parameter	Thrust	Efficiency
Vortex ring volume	+	+
Vortex ring spacing	-	-
Jet ratio A/D	+	-

Table 9.1 Relationship between starting vortex ring kinematics and dynamics. Both thrust and efficiency increase in direct proportion with vortex ring volume. By contrast, thrust and efficiency decrease with increasing vortex spacing due to diminished inter-ring interactions. For a fixed volume of ejected fluid, the thrust increases with jet ratio A/D , at the expense of efficiency. Trends are based on the assumption of negligible vortex formation during the recovery stroke. + indicates a direct relationship and – indicates an inverse relationship (cf. Weihs, 1977; Krueger and Gharib, 2003).

9.4.4 *A note on fluid dynamic and geometric scaling*

One aim of this work has been to demonstrate the robustness of the observed flow patterns over a wide range of medusae sizes. If the fluid dynamical effects are insensitive to geometric scaling—as we have seen here—then the kinematics of bell motion that dictate the fluid dynamics should also be scale-invariant. We demonstrate this effect straightaway by plotting the shape profile for the smaller and larger medusae at full bell contraction and relaxation in coordinates normalized by the cube root of the ejected bell fluid volume, $\Omega_b^{1/3}$ (figure 9.5). The cube root of the volume is used rather than the volume itself so that the normalized coordinates are dimensionless, thereby facilitating comparison across the full range of animal sizes. Consistent with the arguments presented in this chapter and the findings of McHenry and Jed (2003), the bell kinematics are very similar, despite the order of magnitude difference in the volumes of the subjects. A similar examination should be made for other species of medusae, to determine the generality of the fluid dynamic and geometric scaling sensitivities observed here.

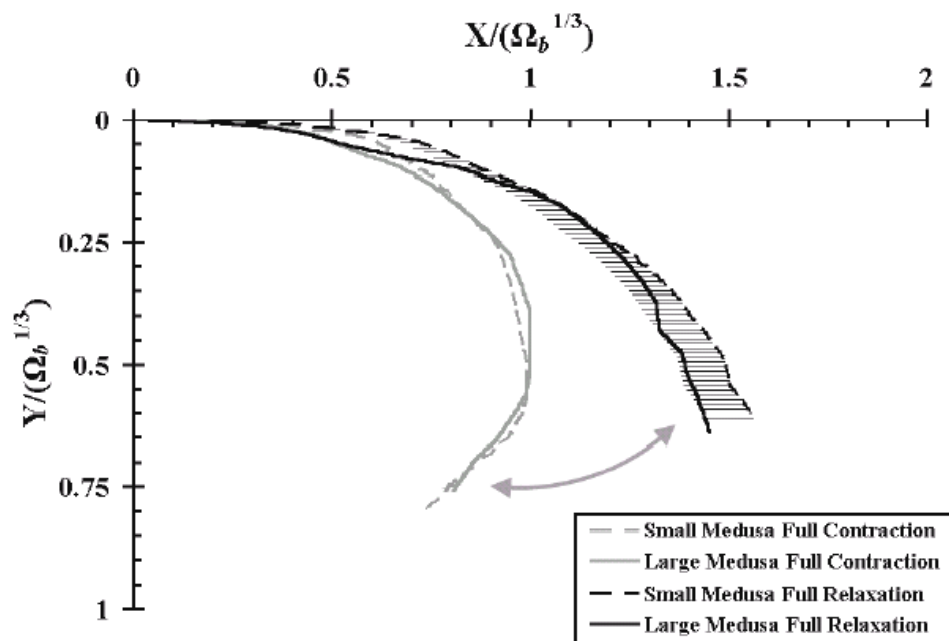


Figure 9.5 Medusa bell shape profiles normalized by volume of ejected bell fluid Ω_b . Dashed lines, small medusa; solid lines, large medusa; gray lines, full bell contraction; black lines, full bell relaxation. Horizontal bars denote measurement uncertainty.

9.5 Chapter References

- Cantwell, B. J. 1986 Viscous starting jets. *J. Fluid Mech.* **173**, 159-189.
- Colin, S. P. and Costello, J. H. 2002 Morphology, swimming performance, and propulsive mode of six co-occurring hydromedusae. *J. Exp. Biol.* **205**, 427-437.
- Costello, J. H. and Colin, S. P. 1994 Morphology, fluid motion and predation by the scyphomedusa *Aurelia aurita*. *Mar. Biol.* **121**, 327-334.
- Costello, J. H. and Colin, S. P. 1995 Flow and feeding by swimming scyphomedusae. *Mar. Biol.* **124**, 399-406.
- Costello J. H., Klos E. and Ford M. D. 1998 In situ time budgets of the scyphomedusae *Aurelia aurita*, *Cyanea* sp., and *Chrysaora quinquecirrha*. *J. Plankton Res.* **20**, 383-391.

- Dabiri, J. O. and Gharib, M. 2003 Sensitivity analysis of kinematic approximations in dynamic medusan swimming models. *J. Exp. Biol.* **206**, 3675-3680.
- Dabiri, J. O. and Gharib, M. 2004 Fluid entrainment by isolated vortex rings. *J. Fluid Mech.* **511**, 311-331.
- Dabiri, J. O. and Gharib, M. 2004 Starting flow through nozzles with temporally variable exit diameter. *J. Fluid Mech.*, in press.
- D'Ambra, I., Costello, J. H. and Bentivegna F. 2001 Flow and prey capture by the scyphomedusa *Phyllorhiza punctata* von Lendenfeld, 1884. *Hydrobiologia* **451**, 223-227.
- Daniel, T. L. 1983 Mechanics and energetics of medusan jet propulsion. *Can. J. Zool.* **61**, 1406-1420.
- Didden N. 1979 Formation of vortex rings—rolling-up and production of circulation. *Z. Angew. Math. Phys.* **30**, 101-116.
- Ford, M. D. and Costello, J. H. 2000 Kinematic comparison of bell contraction by four species of hydromedusae. *Sci. Mar.* **64**, 47-53.
- Ford, M. D., Costello, J. H., Heidelberg, K. B. and Purcell, J. E. 1997 Swimming and feeding by the scyphomedusa *Chrysaora quinquecirrha*. *Mar. Biol.* **129**, 355-362.
- Freedman, D., Pisani, R. and Purves, R. 1998 *Statistics*. W. W. Norton.
- Gharib, M., Rambod, E. and Shariff, K. 1998 A universal time scale for vortex ring formation. *J. Fluid Mech.* **360**, 121-140.
- Krueger, P. S., Dabiri, J. O. and Gharib, M. 2003 Vortex ring pinch-off in the presence of simultaneously initiated uniform background co-flow. *Phys. Fluids* **15**, L49-L52.

- Krueger, P. S. and Gharib, M. 2003 The significance of vortex ring formation to the impulse and thrust of a starting jet. *Phys. Fluids* **15**, 1271-1281.
- Lamb, H. 1932 *Hydrodynamics*. Cambridge University Press.
- Lim, T. T. and Nickels, T. B. 1995 Vortex Rings. In *Fluid Vortices*. Kluwer Academic Publishers.
- McHenry, M. J. and Jed, J. 2003 The ontogenetic scaling of hydrodynamics and swimming performance in jellyfish (*Aurelia aurita*). *J. Exp. Biol.* **206**, 4125-4137.
- Rayner, J. M. V. and Thomas, A. L. R. 1991 On the vortex wake of an animal flying in a confined volume. *Philos. T. Roy. Soc. B* **334**, 107-117.
- Sullivan, B. K., Garcia, J. R. and Klein-MacPhee, G. 1994 Prey selection by the scyphomedusan predator *Aurelia aurita*. *Mar. Biol.* **121**, 335-341.
- Vogel, S. 1994 *Life in Moving Fluids*. Princeton University Press.
- Weihs, D. 1977 Periodic jet propulsion of aquatic creatures. *Forts. Zool.* **24**, 171-175.
- Willert, C. E. and Gharib, M. 1991 Digital particle image velocimetry. *Exp. Fluids* **10**, 181-193.